



저작자표시-비영리-변경금지 2.0 대한민국

이용자는 아래의 조건을 따르는 경우에 한하여 자유롭게

- 이 저작물을 복제, 배포, 전송, 전시, 공연 및 방송할 수 있습니다.

다음과 같은 조건을 따라야 합니다:



저작자표시. 귀하는 원저작자를 표시하여야 합니다.



비영리. 귀하는 이 저작물을 영리 목적으로 이용할 수 없습니다.



변경금지. 귀하는 이 저작물을 개작, 변형 또는 가공할 수 없습니다.

- 귀하는, 이 저작물의 재이용이나 배포의 경우, 이 저작물에 적용된 이용허락조건을 명확하게 나타내어야 합니다.
- 저작권자로부터 별도의 허가를 받으면 이러한 조건들은 적용되지 않습니다.

저작권법에 따른 이용자의 권리는 위의 내용에 의하여 영향을 받지 않습니다.

이것은 [이용허락규약\(Legal Code\)](#)을 이해하기 쉽게 요약한 것입니다.

[Disclaimer](#)

공학박사학위논문

**Study on the microstructure of
active materials in lithium ion battery
with enhanced life cycle**

고수명 리튬 이온 전지용 활물질 미세 구조 연구

2016 년 2 월

서울대학교 대학원

재료공학부

김 슬 참

Abstract

Study on the microstructure of active materials in lithium ion battery with enhanced life cycle

Seul Cham Kim

Department of Materials Science and Engineering

The Graduate School

Seoul National University

In this thesis studies, we observed the changes of microstructure in various types of Li ion battery anode and cathode materials FIB/SEM/TEM. It was drawn that stable microstructure for enhanced life cycle by correlating electrochemical properties and change of microstructure with cycle progress. This study is comprised of two parts. Part 1, observation of Si anode materials micro structure from various viewpoints. Part 2, analyze of micro structural change of cathode materials according types of electrolyte.

Part 1, drawn suitable microstructure for enhanced life properties by analyzing Si based anode material's microstructure from a variety of points. For good life, effective stress control that generated by volume expansion and suppression of SEI layer forming.

First point is stress, mechanical fracture occurred on surface and inside of Si particle, new surface became irreversible SEI layer, exposed at fracture area. In order to effectively control the stress from volume expansion, and ultrafine grain size and uniform microstructure are required. Occurred stress decreased with downsizing grain size. Because volume expansion of fine grain size is smaller than large grain, fracture of Si particle occurring is prevented from stress. And uniform microstructure through whole particle is also very important. If microstructure is non uniform even though Si particle has fine grain size, imbalance of stress is occurred. Mechanical alloying (High Energy ball milling) process is suitable for refining grain size and formation uniform microstructure. After MA process, Si and Silicide single grain have of 5 ~ 20nm and mixed very well. During cycle progress, significantly change of the microstructure was not observed. Aggregation is also very important for MA Si alloys. If particles have weak aggregation force, SEI layer should be formed easily by penetration of electrolyte inside of particles, it caused life cycled decreased rapidly. Carbon is added in progress of Mechanical alloying process as bonding phase for improving aggregation force and remaining after

100 cycles.

Second point is surface carbon coating, carbon has ionic/electrical conductivity, and easy for applying particle coating process. Carbon coating layer increase conductivity and prevent mechanical fracture of Si particle. After cycle progress, coating layer and the Si nanoparticles display no evidence of cracking nor does the C layer/Si interface show signs of delamination. And, applying the ionic liquid as electrolyte, additional C layer is formed during electrochemical reaction on Si particle surface that improved life cycle by forming more stable SEI layer than general electrolyte.

Third is the formation of 3D network structure due to the diffusion of Si in C matrix. Si/AC composite that has Si embedded in C matrix structure is made by mixed with Si nano particle and carbon. The Si nano path connected into the network structure in-situ during the charge and discharge process. Si is diffused in the C matrix to form a Si network for faster Li ion transmission. 3D Si network provides electronic/ionic conductivity and structure stability for the Si/AC composite,

Part 2, Micro structural changes of cathode materials using solid and liquid electrolyte are observed during cycle. We can understand difference between solid and liquid electrolyte cells by analyzing both of the two types of the electrolyte. In case of solid electrolyte, since the reaction area is limited, the reaction rate has slowed but microstructures are stable, On the contrary, in

case of liquid electrolyte, since the reaction is occurred every area in electrode, the reaction speed is high but micro structure is unstable.

First, we report that a solid-state battery with sulfide based electrolyte enables the reversible FeS_2 (pyrite) cathode material. We find that nanoparticles of orthorhombic FeS_2 are generated upon recharge at 30–60°C which explains a coincident change in rate kinetics. Because orthorhombic structure has bigger unit cell than cubic structure, Li ion pass more easily. In the case of the solid electrolyte, life properties is improved by preventing liberated of Sulfur.

Second, we present improvement process of life properties of cathode active materials. In case of NMC, life property is reduced by change of microstructure from single crystal to amorphous according to the progress of the cycle. TEM selected area electron diffraction (SAED) patterns show that NMC Bare electrode undergoes phase transition during 100 cycles from layered structure mother phase (space group: R-3m) to spinel cubic structure (space group: Fd3m). In contrast, the Al_2O_3 -ALD coating layer preserves the original layered structure of NMC/4ALD electrode for the same cycling period

Keywords : Lithium ion battery, Silicon anode, Carbon coating, Volume expansion of electrode materials, 3D Si network, Microstructure of active materials, Solid State Electrolyte, Transmission Electron Microscope, Focused Ion Beam

Student Number : 2011-31279

Table of Contents

Abstract.....	i
Table of Contents.....	vi
List of Tables.....	xiii
List of Figures.....	xiv

Chapter 1. Introduction

1.1 Introduction of Li ion battery.....	1
1.2 Advantages and disadvantages	1
1.3 Variety types of Li-ion batteries	1
1.3.1 Positive electrode (cathode) materials	2
1.3.2 Negative electrode (anode) materials	2
1.4 Charging and Discharging sequence of Li-ion Batteries.....	5
1.5 References.....	5

Part 1. Micro-structural study of Si base anode materials from a variety points

Chapter 2. Effect of micro structural change due to stress

and volume expansion behavior of Si alloy during cycle

2.1	Introduction	7
2.1.1	Previous study with Si for anode for Li Battery.....	7
2.1.2	Mechanical Alloying process.....	8
2.1.3	Volume expansion behavior of electrode materials.....	8
2.2	Experimental procedure.....	9
2.2.1	Mechanical Alloying process.....	9
2.2.2	Electrochemical test & Analysis of Microstructure.....	9
2.2.3	Measurement of expansion ratio.....	10
2.3	Results and discussion.....	12
2.3.1	Microstructural change of MA Si alloy.....	12
2.3.2	Volume expansion behavior of electrode materials.....	12
2.4	Conclusion.....	26
2.5	Reference.....	27

Chapter 3. Surface modification for enhancing the life property of Si anode cycle

3.1	Introduction.....	30
3.1.1	Previous study with Carbon coating on Si	30
3.1.2	Effect of ionic liquid electrolyte.....	30

3.2	Experiment Procedure.....	31
3.2.1	PAN coating.....	31
3.2.3	Electrochemical test & Analysis of Microstructure.....	31
3.3	Results and discussion.....	32
3.3.1	Conformal carbon coating on Si nano particle.....	32
3.3.2	Forming stable SEI by ionic liquid electrolyte.....	39
3.4	Conclusion.....	47
3.5	Reference.....	49

Chapter 4. Shape change of Si particle during electro-chemical reaction

4.1	Introduction.....	52
4.1.1	Introduction of Si/C composite.....	52
4.1.2	Forming 3D Si network.....	53
4.2	Experiment procedure.....	53
4.2.1	Preparation of Si/C composite.....	53
4.2.2	Electrochemical test & Analysis of Microstructure.....	54
4.3	Results and discussion.....	54
4.3.1	Microstructure of Si/C composite with cycle progress.....	54
4.3.2	Forming 3D Si network.....	58

4.4	Conclusion.....	60
4.5	Reference.....	61

Part 2. Micro-structural change observation of variety types of cathode materials during cycle

Chapter 5. Structural change observation of reversible FeS₂ cathode in solid state electrolyte system

5.1	Introduction.....	63
5.1.1	Previous study with Carbon coating on Si	63
5.1.2	Effect of ionic liquid electrolyte.....	63
5.2	Experiment Procedure.....	64
5.2.1	Synthesis of Pyrite.....	64
5.2.2	Solid state electrolyte battery.....	64
5.2.3	Electrochemical test & Analysis of Microstructure.....	65
5.3	Results and discussion.....	66
5.3.1	Electrochemical properties of Pyrite.....	66
5.3.2	Microstructural change of pyrite.....	70
5.4	Conclusion.....	75
5.5	Reference.....	76

Chapter 6. Improvement life performance of Ni-Mn-Co intercalation cathode materials by Al₂O₃ ALD coating for preventing micro structural change

6.1	Introduction.....	78
6.1.1	LiNi _{1/3} Mn _{1/3} Co _{1/3} O ₂ (NMC) cathodes.....	78
6.1.2	Atomic Layer Deposition.....	79
6.2	Experiment procedure.....	79
6.2.1	Al ₂ O ₃ ALD ON NMC particle.....	79
6.2.2	Electrochemical test & Analysis of Microstructure.....	80
6.3	Results and discussion.....	81
6.3.1	Electrochemical properties of ALD coated NMC.....	82
6.3.2	ALD coating effect on microstructure of NMC during cycle.....	86
6.3.3	Life cycled performance comparison between w/ & w/o ALD...	90
6.4	Conclusion.....	93
6.5	Reference.	94

Chapter 7. Conclusion.....97

Appendix 1. Thermal stability of ZnS nanowires studied by

using in-situ heating X-ray diffraction

8.1 Introduction.....	100
8.1.1 1D semi-conductor nano materials.....	100
8.1.2 ZnS nanowire.....	100
8.2 Experiment procedure.....	101
8.2.1 Synthesis of ZnS nanowire.....	101
8.2.2 Characterize the thermal stability of ZnS nanowire.....	102
8.3 Results and discussion.....	105
8.4 Conclusion.....	113
8.5 Reference.....	114

Appendix 2. Martensite in interstitial-free steel obtained by ultra-high pressure

9.1 Introduction.....	116
9.1.1 Interstitial Free steel.....	116
9.1.2 High pressure high temperature.....	117
9.2 Experiment procedure.....	117
9.2.1 High pressure high temperature.....	117
9.2.2 Microstructure analysis.....	118
9.3 Results and discussion.....	121

9.4 Conclusion.....	127
9.5 Reference.....	128
국문 초록.....	130
Curriculum Vitae.....	133

LIST OF TABLES

Table 1.1 Electrochemical properties of alloys for Lithium Ion battery

Table 9.1 Chemical composition of IF steel used in the study (wt.%).

LIST OF FIGURES

Figure 1.1 Approximate current and voltage during typical Li-ion charge cycle.

Exact values depend on charging conditions and battery type

Figure 2.1 (a) Voltage profile of Step sequence discharge state between Si alloy and Graphite (b) Si particle area measurement using image processing in cross-sectional image. (c) Pixels and area measurement data of each Si particle

Figure 2.2 (a) TEM micrograph of the Melt spunned Si alloy (b) TEM micrograph of the ball milled alloying Si alloy

Figure 2.3 (a) cS corrected high resolution TEM micrograph of ball milled alloying Si alloy (b) cS corrected high resolution STEM micrograph of same area

Figure 2.4 (a) Results of life properties of MA Si-Fe alloy (sample 1). (b) TEM micrograph of initial ball milled alloying Si (c) TEM micrograph of 50 cycled

Figure 2.5 (a) TEM micrograph of initial ball milled alloying Si particle. (b) TEM micrograph of 50 cycled ball milled alloying Si particle (c) TEM micrograph of 100 cycled ball milled alloying Si particle

Figure 2.6 (a) EELS zero-loss map of SEI layer formed inside of particle. (b)

EELS Map of Si (c) EELS Map of Fe (d) EELS Map of O (e) EELS Map of C

Figure 2.7 (a) Concept illustrate of Carbon as bond phase (b) TEM BF image of secondary particle before C coating (c) after C coating. (d) TEM BF image of initial C coating area of inside particle (e) after 100 cycles

Figure 2.8 Expansion ratio of Electrode (Black line) and Si alloy (Blue line) with cycle progress

Figure 2.9 Concept illustrate of Si alloy expansion at delithiated state by inactive matrix lithiation, (a) Initial state of Si alloy (b) Lithiated state of Si alloy (c) Delithiated state of Si alloy

Figure 2.10 Zerolss and EELS mapping image of Si alloy during cycle (a) 1st lithiated zero loss image of Si alloy (White Si, Black matrix) (b) 1st lithiated EELS mapping image of Si alloy (R : Si, B: Li) (c) 50 cycled zero loss image of Si alloy (White Si, Black matrix) (d) 50 cycled EELS mapping image of Si alloy (R : Si, B: Li) (e) 200 cycled zero loss image of Si alloy (White Si, Black matrix) (f) 200 cycled EELS mapping image of Si alloy (R : Si, B: Li) (g) Cycle-Capacity graph of Si-alloy (h) Cycle-Capacity graph of matrix only.

Figure 3.1(a) TEM micrograph of the uncycled nano-Si/cyclized-PAN

electrode with (b) EELS elemental mapping confirming that we achieve a conformal 5 nm thick cyclized-PAN coating. (c) Raman spectra for an untreated electrode (red) and for an electrode treated at 300°C (cyan). The delocalized $sp^2\pi$ D and G bands present in the spectra

Figure 3.2 (a) Cyclic capacity (blue circles) and CE (blue squares) of nano-Si/cyclized-PAN electrodes run at a rate of C/20 for the first 10 cycles and at C/10 for subsequent cycles. A conventional nano-Si electrode (red circles) was cycled at a rate of C/10 as a control cell. After 150 cycles, our nano-Si/cyclized-PAN composite electrode has a specific charge capacity of nearly 1500 mAh/g and a CE approaching 100%, whereas the conventional electrode fails after 3 cycles. (b) Voltage profiles of our nano-Si/cyclized-PAN electrode showing a minimal overpotential when cycled at C/10 compared to C/20. (c) A rate test demonstrates that our nano-Si/cyclized-PAN electrodes can achieve a specific charge capacity in excess of 2300 mAh/g at a rate of 5C.

Figure 3.3 (a), (b) TEM micrographs of a nano-Si/cyclized-PAN electrode cross-sections before and after initial lithiation, respectively. Si's expansion is largely accommodated by the porosity of the electrode such that the electrode only expands by 40%. (c) The porous structure reopens upon delithiation after 20 cycles indicating that ionic transport pathways are maintained. (d), (e) TEM

micrographs of a delithiated nano-Si/cyclized-PAN electrode collected after its 20th cycle. We observe that the cyclized-PAN coating does not delaminate from Si particles nor does it crack.

Figure 3.4 Galvanostatic performance of various electrolyte systems with nSi-cPAN. (a) Specific capacities and coulombic efficiencies of nSi-cPAN electrode in PYR13FSI (1.2M LiFSI) and EC/DEC (1M LiPF₆). (b) Specific capacities and coulombic efficiencies of nSi-cPAN electrode in PYR13TFSI (0.6M LiTFSI) and EMIMFSI (1.2M LiFSI) electrolyte systems. Cycling was carried out at room temperature in 2032 coin-type half-cells operated between 0.05 and 1V (versus Li/Li⁺).

Figure 3.5 Solid-electrolyte interphase composition of the Si-PYR13FSI system. (a) EELS elemental mapping of Si from (b) TEM micrograph of cycled nSi-cPAN electrode at the 16th delithiation along with EELS elemental mapping and XPS analysis of (c,d) carbon, (e,f) sulfur, (g,h) fluorine, (i,j) lithium and (k,l) oxygen, defining the elemental constitution and favored nucleation sites of the SEI formed.

Figure 3.6 Microstructure of nSi-cPAN and morphological effects of PYR13FSI IL on anode. (a) EELS elemental mapping of carbon (cyan) and silicon (red) and (b) TEM micrograph of the pristine nSi-cPAN electrode reveal a thin, conformal coating of PAN on the nano-Si particles throughout

the uncycled composite. (c,d) FESEM images of electrode cross-sections before (c) and after (d) initial lithiation showing an electrode volume expansion of only 17%. (e–h) TEM micrographs of fully lithiated (e,f) and 16th delithiated (g,h) nSi-cPAN electrodes showing no mechanical deficiencies or significant morphological changes.

Figure 4.1 Schematics of forming Si 3D network during lithiation and delithiation in Si/AC composite (a) Initial state of Si/AC composite particle. (b) Si diffuse (migration) in C matrix during delithiation. (c) Si nanoparticles tend to fuse to form a network structure to fastest Li ion transfer path. The physical connections between the Si nano particles and the conductive network are preserved during the discharge process

Figure 4.2 Micro-structural change observation of Si nano particle in Si/AC composite during cycle (a) Initial shape of Si/AC composite, (b) 1st lithiated state, (c) after 5 cycles, (d) after 100 cycles

Figure 4.3. (a) After 100 cycle Si particle surface that distance between another particles are close, (b) After 100 cycle surface of isolated Si particles, (c) High-resolution STEM images of 100 cycled Si/AC composite.

Figure 5.1 (a) Indexed x-ray diffraction of synthetic cubic-FeS₂. (b) FESEM image of synthetic cubic-FeS₂ that confirms cubic structure with 2–3 μ m cubes.

Figure 5.2 Comparison of synthetic cubic-FeS₂ cycled at 30 ° C and 60 ° C in conventional liquid coin cells and in solid-state cells: a) solid-state cell at 30 ° C, b) solid-state cell at 60 ° C, c) liquid coin cell at 30 ° C, d) liquid coin cell at 60 ° C, e) capacity retention comparison of cells cycled at 30 ° C, and f) capacity retention comparison of cells cycled at 60 ° C. All cells except for the 30 ° C solid-state cell were cycled at a current of 144 μ A which corresponds to a rate

Figure 5.3 (a) Coulometric titration results for the solid-state cell titrated at 60 ° C compared with the 1st , 2nd , and 10th discharge profiles for the solid-state cell cycled at 60 ° C (Figure 2 b). (b) dQ/dV of solid-state cell cycled at 30 ° C. (c) Deconvolution of the dQ/dV peaks at 2.1 and 2.2V with fitted peaks and residual.

Figure 5.4 Electrode material from the solid-state cell cycled at 60 ° C (Figure 2 b) was recovered after the 20th charge for TEM analysis. a) Bright field TEM image of the 20th cycle sample. Darker areas correspond to nanocrystalline orthorhombic-FeS₂ while the lighter areas correspond to an amorphous region composed of FeS_y and elemental sulfur. b) HR-TEM of the 20th cycle sample. FFT analysis matches with orthorhombic-FeS₂ along the [- 110] zone axis.

Figure 6.1. Cycling performance of half cells using uncoated-NMC (NMC Bare), uncoated-NMC:LMO (NMC:LMO, 1:1 mixture) and Al₂O₃ 4ALD coated-NMC (NMC/4ALD) cathodes cycled between 3.0 and 4.5 V versus Li⁺/Li at 25 °C at 1 C-rate (160 mA g⁻¹ for NMC Bare and NMC/ALD and 130 mA g⁻¹ for NMC:LMO) following after the first two formation cycles at C/4-rate (40 mA g⁻¹ for NMC Bare and NMC/ALD and 32.5 mA g⁻¹ for NMC:LMO). Discharge capacities at 4C-rate (640 mA g⁻¹ for NMC Bare and NMC/ALD and 520 mA g⁻¹ for NMC:LMO) after 100 cycles are shown at the 101st cycle

Figure 6.2 (a~c) Comparison of 3rd and 100th charge/discharge voltage profiles (3.0~4.5 V) at 1 C-rate, (d~f) charge/discharge voltage profiles at 4 C-rate after continuous 100 cycles at 1 C-rate of NMC Bare, NMC:LMO and NMC/4ALD half cells. Voltage hold is applied at 4.5 V for 0.5 h after each charge step.

Figure 6.3 FIB cross-section images of fully charged (delithiated) (a) NMC Bare and (b) NMC/4ALD after 100 cycles at 1 C-rate between 3.0 and 4.5 V. TEM selected area electron diffraction (SAED) patterns from inner area (1) and outer area (2) of each particle show phase transition in NMC Bare electrode (c,d) whereas NMC/4ALD presents same crystal structure from inner and outer area (e,f).

Figure 6.4 Synchrotron X-ray diffraction patterns of fully charged (a,b) NMC Bare and (c,d) NMC/4ALD at 3rd cycle and 100th cycle respectively during 1 C-rate cycling test between 3.0 and 4.5 V.

Figure 6.5 (a) Cycling performance of half cells using uncoated-NMC (NMC Bare), uncoated-MC:LMO (NMC:LMO, 1:1 mixture) and Al₂O₃ 4ALD coated-NMC (NMC/4ALD) cathodes cycled between 3.0 and 4.5 V versus Lip/Li at 55 °C by applying a constant rate of 1 C-rate (160 mA g⁻¹ for NMC Bare and NMC/ALD and 130 mA g⁻¹ for NMC:LMO) following after the first two formation cycles at C/4-rate (40 mA g⁻¹ for NMC Bare and NMC/ALD and 32.5 mA g⁻¹ for NMC:LMO). Comparison of 3rd and 70th charge/discharge voltage profiles (3.0~4.5 V) at 1 C-rate of (b) NMC Bare, (c) NMC:LMO and (d) NMC/4ALD half cells. Voltage hold was applied at 4.5 V for 0.5 h after each charge step.

Figure 6.6 (a) Cycling performance of half cells using uncoated-NMC (NMC Bare), uncoated-MC:LMO (NMC:LMO, 1:1 mixture) and Al₂O₃ 4ALD coated-NMC (NMC/4ALD) cathodes cycled between 3.0 and 4.3 V versus Lip/Li at 55 °C by applying a constant rate of 1 C-rate (160 mA g⁻¹ for NMC Bare and NMC/ALD and 130 mA g⁻¹ for NMC:LMO) following after the first two formation cycles at C/4-rate (40 mA g⁻¹ for NMC Bare and NMC/ALD and 32.5 mA g⁻¹ for NMC:LMO). Comparison of 3rd and 70th

charge/discharge voltage profiles (3.0e 4.3 V) at 1 C-rate of (b) NMC Bare, (c) NMC:LMO and (d) NMC/4ALD half cells. Voltage hold was applied at 4.3 V for 0.5 h after each charge step.

Figure 8.1 (a) Schematic representation of ZnS nanowires showing the Au/Pd-catalyzed VLS reaction. (b) In-situ heating XRD measurement diagram (Red circle: XRD data acquisition time for 10 min)

Figure 8.2 X-ray diffraction pattern by in-situ heating at (a) 25°C, (b) 500°C, (c) 600°C, (d) 700°C, (e) 800°C, and (f) 900°C. (g) Low-magnification 70°tilted SEM image of as-synthesized ZnS nanowires. (h) High-magnification 70° tilted SEM image of as-synthesized ZnS nanowires.

Figure 8.3 (a) Low-magnification SEM image of as-synthesized ZnS nanowires. (b) Enlarged SEM image of as-synthesized ZnS nanowires. (c) SEM image of ZnS nanowires obtained by 900°C heat-treatment. (d) High-magnification SEM image of (c).

Figure 8.4 (a) Low-magnification TEM image of as-synthesized ZnS nanowire. (b) HRTEM image at upper part of as-synthesized ZnS nanowire (inset: FFT pattern showing [111] growth direction). (c) TEM image of ZnS nanowires obtained by 900°C heat-treatment. (d) HRTEM image of degraded ZnS nanostructure (inset: FFT pattern corresponding to HRTEM image).

Figure 9.1. The structure of the reaction cell for the HPHT process. The pressure dummy is a plain carbon steel and the dimension is optimized for the preset conditions of pressure and temperature (5 GPa, 1200°C).

Figure 9.2. Microstructure after HPHT process: (a) EBSD orientation map overlaid on band contrast map, (b) TEM micrograph and (c) distribution of twin boundaries (thick black lines) in the upper-left part of (a).

Figure 9.3. Microstructures produced under atmospheric pressure, heated to 1150°C at 10°C/sec, held for 10 min and cooled at (a) 8 and (b) 50°C/sec

Chapter 1. Introduction

1.1 Introduction of Li ion battery

Lithium-ion (Li-Ion) batteries are becoming more public in portable electronic devices because of their high energy density, enable to high speed charge and discharge and no memory effect. Lithium-ion batteries are quite new technology, research and development goals are to improve increase capacity and safety, fast charge/discharge and durability. This study describes microstructure of variety types of lithium-ion batteries currently interested.

1.2 Advantages of Li ion batteries

The main advantage of lithium ion batteries is their high energy density and that have good life cycle and do not occur high rate of self-discharge and memory effect of traditional rechargeable batteries like NiCd and NiMH. In contrast to the sealed lead acid (SLA) and nickel cadmium, lithium ion batteries do not have toxic materials (heavy metals). The main disadvantage of lithium-ion batteries that they require special attention to safety. Recharge, overheat or short circuit by forming Li dendrite during cycle can cause a fire or explosion. Safety product design must be required.

1.3 Variety types of Li-ion batteries

All lithium-ion batteries use processes known as intercalation and alloying in which lithium ions are incorporated in the structure of the electrode material. Lithium ions move from the cathode to the anode during charging, and from the anode to the

cathode of the battery is discharged.

Most types of lithium ion batteries available today differ in composition of the positive electrode (cathode). Because of the development of new materials for the negative electrode, few of them are currently available on the market including Si based anode materials.

1.3.1 Positive electrode (cathode) materials

Various positive electrode materials vary in cost, safety and energy density. Lithium Cobalt Oxide (LCO), Nickel Manganese Cobalt (NMC) are the most common types of cathode materials. Lithium Iron Phosphate (LFP or LiFePO_4) becomes as a choice when required safety more than energy density. Some battery cells made by mixture of Lithium Manganese Oxide (LMO) and the NMC, which provides better storage and enhanced life cycle.

1.3.2 Negative electrode (anode) materials

Graphite is by far the most common material for the anode, but also some other technology researches are progressing. Lithium metal alloys like Si and Sn are known for their high specific capacity and safety characteristics, as well as for some metal elements supply that is abundant and their relatively low cost. Table. 1 compares the electrochemical properties of anode alloys materials. The alloys have a theoretical specific capacity that is 2 ~ 10 times higher than that of graphite, but the volume change is over 300%. For example, Si and Sn have specific capacity of 3,600mAh/g and 1000mAh/g. however, volume changes are over 300% (Si) and 200%

(Sn), respectively. Also, their onset voltage potentials are higher than graphite. (Alloy 0.4V ~ 0.6V, Graphite ~0,05V) Lithium metal alloy surrounding active particles (Si, Sn, Mg) so that is restraint volume change during charge-discharge. But after several cycles, the reversible capacity is dramatically decreased. Many research tried to solve volume expansion and micro fracture during cycle like Si alloying and surface carbon coating. [1]

Materials	Li	C	Si	Sn	Sb	Al	Mg	Bi
Density (g/cm ³)	0.53	2.25	2.33	7.29	6.7	2.7	1.3	9.78
Lithiated phase	Li	LiC ₆	Li _{4,4} Si	Li _{4,4} Sn	Li ₃ Sb	LiAl	Li ₃ Mg	Li ₃ Bi
Theoretical specific capacity (mAh/g ¹)	3862	372	4200	994	660	993	3350	385
Theoretical charge density (mAh/cm ³)	2047	837	9786	7246	4422	2681	4355	3765
Volume change (%)	100	12	320	260	200	96	100	215
Potential vs. Li (~V)	0	0.05	0.4	0.6	0.9	0.3	0.1	0.8

Table 1.1 Electrochemical properties of alloys

1.4 Charging and discharging sequence of Li-ion Batteries

The electrochemical reaction control and protection designs are critical for lithium-ion batteries. Almost Li ion batteries have built-in protection circuitry. Because of recharged lithium - ion battery can cause a fire or explosion, and over discharging may damage the battery. Li ion batteries are usually charged in two steps (Figure 1). The first step is the DC charging on 0.5-1C, until the battery reaches maximum voltage, usually 4.1-4.2 V/cell. After reaching maximum voltage, the battery is not charged at a constant voltage until the current drops below the threshold between 0.02 and 0.1C, or for a fixed amount of time, about 2 hours. If the battery is deeply discharged, the slow charge (0.1C) must be brought to the voltage of 2.5-3 V/cell before 0.5-1C charge can begin. However, attempting to charge a severely depleted battery may not be safe, and the battery may have permanent loss of capacity. [2]

1.5 Reference

[1] Wei-Jun, Z., Journal of Power Sources, (2011) 196, 13.

[2] R.A. Huggins, Advanced Batteries : Materials Science Aspects, *Springer*, 2008

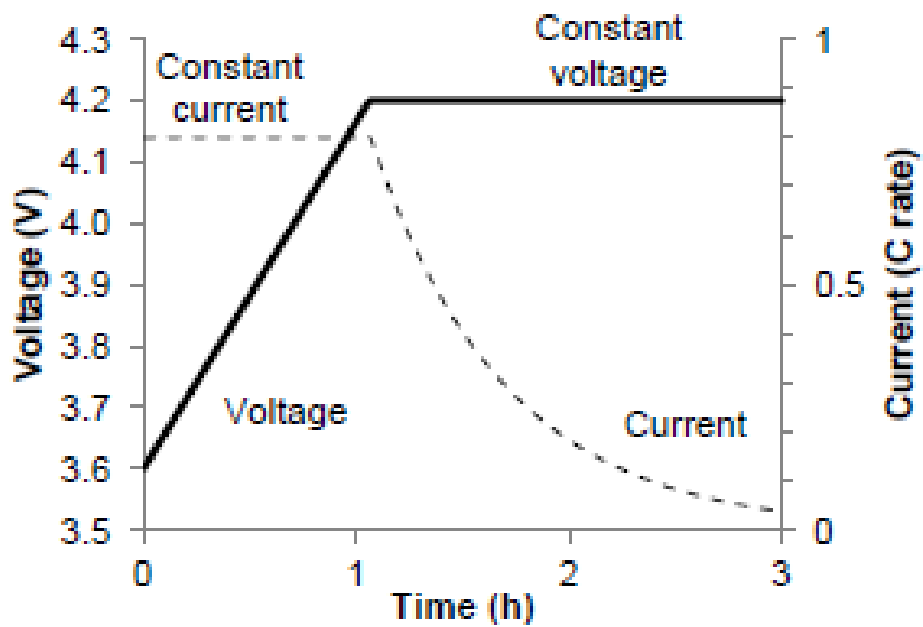


Figure 1.1 Approximate current and voltage during typical Li-ion charge cycle.

Exact values depend on charging conditions and battery type

Chapter 2. Effect of micro structural change due to stress and volume expansion behavior of Si alloy during cycle

2.1 Introduction

2.1.1 Previous study with Si for anode for Li Battery.

Lithium ion batteries (LIBs) are most interested energy source for a variety of electronic devices and electric vehicles (Electric Vehicles, Hybrid Electric Vehicles, Plug-in Hybrid Electric vehicles) with new electrode materials. These materials required high level energy density and good life cycle properties. [1,2]

Now days, graphite is most widely used anode material for LIBs because it shows good life cycle properties, even though it's capacity is only 372mAh/g. Although graphite shows good life cycle but new devices and variety electric vehicle systems require anode materials with higher capacities. Si is one of the most promising materials studied to replace graphite.

Specific capacity of Si is 3600mAh/g (forming $\text{Li}_{15}\text{Si}_4$) which is the highest specific capacity known among materials reported. Si is 2nd place abundant element and non-toxic material. [3-6] However, Si has problems to applying commercial battery cells because it's a volume expansion of 300% with the Li insertion. Such a large volume expansion results in mechanical fracture which causes dramatically capacity decrease. SEI layer formed by reaction with liquid electrolyte cause poor coulombic efficiency. [7-10]

2.1.2 Mechanical Alloying process

In order to prevent mechanical fracture from cycle progress using nano materials like Si nano-powders, nano-wires, or Si alloying process. Si nano materials have stable for applying battery cells because Li-ion diffusion pathways are shortened compared to the bulk and better cycle performance. [11–19] However, Si nano-materials cause cost rising of Li battery because it's expensive price. For this reason, the aforementioned technologies are not suitable for large scale manufacture to meet commercial demand. To reduction grain size of Si alloy and forming uniform microstructure, Si alloy particles are formed using ball milling. Mechanical alloying (high energy ball milling) is one of the most extensively used technique to produce ultrafine materials. Mechanical alloying consists of repeated fracture, mixing, and cold welding of a fine blend of metal, oxide, and alloy particles resulting in size reduction and sometimes in chemical reactions. [20]

2.1.3 Volume expansion behavior of electrode materials

And recently, research on the volume expansion of silicon is mainly focused on silicon nano-wire or nano-particle using in-situ system. [21] However, volume expansion study using in-situ system has different condition with actual electrode. And it has shown the limitation to investigate the relationship with configuration materials of electrode such as binder or conductive graphite.

2.2 Experimental procedure

2.2.1 Mechanical Alloying process

Si-Fe alloy powders were prepared by milling with a high-energy ball-mill (ZOZ). The alloy powders were characterized by X-ray diffraction (XRD). Si-Fe alloy powders were prepared by 2 steps. 1st step is ball-milling for crushing and mixing Si and silicide, 2nd step is carbon coating ball milled with artificial graphite (Timex SFG6) after 23hr Si-Fe alloy ball milling.

2.2.2 Electrochemical test & Analysis of Microstructure

Standard types of 2016 half coin cells with Li metal foil as a counter electrode were prepared for these experiments. The anode mixture was composed of Si-Fe, ketjen black and polyamide/imide (PAI) binder with a wt% ratio of 88%-4%-8%, and mixed with a 1-methyl-2-pyrrolidinone (NMP) solution. The mixture was coated on Cu foil and then dried under air. Considering weight ratio among materials, 1.0 mg cm⁻² of Si-Fe is applied on the single electrode. 1.5 M LiPF₆ in ethylene carbonate, diethyl carbonate and fluoroethylene carbonate (5:70:25) was used as the electrolyte. [22] Constant current (CC) is applied during discharge and charge between the voltage range of 0.01 V and 1.5 V. Constant voltage (CV) is applied until amount of 0.01c is achieved at 0.01 V and 20 minutes of holds are made at both 0.01 V and 1.5 V.

A FIB (FEI, NOVA200 dual beam system) equipped with an air-lock chamber is used for TEM sample preparation. Ga ion source is used for FIB sectioning. The use of an air-lock system enables to observe lithiated Si-Fe structure without any exposure to the air. Air exposure to lithiated sample causes structure changes with

oxidation, however this mobile air-lock system maintains a vacuum state while samples are loaded from glove box to FIB chamber. The microstructure of Si-Fe structure was investigated by HR-TEM (JEOL 3000F equipped with EDS) operating at 300keV and analytical TEM (TECNAI F20 equipped with EELS) operating at 200keV. XRD data for phase determination was collected with X-ray diffractometer (XRD, Bruker, D8 Advance) with Cu-K α radiation.

The electrodes are composed with 50 wt% silicon alloy particles, 50 wt% graphite (Si alloy 540mAh/g, graphite 180mAh/g), binder and liquid electrolyte (1 M LiPF₆ in EC : DEC : FEC 5:70:25 by weight) in 2032 coin cell.

By utilizing the discharge voltage difference between Si and graphene, measured by separating the charge-discharge behaviors of the active material

2.2.3 Measurement of expansion ratio

Measurement of the expansion ratio is comparing the thickness of the initial electrode and cycled electrode using dual beam FIB. Using ion beam to form cross-sectioned area of the electrode, and thickness of initial and cycled electrodes were measured 52 degree tilted scanning electron microscope. Individual behavior of the Si particles are statistically analyzed in cross-sectional SEM images with image processing process.

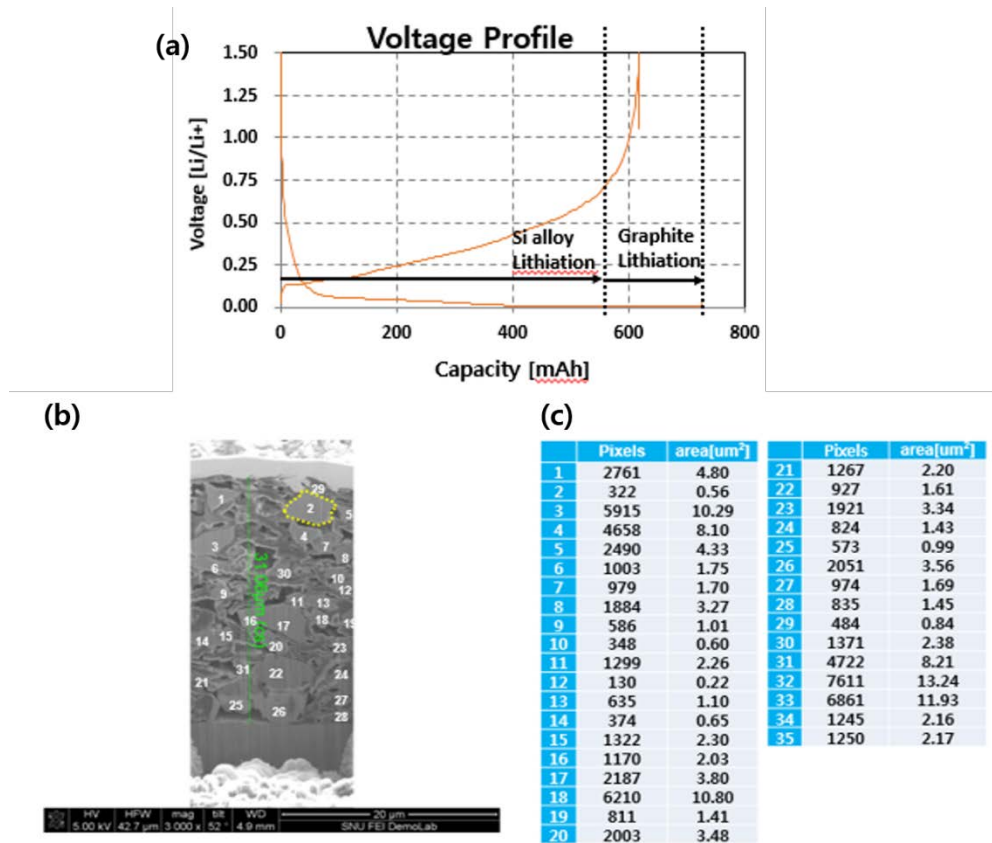


Figure 2.1 (a) Voltage profile of Step sequence discharge state between Si alloy and Graphite (b) Si particle area measurement using image processing in cross-sectional image. (c) Pixels and area measurement data of each Si particle

2.3 Results and discussion

2.3.1 Microstructural change of MA Si alloy

In the case of Silicon alloy formed by melt spinning, has large grain size (over 200nm) and clearly identified between free silicon area and matrix. [22] Large size Si grain causes dramatically volume expansion. In addition, grain size is different between wheel side and air side. Because cooling rate of air side is lower than wheel side, lower cooling rate makes it easy to growth Si dendrite at air side. In case of mechanical alloying process, it has very small amorphous free Si grain (5 ~ 20 nm) and uniform structure. . In addition, it is very hard to identify between amorphous Si and crystalline Fe-silicide area. Stress caused by volume expansion and imbalance are minimized by improving micro structural properties. Figure 2.2 (a~b)

In high resolution images of MA Si alloy, amorphous Si forming continuous phase, and silicide exist independent nano-particles. Continuous amorphous Si phase is role as a path of Li transparent and Fe-silicide that has no reactivity with Li is as a role of stress relaxation induced by Si volume expansion. 2.3 (a~b)

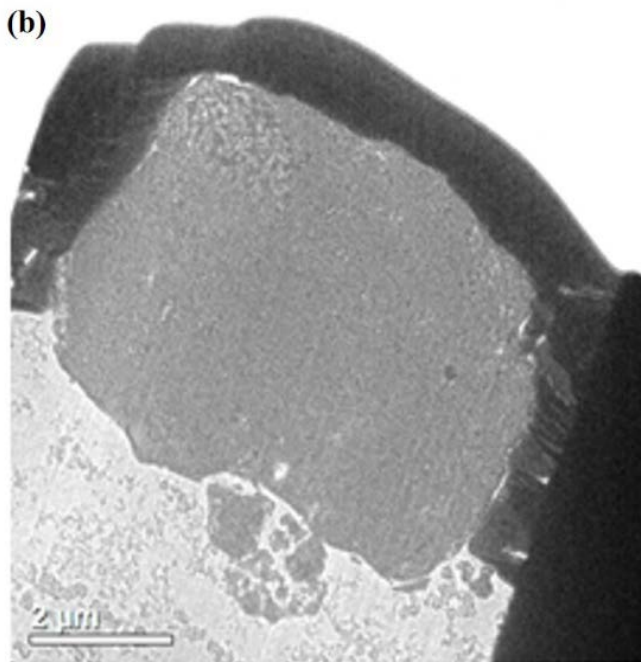
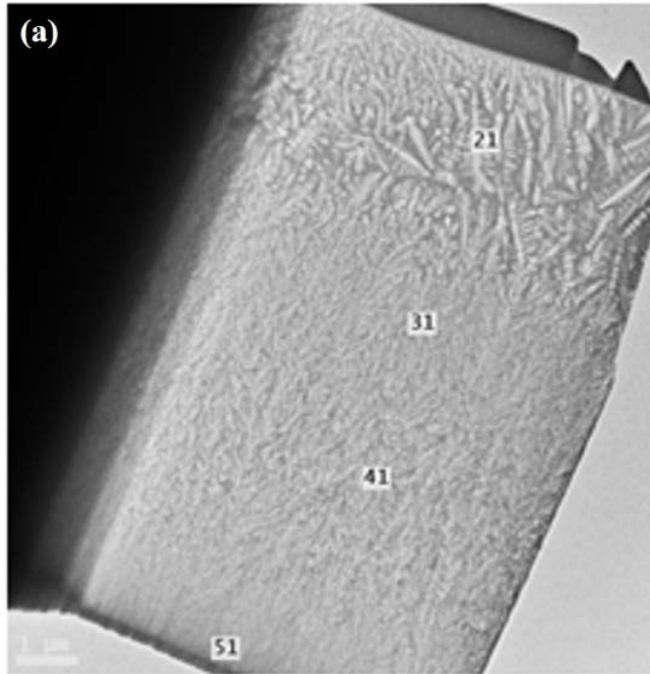


Figure 2.2 (a) TEM micrograph of the Melt spun Si alloy (b) TEM micrograph of the ball milled alloying Si alloy

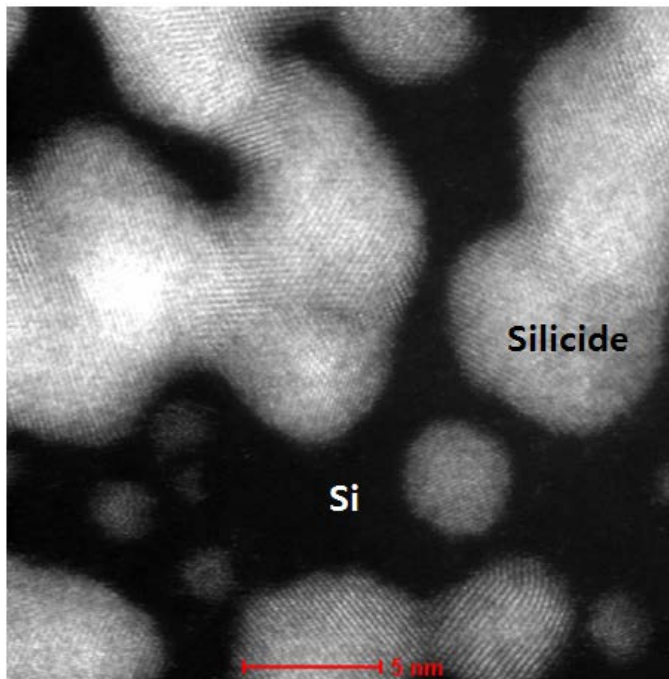
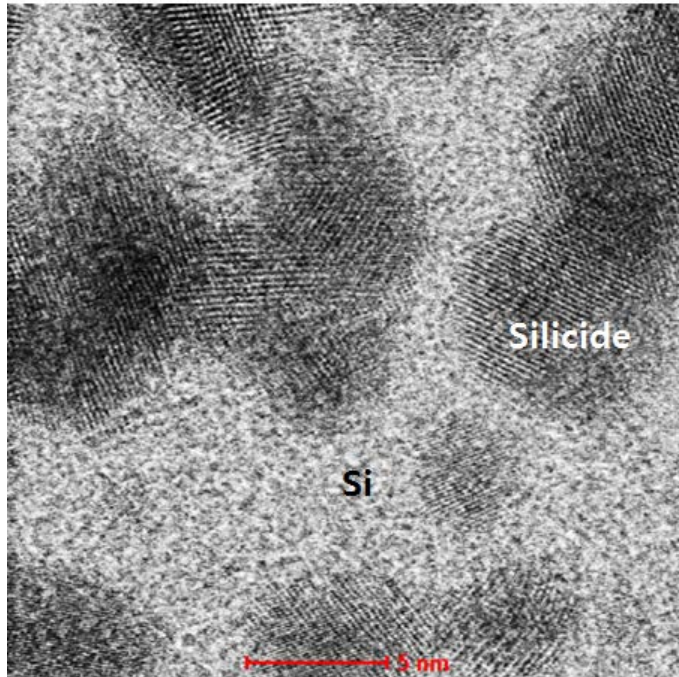


Figure 2.3 (a) cS corrected high resolution TEM micrograph of ball milled alloying Si alloy (b) cS corrected high resolution STEM micrograph of same area

Figure 2.4 (a) is a result of the life cycle test of MA Si alloy. (Graph of sample 1) It has shown a high capacity retention ratio of more than 85 percent at 100 cycles. Through the microstructure analysis with cycle progress, initial state microstructure is maintained after long life cycle. (100cycle) Figure 2.4 (b~d) shows there are no significantly micro structural changes in MA alloy systems with cycle progress.

Figure 2.5 (a~c) are TEM images of the surface of the particles with the cycle. Although microstructure of inside particle is maintained but SEI layers are formed around the Si alloy particle. SEI layers are formed by side reaction of Si between liquid electrolytes. Forming SEI layer is irreversible reaction, it cause depletion of the electrolyte. Figure 2.6 (a) is a TEM image of electrolyte penetration inside particle. Figure 2.6 (b~e) are TEM EELS elemental analysis images that shows SEI layer formed inside of particle by loosely bonding of Si alloy. If Si alloy particles have strong bonding force, SEI layer formed only surface with cycle progress and have good cycle performance. However, particles has weak bonding force, electrolyte penetrate inside of the particles and formed very large SEI layer area rapidly and shows very poor life cycle performance.

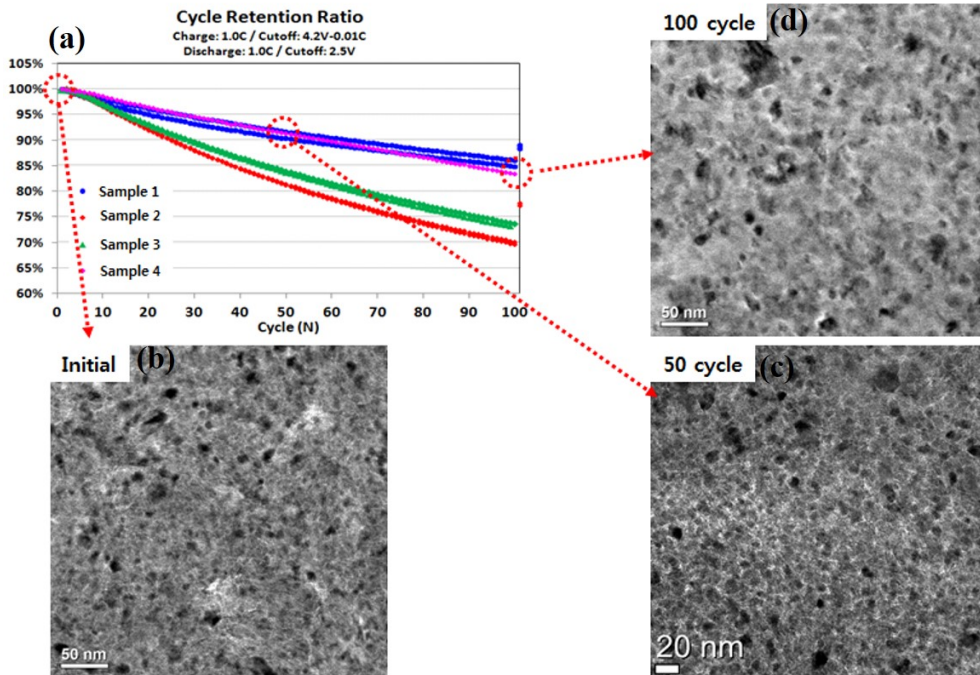


Figure 2.4 (a) Results of life properties of MA Si-Fe alloy (sample 1). (b) TEM micrograph of initial ball milled alloying Si (c) TEM micrograph of 50 cycled

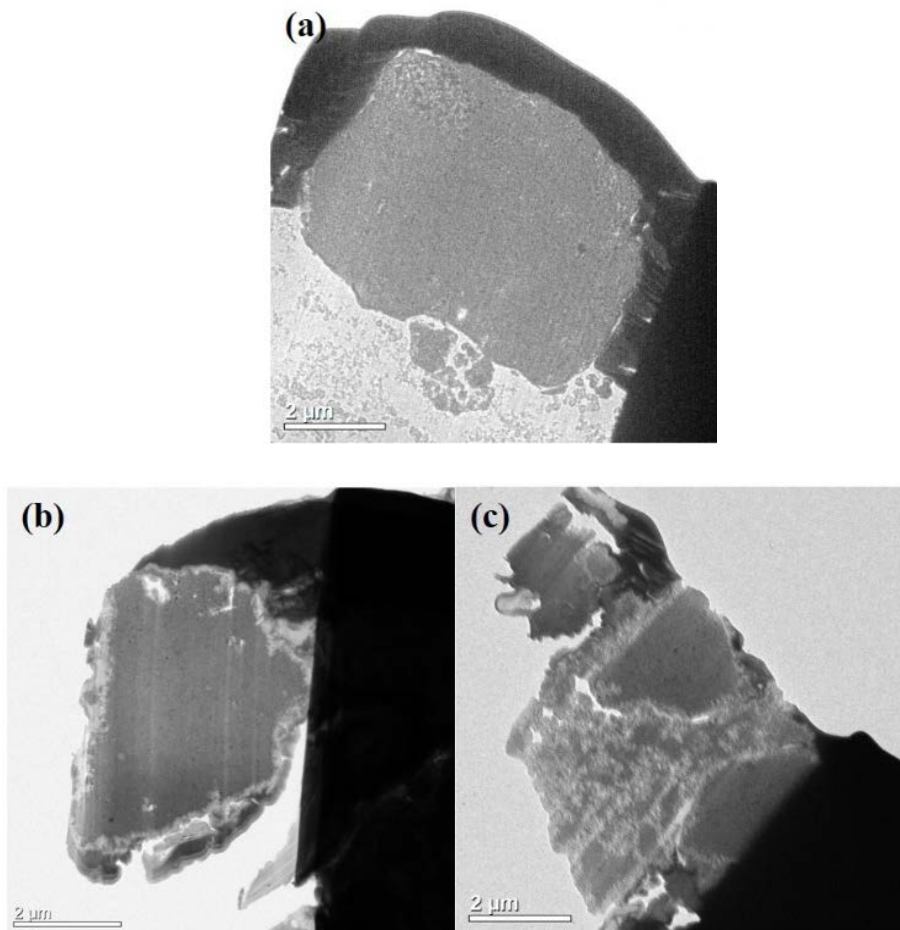


Figure 2.5 (a) TEM micrograph of initial ball milled alloying Si particle. (b) TEM micrograph of 50 cycled ball milled alloying Si particle (c) TEM micrograph of 100 cycled ball milled alloying Si particle

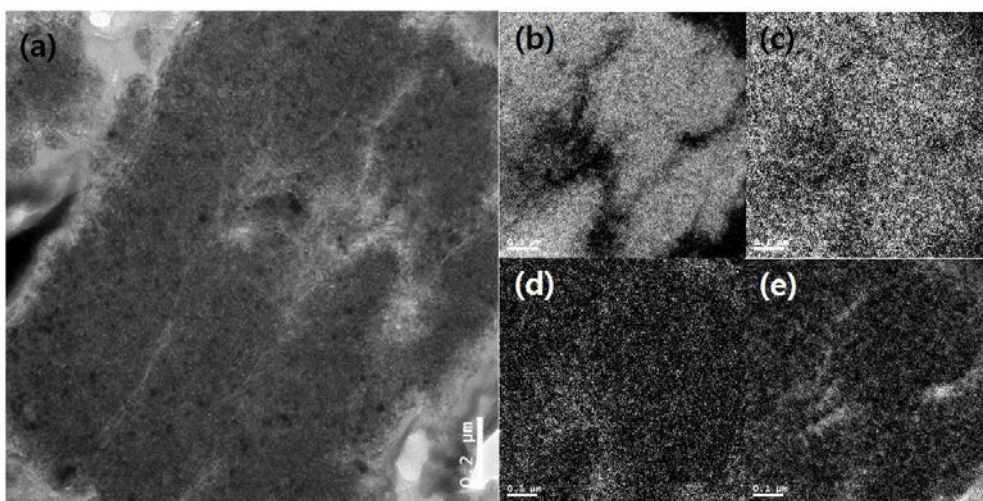


Figure 2.6 (a) EELS zero-loss map of SEI layer formed inside of particle. (b) EELS Map of Si (c) EELS Map of Fe (d) EELS Map of O (e) EELS Map of C

MA particles (3~5 μ m) are secondary agglomerate of primary particles (200~500nm) that is formed with well mixed continuous phase amorphous free Si and crystalline silicide particles. (5~20nm) After 1st step ball milling in order to crushing Si and Si particles and amorphizing of Si, secondary particles have very porous structure. Pores of inside secondary particle cause dramatically decreasing of life cycle performance by penetration of liquid electrolyte inside particles. In order prevent forming inside pores, enhancing bonding force is required. C coating on primary particle can improve bonding force by forming C-C bonding between primary particles. Carbon coating process is low energy ball milling with primary particles and graphite that is carbon source. Figure 2.7 (a) is a conceptual illustrate of mechanism for improve bonding force by carbon coating as a bonding phase. Carbon layers are formed on surface of primary particles. Crashing with another C coated particles formed strong C-C bonding, and it densifies secondary particle. Figure 2.7 (b~c) Figure 2.7 (d) is a TEM images of initial graphitic carbon filled with void of secondary particle and maintained after 100 cycles. Figure 2.7 (e)

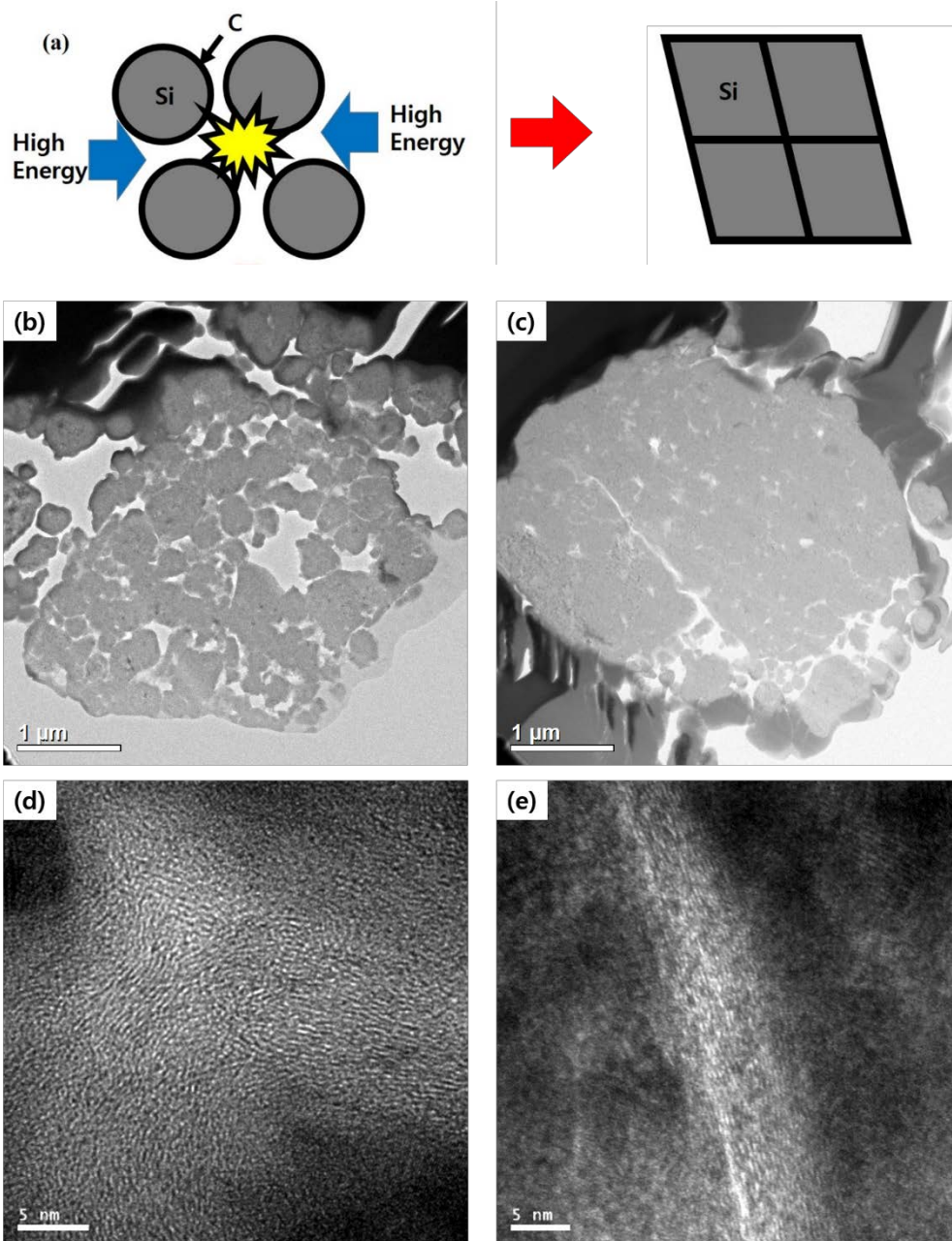


Figure 2.7 (a) Concept illustrate of Carbon as bond phase (b) TEM BF image of secondary particle before C coating (c) after C coating. (d) TEM BF image of initial C coating area of inside particle (e) after 100 cycles

2.3.2 Volume expansion behavior of electrode materials

Since discharge voltage of Si is higher than graphite, Si alloys are expanded earlier than graphite. It is possible to analyze individual expansion behavior of Si and graphite. Figure 2.8 shows expansion ratio of electrode and Si alloy during 3 cycles. Expansion ratio of electrode is sum of Si alloy's and graphite's. Expansion ratio of electrode value is existed in 50-70% range when charged and in 10-30% range when discharged. In the contrary, in case of the Si alloy, expansion ratio value is in 15-20% range after 1st lithiation and maintained. This results shows expansion of the electrode is affected not only Si alloys but also graphite. Expanded Si alloy state is maintained regardless of state, it describes Li ions are remaining in Si alloy particles at discharge state after 1st lithiation. Li_xSi is known as very unstable phase, so it can be expected that Li ions are remaining in matrix area.

Figure 2.9 is a schematic view of the role of matrix with lithium remaining. (a) 1st lithiated state, Si particles form Li_xSi phase with electrochemically inserted Li ions and Si included matrix is lithiated at same time. (b) At delithiated state Li_xSi separated Si and Li ions, but Li ions in matrix area are remaining. That is expected irreversible reaction. Since remained Li ions in matrix, Si alloy particles are remained expanded state. After 1st cycle Si included matrix as a role of solid state electrolyte for Li transport to free Si inside of alloy particle.

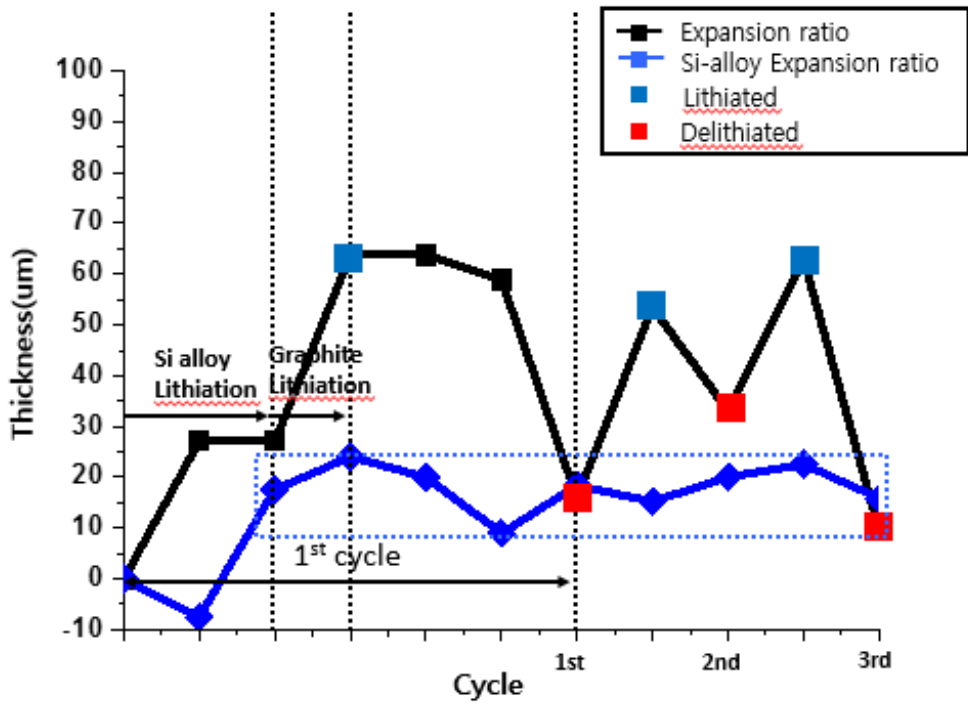


Figure 2.8 Expansion ratio of Electrode (Black line) and Si alloy (Blue line) with cycle progress

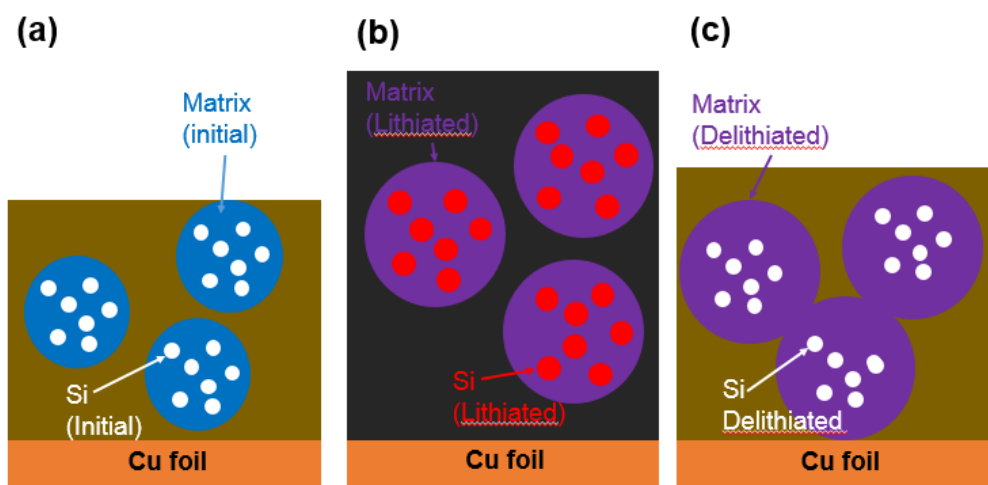


Figure 2.9 Concept illustrate of Si alloy expansion at delithiated state by inactive matrix lithiation, (a) Initial state of Si alloy (b) Lithiated state of Si alloy (c) Delithiated state of Si alloy

Figure 2.10 (a~e) prove matrix becomes solid state electrolyte during cycle. Li is detected only matrix area after 1st lithiation. Li ions in matrix are remained after 200 cycles It is expected that Li_xSi is separated during TEM sampling or TEM analysis using ion/electron beams. is possible to prove to those observed in the matrix area, in the case of a Si alloy as Figure 2.10 (f) shows, initial capacities are different between theoretical and measured. Measured capacity is about 150mAh/g larger than the theoretical capacity. And measured capacity of matrix is about 210mAh/g and decreased 150mA/g in few cycles. 60mAh/g is from carbon for conductivity, 150mAh/g is from lithiated matrix area. [20,22]

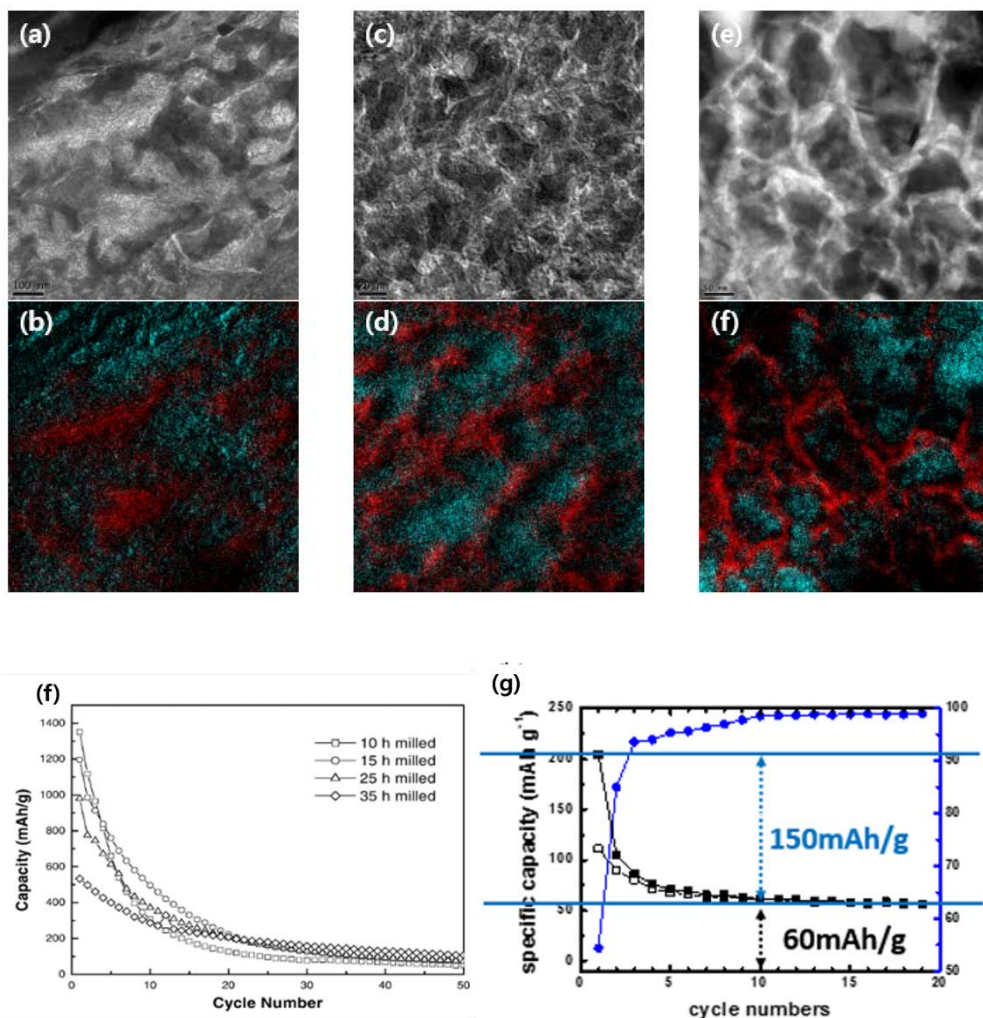


Figure 2.10 Zero-loss and EELS mapping image of Si alloy during cycle (a) 1st lithiated zero-loss image of Si alloy (White Si, Black matrix) (b) 1st lithiated EELS mapping image of Si alloy (R : Si, B: Li) (c) 50 cycled zero-loss image of Si alloy (White Si, Black matrix) (d) 50 cycled EELS mapping image of Si alloy (R : Si, B: Li) (e) 200 cycled zero-loss image of Si alloy (White Si, Black matrix) (f) 200 cycled EELS mapping image of Si alloy (R : Si, B: Li) (f) Cycle-Capacity graph of Si-alloy (g) Cycle-Capacity graph of matrix only.

2.4 Conclusion

Si alloying process is mechanical alloying process using high energy ball milling. MA Si alloys are composed amorphous free Si and Fe-Silicide. Continuous amorphous Si phase is role as a path of Li transparent and Fe-silicide is as a role of stress relaxation induced by Si volume expansion.

In order to enhancing life cycle performance, grain size refinement, well mixed uniform structure and strong bonding force between primary particles are required. Stress from volume expansion is relaxed with ultrafine free Si and Fe-Silicide. Their grain size is under 20nm. Uniform microstructure can prevent occurring imbalance stress. Imbalance stress cause mechanical fracture. Carbon coating process increase bonding force between primary particles. After carbon coated secondary particle has lower porosity than before coating process. Since dense particles are less exposed to electrolyte, it prevent forming SEI layer inside of secondary particle. In this study stable Si alloy microstructure for enhanced life cycle performance derived.

In this study, we measured the expansion behavior of the electrode materials using discharge voltage difference. Expansion of the electrode is not only Si alloy, the expansion of the graphite also have a significant impact.

Matrix of Si alloy to the role of the solid electrolyte to transfer Li ion to inside free Si particles during Lithiation. Lithiation of matrix is a irreversible reaction, expansion state is maintained after delithiation

2.5 Reference

- [1] J. M. Tarascon , M. Armand , Nature 2001 , 414 , 359.
- [2] C. K. Chan , H. L. Peng , G. Liu , K. McIlwrath , X. F. Zhang , R. A. Huggins ,
Y. Cui , Nat. Nanotechnol. 2008, 3, 31.
- [3] T. D. Hatchard, J. R. Dahn, J. Electrochem. Soc. 2004, 151, A838.
- [4] M. N. Obrovac, L. Christensen, Electrochem. Solid State Lett. 2004, 7, A93.
- [5] A. H. Mayne, S. C. Bayliss , P. Barr , M. Tobin , L. D. Buckberry , Phys.
Status Solidi A-Appl. Res. 2000, 182, 505.
- [6] U. Kasavajjula , C. S. Wang , A. J. Appleby , J. Power Sources
2007, 163, 1003.
- [7] S. Golmon, K. Maute, S. H. Lee, M. L. Dunn , Appl. Phys. Lett. 2010, 97.
- [8] S. B. Son , J. E. Trevey , H. Roh , S. H. Kim , K. B. Kim , J. S. Cho,
J. T. Moon, C. M. DeLuca, K. K. Maute , M. L. Dunn , H. N. Han,
K. H. Oh, S. H. Lee, Adv. Energy Mater. 2011, 1, 1199.
- [9] V. A. Sethuraman, M. J. Chon, M. Shimshak , V. Srinivasan ,
P. R. Guduru, J. Power Sources 2010, 195, 5062.
- [10] S. D. Beattie, D. Larcher, M. Morcrette, B. Simon, J. M. Tarascon,
J. Electrochem. Soc. 2008, 155, A158.
- [11] J. E. Trevey, K. W. Rason, C. R. Stoldt, S. H. Lee, Electrochem. Solid
State Lett. 2010, 13, A154.
- [12] H. Kim, J. Cho, Nano Lett. 2008, 8, 3688.

- [13] X. H. Liu , L. Q. Zhang , L. Zhong , Y. Liu , H. Zheng , J. W. Wang ,
J. H. Cho, S. A. Dayeh, S. T. Picraux, J. P. Sullivan, S. X. Mao,
Z. Z. Ye, J. Y. Huang, *Nano Lett.* 2011, 11, 2251.
- [14] A. Magasinski, P. Dixon, B. Hertzberg, A. Kvit, J. Ayala, G. Yushin,
Nat. Mater. 2010, 9, 353.
- [15] H. Jung, Y. U. Kim, M. S. Sung, Y. Hwa, G. Jeong, G. B. Kim,
H. J. Sohn, *J. Mater. Chem.* 2011, 21, 11213.
- [16] H. T. Nguyen, F. Yao, M. R. Zamfir, C. Biswas, K. P. So, Y. H. Lee,
S. M. Kim, S. N. Cha, J. M. Kim, D. Pribat, *Adv. Energy Mater.*
2011, 1, 1154.
- [17] B. S. Lee, S. B. Son, K. M. Park, W. R. Yu, K. H. Oh, S. H. Lee,
J. Power Sources 2012, 199, 53.
- [18] L. Q. Mai, B. Hu, W. Chen, Y. Y. Qi, C. S. Lao, R. S. Yang, Y. Dai,
Z. L. Wang, *Adv. Mater.* 2007, 19, 3712.
- [19] L. Q. Mai , L. Xu , B. Hu , Y. H. Gu, *J. Mater. Res.* 2010, 25, 1413
- [20] Heon-Young Lee, Sung-Man Lee, *Journal of Power Sources*
112 (2002) 649.
- [21] Xiao Hua Liu, Yang Liu, Akihiro Kushima, Sulin Zhang, Ting Zhu, Ju Li,
and Jian Yu Huang, *Adv. Energy Mater.* 2012, 2, 722–741
- [22] N. S. Choi, K. H. Yew, K. Y. Lee, M. Sung, H. Kim, S. S. Kim , *J. Power
Sources* 2006, 161, 1254.

[23] Seoung-Bum Son, Seul Cham Kim, Chan Soon Kang, Thomas A. Yersak,
Yoon-Chang Kim, Chun-Gyoo Lee, Sung-Hwan Moon, Jong Soo Cho,
Jeong-Tak Moon, Kyu Hwan Oh , and Se-Hee Lee, *Adv. Energy Mater.*
2012, 2, 1226–1231

Chapter 3. Surface modification for enhancing the life property of Si anode

3.1 Introduction

3.1.1 Previous study with Carbon coating on Si

Si-C nano-composites may be promising candidates for viable, inexpensive, stable and efficient high capacity anodes. Si-C conventional composites are typically prepared by carbonizing precursors [1-4] or by mechanically mixing Si with carbon. [5-6] The result are composites of Si particles embedded in carbon matrix.

By cyclizing commercially available polyacrylonitrile (PAN), we show that it is possible to conformally coat nanoparticles of Si with a conjugated polymer. We utilize cyclized-PAN both as a binder and conductive additive because of its good mechanical resiliency to accommodate silicon's (Si) large expansion as well as its good ionic and electronic conductivity. As we will show, the superior performance of our nano-Si/cyclized-PAN composite electrodes is enabled by the unique material properties of cyclized-PAN coatings.

3.1.2 Effect of ionic liquid electrolyte

Si anodes suffer extensively from a dynamic SEI that must reform each cycle as expansion during lithiation causes the layer to break. [7-9] Formation of the SEI consumes Li^+ and depletes electrolyte during every cycle. [10] In the effort to design next-generation electrolyte materials, room temperature ionic liquids (RTILs or ILs) are of particular interest due to their low volatilities, negligible vapour pressures,

thermal stabilities, high-voltage stability windows and sufficient ionic conductivities. [11] For enhancing life cycle performance of Si anode, we have designed a Si-RTIL system that exhibits a highly stable and resilient SEI, providing a solution to the drawbacks of the Si-anode and enabling the long term operation of a lithium-ion cell.

3.2 Experimental procedure

3.2.1 PAN coating

PAN ($M_w = 150,000\text{g/mol}$, Sigma-Aldrich) was mixed with 50 nm diameter crystalline Si particles (Alpha Aesar) in a 3:7 mass ratio respectively using a mortar and pestle. The mixture was then dissolved in N, N-dimethylformamide (DMF, 99%) such that 87.5 wt% of the final solution/suspension was solvent. The solution/suspension was then mixed via magnetic stirring for about 12 hours to produce a viscous slurry that was bladed onto a copper foil current collector and dried at 80°C for about 3 hours. The subsequent electrode film was then calendared before a PAN cyclization heat treatment at 300°C inside an Ar-filled glove box for about 12 hours.

3.2.2 Electrochemical test & Analysis of Microstructure

Electrochemical measurements were carried out using an Arbin TM 2000 battery test station. All cells were assembled in an Ar-filled glove box using our prepared nano-Si/ cyclized-PAN electrodes as the working electrode and lithium metal foil as the counter electrode. The electrolyte was 1M LiPF₆ dissolved in a 1:1 (volume ratio) mixture of ethylene carbonate (EC) and diethyl carbonate (DEC), the separator was

a glass micro-fiber disk (Whatman TM GF/F) and the shell was a stainless steel CR2032 coin cell (VWR Inter.). The cells were discharged (lithiated) and charged (delithiated) with various cycling currents between 0.05 and 1 V (vs. Li/Li +). Charging was conducted with constant current (CC) and discharge was conducted with CCCV cycling parameters.

A FIB (FEI, NOVA200 dual beam system) equipped with an air-lock chamber is used for TEM sample preparation. [12] TEM and EELS analysis was performed with a FEI Tecnai F20 operated at 200 keV. A detailed description of our TEM and EELS characterization procedures can be found elsewhere. [13]

3.2.3 Applying Ionic liquid electrolyte

Ionic liquid electrolytes were provided by Boulder Ionics Corporation (USA). One molar LiPF₆ in ethylene carbonate:diethyl carbonate (50:50, Soulbrain) was used as a conventional organic electrolyte.

The half-cells were then disassembled and the electrodes were used to fabricate 2032 coin-cell (Al-clad cathode cup) type full-cells. This method of pre-conditioning allows for full control of the amount of lithium in the system.

3.3 Results and discussion

3.3.1 Conformal carbon coating on Si nano particle

In conformal C coatings on Si anode study, to characterize the microstructure of our nano-Si/cyclized-PAN electrodes we used transmission electron microscopy (TEM)

and electron energy loss spectroscopy (EELS). TEM samples were prepared using a focused ion beam (FIB) equipped with a mobile air-lock chamber. [12] **Figure 3.1** shows TEM micrograph (a) and an EELS (b) elemental map of an uncycled nano-Si/cyclized-PAN electrode. We observe a conformal thin coating (under 5nm) of cyclized-PAN (cyan) on nano-Si particles (red). The coating provides an intimately linked conductive network that connects nano-Si particles throughout the electrode. To confirm that the PAN coating contains delocalized $sp\pi$ bonding, we used Raman to characterize our electrodes. Figure 3.1 (c) presents the Raman spectra for nano-Si electrodes with coatings of untreated PAN (red profile) and PAN cyclized at 300°C (cyan profile). As expected, both samples exhibit a shift attributed to Si at 520/cm. And like the Raman analysis of 1–5 μ m PAN films, only the electrode treated at 300°C exhibits the D and G delocalized $sp^2\pi$ bands. From this result we conclude that nano-Si is coated with an electronically conductive and mechanically resilient cyclized-PAN conformal coating.

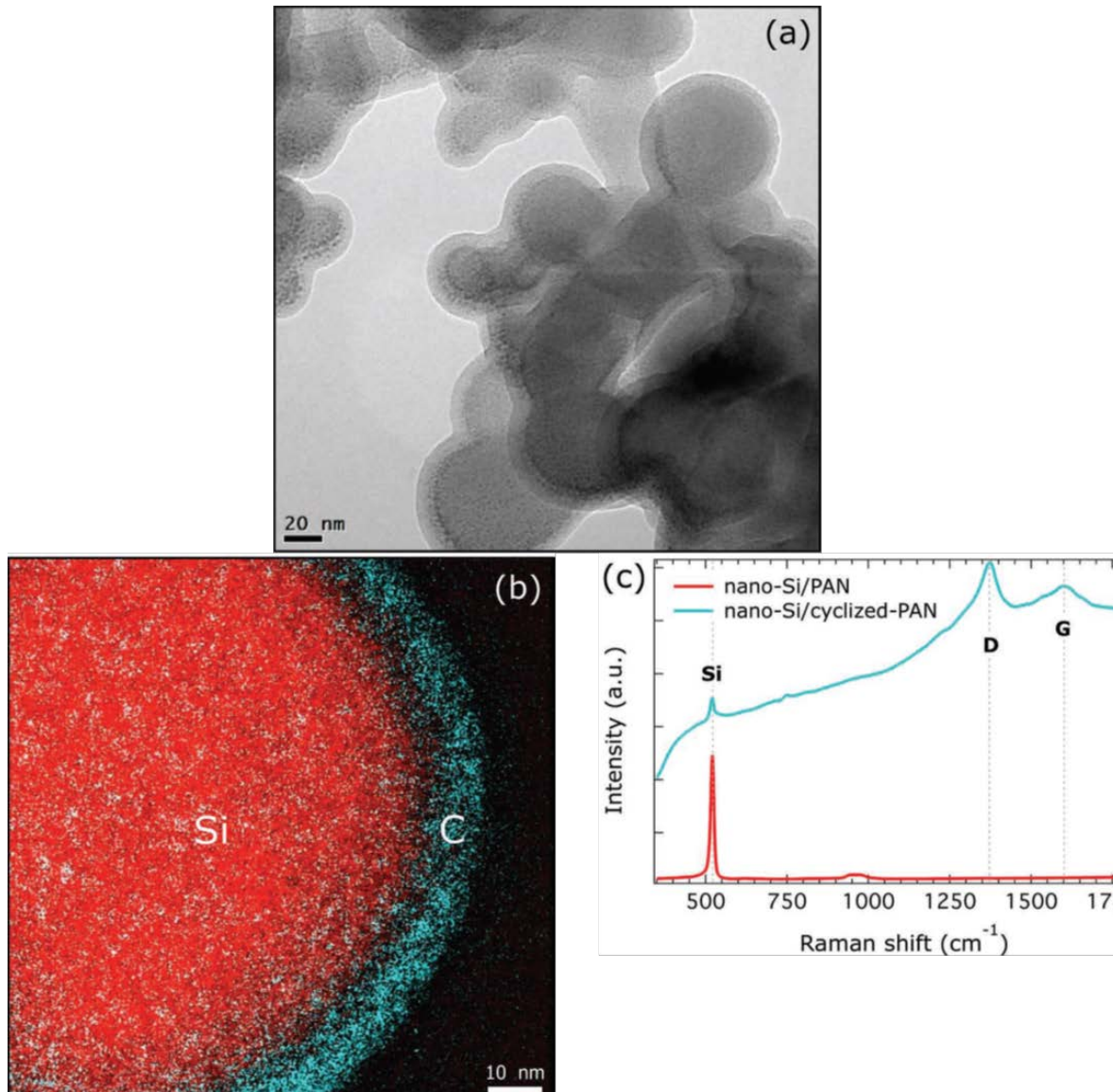


Figure 3.1(a) TEM micrograph of the uncyclized nano-Si/cyclized-PAN electrode with (b) EELS elemental mapping confirming that we achieve a conformal 5 nm thick cyclized-PAN coating. (c) Raman spectra for an untreated electrode (red) and for an electrode treated at 300°C (cyan). The delocalized $sp^2\pi$ D and G bands present in the spectra

Results of our electrochemical characterization are presented in Figure 3.2. Figure 3.2 (a) presents the cyclic stability of our nano-Si/cyclized-PAN anode treated at 300°C. The electrode was run at a rate of C/20 for the first 10 cycles and a rate of C/10 for all subsequent cycles. At cycle 150 our nano-Si/cyclized-PAN cell exhibits a specific charge capacity of nearly 1500 mAh/g with a CE approaching 100%. 1500 mAh/g corresponds to an electrode volumetric capacity of 620 mAh/cm³ considering an initial electrode thickness of 9.08µm. Figure 3.2 (a). Such good cycle life and CE is evidence that the cyclized-PAN coating has good mechanical resiliency. Figure 3.2 (b) displays the 1st, 3rd , 10th , 30th , 40th , and 5th voltage profiles of our nano-Si/cyclized-PAN anode. The first cycle profile shows a specific charge capacity of 2585 mAh/g, which is equivalent to the extraction of 2.7 mole Li per mole of Si. At cycle 50, the specific charge capacity is 2078 mAh/g (2.2 mole Li).

We also conducted a rate test to study the transport properties of our cyclized PAN films. Figure 3.2 (c). At a rate of 5C, our nano-Si/cyclized-PAN electrode exhibits a specific charge capacity in excess of 2300 mAh/g. If the coating did not provide adequate ionic and electronic transport, it is reasonable to conclude that we would not have been able to achieve such high charging capacities at a rate of 5C. At this time, an ionic transport mechanism for the cyclized-PAN coatings has yet to be elucidated. However, other amorphous, thin coatings have been shown to be ionically conductive despite being ionically resistive in the bulk form. [13] We characterized the microstructural properties of our nano-Si/cyclized-PAN electrodes using TEM to verify the mechanical resiliency of our cyclized-PAN coating.

Figure 3.3 (a~b) present SEM micrographs of electrode cross-sections before and

after initial lithiation, respectively. Before cycling, the electrode has good porosity and an overall thickness of 9.08 μm . After full lithiation at a rate of C/20, the electrode expands in overall thickness to 12.75 μm . Si's expansion is largely accommodated by the porosity of the electrode such that the electrode only expands by 40%. However, the porous structure reopens upon delithiation after 20 cycles indicating that ionic transport pathways are maintained. Figure 3.3 (c). To confirm that cyclized-PAN coatings conform to the strains of lithiated Si, an electrode was recovered after its 20th cycle. This electrode was cycled at a slower rate of C/30 for the first cycle and C/20 for subsequent cycles to fully lithiate Si and expose the cyclized-PAN $\sim 5\text{nm}$ coating to a condition of maximum stress and strain. Even after extensive cycling, the cyclized-PAN coating and the Si nanoparticles display no evidence of cracking nor does the cyclized-PAN/Si interface show signs of delamination Figure 3.3 (d~e). The superior resiliency of our cyclized-PAN coating successfully accommodates Si expansion where previously reported dense carbon matrices would have experienced brittle failure. We believe that the conformal cyclized-PAN coating isolates nano-Si from the organic liquid electrolyte and inhibits nano-Si aggregation during cycling. Isolation of nano-Si from the electrolyte prevents the parasitic formation of a SEI and improves CE. Material aggregation is a frequent cause of capacity fade in electrodes utilizing nano-particles, [15-16] but our cyclized-PAN coating confines nano-Si for good capacity retention.

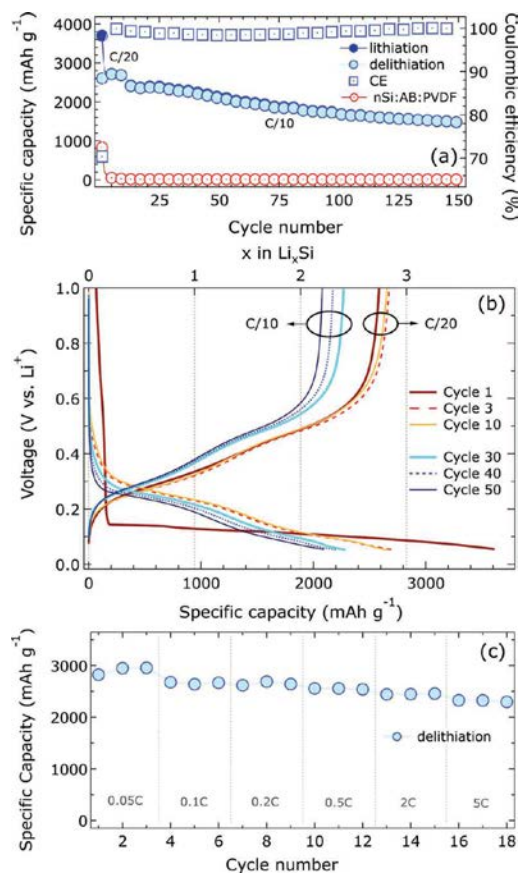


Figure 3.2 (a) Cyclic capacity (blue circles) and CE (blue squares) of nano-Si/cyclized-PAN electrodes run at a rate of C/20 for the first 10 cycles and at C/10 for subsequent cycles. A conventional nano-Si electrode (red circles) was cycled at a rate of C/10 as a control cell. After 150 cycles, our nano-Si/cyclized-PAN composite electrode has a specific charge capacity of nearly 1500 mAh/g and a CE approaching 100%, whereas the conventional electrode fails after 3 cycles. (b) Voltage profiles of our nano-Si/cyclized-PAN electrode showing a minimal overpotential when cycled at C/10 compared to C/20. (c) A rate test demonstrates that our nano-Si/cyclized-PAN electrodes can achieve a specific charge capacity in excess of 2300 mAh/g at a rate of 5C.

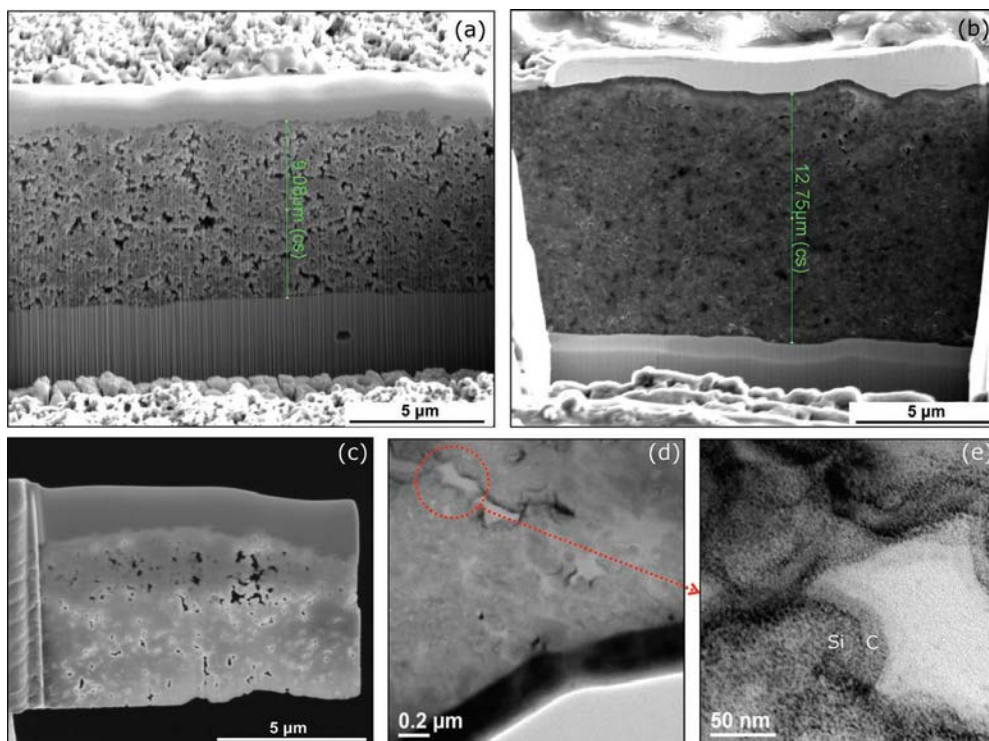


Figure 3.3 (a), (b) TEM micrographs of a nano-Si/cyclized-PAN electrode cross-sections before and after initial lithiation, respectively. Si's expansion is largely accommodated by the porosity of the electrode such that the electrode only expands by 40%. (c) The porous structure reopens upon delithiation after 20 cycles indicating that ionic transport pathways are maintained. (d), (e) TEM micrographs of a delithiated nano-Si/cyclized-PAN electrode collected after its 20th cycle. We observe that the cyclized-PAN coating does not delaminate from Si particles nor does it crack.

3.3.2 Forming stable SEI by ionic liquid electrolyte

In ionic liquid electrolyte study, half-cell electrochemical characterization. The cycling performances of the Si-based electrode in RTIL solutions, including PYR13FSI (1.2M LiFSI), PYR13TFSI (0.6M LiTFSI) and EMIMFSI (1.2M LiFSI), were directly compared with the electrode performance in the commercial EC/DEC (1M LiPF₆) electrolyte. The results of the preliminary cycling study are presented in Fig. 2.2.4, demonstrating the exceptional cycling stability of the nSi-cPAN anodes in FSI_-based ILs and their unprecedented CE in the PYR13FSI system. The high CE manifested in the PYR13FSI (1.2M LiFSI) electrolyte stabilizes after 8 cycles, with an average stable CE of 99.945% and a charge capacity retention of 76.7% after 100 cycles (blue profiles, Figure 3.4 (a)). While exhibiting stable half-cell cycling, the lower average CE (98.451%) observed using an EMIMFSI (1.2M LiFSI) electrolyte (orange profiles, Figure 3.4(b)) is ascribed to the instability of the EMIM⁺ cation below 1.5V (versus Li/Li⁺). [17] Such impressive data contrast that of the cycling behavior of our nSi-cPAN electrode in a conventional organic electrolyte, which maintains only 45.2% of its initial charge capacity after 100 cycles with an average stable CE of 97.824% (red profiles, Figure 3.4 (a)), and the rapid capacity fade and low-active material utilization in a TFSI_-based IL (green profiles, Figure 3.4(b)). The unparalleled CEs of the Si-PYR13FSI system are attributed to the formation of a highly stable SEI.

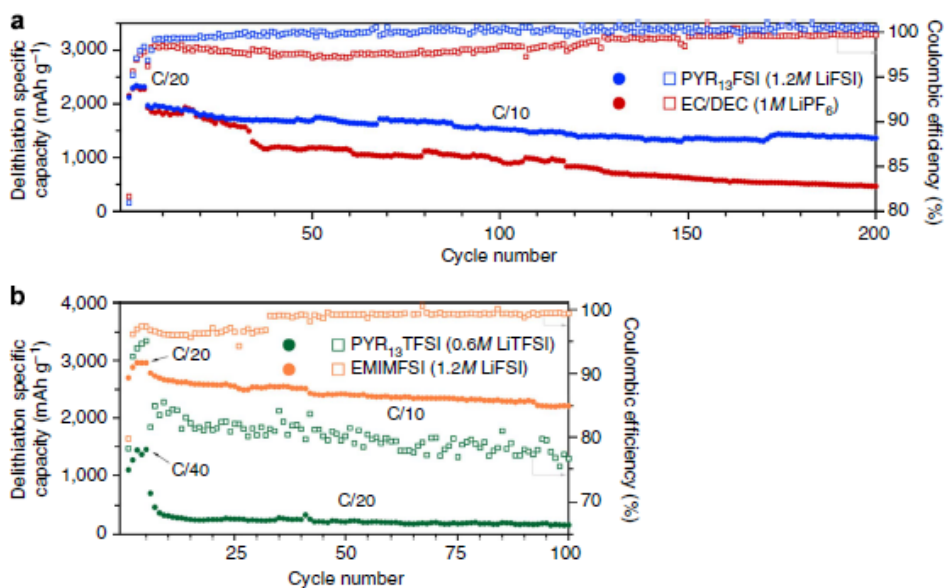


Figure 3.4 Galvanostatic performance of various electrolyte systems with nSi-cPAN. (a) Specific capacities and coulombic efficiencies of nSi-cPAN electrode in PYR13FSI (1.2M LiFSI) and EC/DEC (1M LiPF₆). (b) Specific capacities and coulombic efficiencies of nSi-cPAN electrode in PYR13TFSI (0.6M LiTFSI) and EMIMFSI (1.2M LiFSI) electrolyte systems. Cycling was carried out at room temperature in 2032 coin-type half-cells operated between 0.05 and 1V (versus Li/Li₂O).

Interfacial topography and composition. By using electron energy loss spectroscopy (EELS) to study the elemental composition of the surface of nSi-cPAN particles during cycling (16th delithiation), we confirm our DFT predictions and gain insight into the elemental constitution and topography of the proposed SEI. Figure 3.5 displays high-resolution transmission electron microscopy (HRTEM) images of the cycled/delithiated nSi-cPAN cross-section (b) with EELS mapping of silicon (a), carbon (c), sulfur (e), fluorine (g), lithium (i) and oxygen (k). The well-defined silhouette of F coating the surface of the Si particles, in combination with the presence of Li, provides further evidence of an SEI composition containing LiF [18-19], as proposed in literature [20-21] and found in our DFT simulations. Moreover, the clear mapping of O over the cPAN surface coating and evidence of S correlates with the proposed reaction of previously determined FSI₊-breakdown products, such as SO₂ and LiO [20-22]. Similar analysis of a conventional Si-based electrode cycled in conventional, organic electrolyte shows no specific adherence of electrolyte

To elucidate the precise chemical composition of the proposed SEI, X-ray photoelectron spectroscopy (XPS) is utilized to verify the chemical bonding environments of the species observed physically with EELS and simulated through DFT. Alongside our EELS characterization, Figure 3.5 displays the deconvolution of the C 1s (d), S 2p (f), F 1s (h), Li 1s (j) and O 1s (i) XPS spectra. Deconvolution of the C 1s spectrum shows a chemical environment consistent with that of the cyclized-PAN coating, dominated by the decomposition of and formation of ladder-like structures of thermally stable pyridine rings, C-N^{1/4}C, and conjugation of the backbone, C^{1/4}C. [23] Deconvolution of the F 1s and Li 1s spectra provide direct

chemical evidence of the formation of an SEI composition containing LiF and lithium-oxygen containing species (that is, LiO, LiOH), consistent with previous studies of SEIs formed by (fluorosulfonyl)imide-based RTILs. [20-21]

Moreover, the deconvolution of the S 2p and O 1s spectra reveals evidence of the detachment and reaction of the SO₂ group from FSI_ breakdown, confirming our DFT simulation and our EELS elemental mapping, in which the presence of sulfur- and oxygen-containing species was observed. The S 2p spectrum clearly shows the presence of SO₂ and its reaction on the surface of the particles to form sulfates, sulfites and sulfides, consistent with other works [20-22]. In addition to revealing the formation of sulfates, such as Li₂SO₄ [22], and lithium-oxygen species, the deconvolution of the O 1s spectra affirms the formation of carbon-oxygen components assigned to the reaction of O with the cPAN coating, suggesting the interaction of the SEI components with the coated electrode surface.

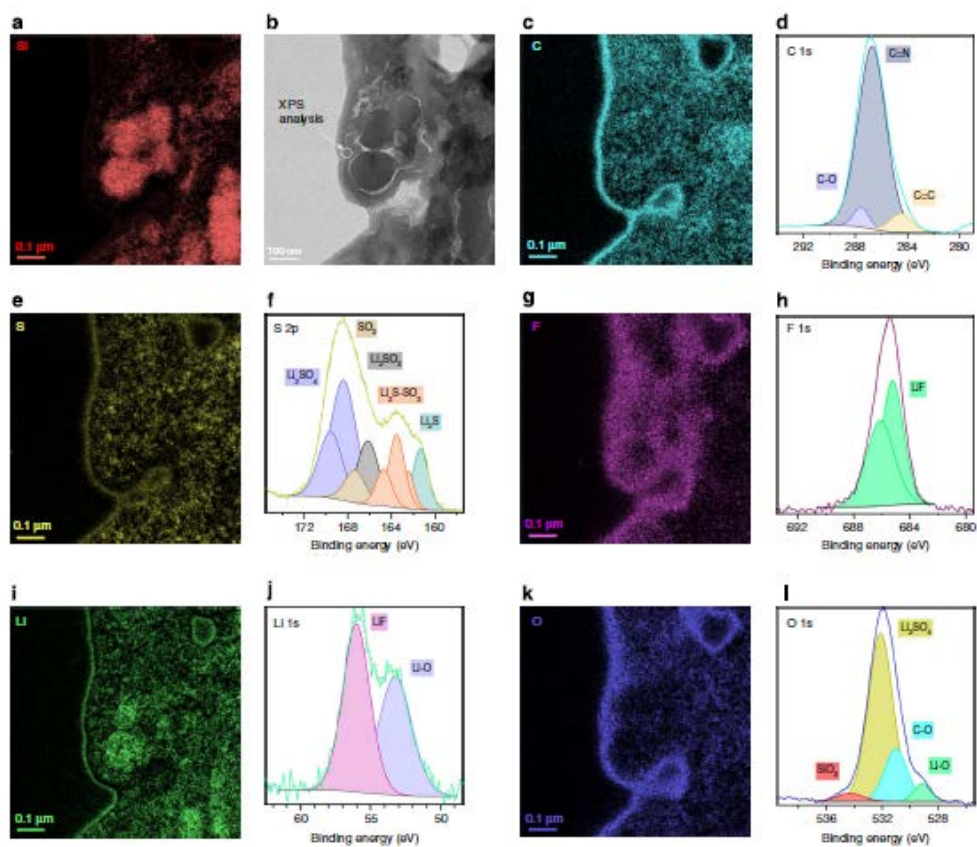


Figure 3.5 Solid-electrolyte interphase composition of the Si-PYR13FSI system. (a) EELS elemental mapping of Si from (b) TEM micrograph of cycled nSiC/PAN electrode at the 16th delithiation along with EELS elemental mapping and XPS analysis of (c,d) carbon, (e,f) sulfur, (g,h) fluorine, (i,j) lithium and (k,l) oxygen, defining the elemental constitution and favored nucleation sites of the SEI formed.

Electrode morphology and volumetric expansion minimization. While the theoretical and experimental data described provide insight into the formation mechanism and composition of the proposed SEI, we turn to a more comprehensive imaging examination to develop a direct understanding of the morphological effects of the PYR13FSI electrolyte on our Si-based electrode. Consistent with our previous work¹⁹, EELS and TEM reveal a thin, conformal coating of PAN on the nano-Si particles throughout the uncycled composite (Figure 3.6(a,b)). Our previous work verified the mechanical advantages of the cPAN coating by analysing electrode cross-sections at different stages of cycle life, finding an overall electrode volumetric expansion of only 40% after full initial lithiation with an EC/DEC (1M LiPF₆) electrolyte [19]. Through the same treatment of electrode cross-section samples taken before and after (Figure 3.6 (c~d)) initial lithiation in a PYR13FSI (1.2M LiFSI) electrolyte, we find the volumetric expansion of the nSi-cPAN composite to be just 17%. To further investigate this remarkable volume control, TEM micrographs were taken upon initial lithiation (Figure 3.6(e~f)) and after the 16th delithiation (Figure 3.6(g~h)). The TEM images of both the fully lithiated and cycled electrodes show no mechanical deficiencies or morphological changes within the Si particles or the composite structure. Most notably, after the 16th delithiation the Si-PYR13FSI system exhibits no severance of connection between the Si particles and cPAN network with striking preservation of the nano-Si spherical shape, contrasting the relatively poor nano-structural preservation of the same electrode in conventional electrolyte.[19] The impressive structural integrity of the Si-PYR13FSI system is undoubtedly linked to the system's cycling stability, suggesting that the Si-RTIL

interface concurrently promotes favourable electrochemistry and structural resilience.

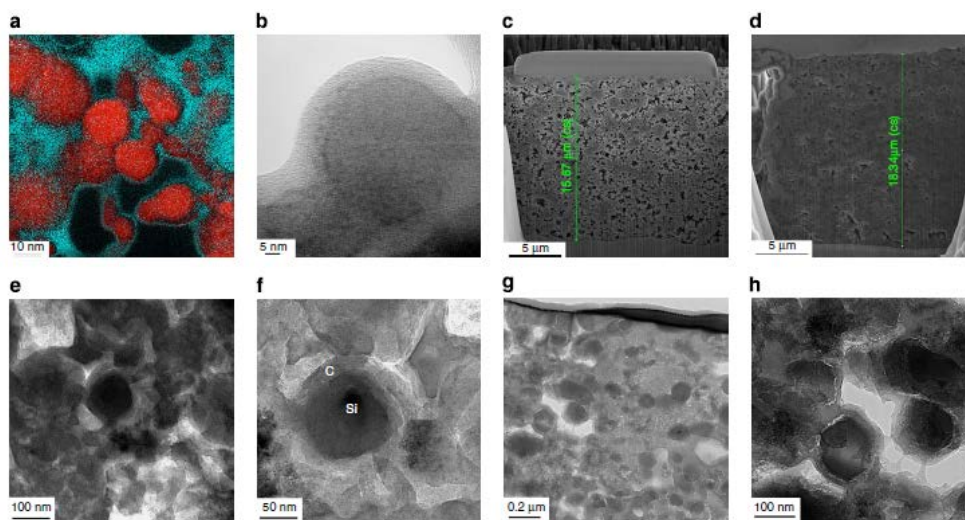


Figure 3.6 Microstructure of nSi-cPAN and morphological effects of PYR13FSI IL on anode. (a) EELS elemental mapping of carbon (cyan) and silicon (red) and (b) TEM micrograph of the pristine nSi-cPAN electrode reveal a thin, conformal coating of PAN on the nano-Si particles throughout the uncycled composite. (c,d) FESEM images of electrode cross-sections before (c) and after (d) initial lithiation showing an electrode volume expansion of only 17%. (e–h) TEM micrographs of fully lithiated (e,f) and 16th delithiated (g,h) nSi-cPAN electrodes showing no mechanical deficiencies or significant morphological changes.

3.4 Conclusion

Cyclized-PAN conformal coatings address several chronic issues that have impeded the commercialization of Si-based electrodes. When designing the coating, we wished to have a material with elastic polymeric properties as well as good conductivity. By cyclizing PAN at temperatures between 300–500 ° C and avoiding carbonization at temperatures > 800°C, we obtain a pyridine-based conjugated polymer that accommodates Si's volumetric expansion during lithiation. Good ionic conductivity of cyclized-PAN coatings is assumed based upon good electrochemical performance at fast cycling rates. And for increased electrode energy density, cyclized-PAN coatings serve as both conductive additive and binder singly. Our approach is attractive for commercialization for two reasons. First, our coating is based upon a commercially available and low-cost polymer precursor. And second, the process described is compatible with commercial electrode slurry manufacturing methods and is adaptable to other anode or cathode materials.

As previously mentioned, the ultimate goal of much electrochemical materials research is to incorporate high-capacity electrodes into a lithium-ion full-cell. Up to this point in our study, we have provided in-depth characterization of the Si-PYR13FSI system and proposed a mechanism for the system's stability through a remarkably robust SEI. The most dependable means of substantiating our claim of a stable SEI is to demonstrate the long-term cycling of a full-cell incorporating the Si-PYR13FSI system. Combining this work and our previous study of the compatibility between PYR13FSI electrolytes and the L333 cathode chemistry, we have built nSi-cPAN/PYR13FSI (1.2M LiFSI)/L333 LIBs capable of maintaining high

energydensities for an exceptionally long cycling life

3.5 Reference

- [1] Daniela Molina Piper , Thomas A. Yersak , Seoung-Bum Son , Seul Cham Kim , Chan Soon Kang , Kyu Hwan Oh , Chunmei Ban , Anne C. Dillon , and Se-Hee Lee, *Adv. Energy Mater.* 2013, 3, 697–702
- [2] D. Larcher , C. Mudalige , A. E. George , V. Porter , M. Gharghoury ,J. R. Dahn , *Solid State Ionics* 1999 , 122 , 71 – 83
- [3] W. Xing , A. M. Wilson , K. Eguchi , G. Zank , J. R. Dahn , *J. Electrochem. Soc.* 1997 , 144 , 2410 – 2416 .
- [4] T. Zhang , L. Fu , J. Gao , L. Yang , Y. Wu , H. Wu , *Pure Appl. Chem.* 2006 , 78 , 1889 – 1896 .
- [5] N. Dimov , S. Kugino , M. Yoshio , *J. Power Sources* 2004 , 136 , 108 – 114 .
- [6] C. S. Wang , G. T. Wu , X. B. Zhang , Z. F. Qi , W. Z. Li , *J. Electrochem. Soc.* 1998 , 145 , 2751 – 2758 .
- [7] Daniela Molina Piper, Tyler Evans, Kevin Leung, Tylan Watkins, Jarred Olson, Seul Cham Kim, Sang Sub Han, Vinay Bhat, Kyu Hwan Oh, Daniel A. Buttry, Se-Hee Lee, *Nature Communications* 6, Article number: 6230
- [8] Hatchard, T. D. & Dahn, J. R. In situ XRD and electrochemical study of the reaction of lithium with amorphous silicon. *J. Electrochem. Soc.* 151, A838–A842 (2004).
- [9] Beaulieu, L. Y., Hatchard, T. D., Bonakdarpour, A., Fleischauer, M. D. & Dahn, J. R. Reaction of Li with alloy thin films studied by in situ AFM. *J. Electrochem. Soc.* 150, A1457–A1464 (2003).
- [10] Chan, C. K., Ruffo, R., Hong, S. S. & Cui, Y. Surface chemistry and

- morphology of the solid electrolyte interphase on silicon nanowire lithium-ion battery anodes. *J. Power Sources* 189, 1132–1140 (2009).
- [11] Balducci, A. et al. Development of safe, green and high performance ionic liquids-based batteries. *J. Power Sources* 196, 9719–9730 (2011).
- [12] S.-B. Son , S. C. Kim , C. S. Kang , T. A. Yersak , Y.-C. Kim , C.-G. Lee ,S.-H. Moon , J. S. Cho , J.-T. Moon , K. H. Oh , S.-H. Lee , *Adv. Energy Mater.* 2012 , 2 , 1226 – 1231
- [13] S.-B. Son , J. E. Trevey , H. Roh , S.-H. Kim , K.-B. Kim , J. S. Cho ,J.-T. Moon , C. M. DeLuca , K. K. Maute , M. L. Dunn , H. N. Han , K. H. Oh , S.-H. Lee , *Adv. Energy Mater.* 2011 , 1199 .
- [14] L. A. Riley , S. V. Atta , A. S. Cavanagh , Y. Yan , S. M. George , P. Liu , A. C. Dillon , S.-H. Lee , *J. Power Sources* 2011 , 196 , 3317 – 3324 .
- [15] A. S. Aricò , P. Bruce , B. Scrosati , J.-M. Tarascon , W. van Schalkwijk , *Nat. Mater.* 2005 , 4 , 366 – 77 .
- [16] M. Armand , J.-M. Tarascon , *Nature* 2008 , 451 , 652 – 7 .
- [17] Markevich, E. et al. In situ FTIR study of the decomposition of N-butyl-N-methylpyrrolidinium bis (trifluoromethanesulfonyl)amide ionic liquid during cathodic polarization of lithium and graphite electrodes. *Electrochim. Acta* 55, 2687–2696 (2010).
- [18] Ji, L. et al. Graphene/Si multilayer structure anodes for advanced half and full lithium-ion cells. *Nano Energy* 1, 164–171 (2011).
- [19] Leung, K. et al. Modeling Electrochemical decomposition of fluoroethylene carbonate on silicon anode surfaces in lithium ion batteries. *J. Electrochem. Soc.*

161, A213–A221 (2014), and references therein.

[20] Budi, A. et al. Study of the initial stage of solid electrolyte interphase formation upon chemical reaction of lithium metal and N-Methyl-N-Propyl pyrrolidiniumbis (fluorosulfonyl) imide. *J. Phys. Chem. C* 116, 19789–19797 (2012).

[21] Philippe, B. et al. Improved performances of nanosilicon electrodes using the salt LiFSI: a photoelectron spectroscopy study. *J. Am. Chem. Soc.* 135, 9829–9842 (2013).

[22] Xiong, S., Xie, K., Blomberg, E., Jacobsson, P. & Matic, A. Analysis of the solid electrolyte interphase formed with an ionic liquid electrolyte for lithium-sulfur batteries. *J. Power Sources* 252, 150–155 (2014).

[23] Molina Piper, D. et al. Conformal coatings of cyclized-PAN for mechanically resilient Si nano-composite anodes. *Adv. Energy Mater.* 3, 697–702 (2013).

Chapter 4. Shape change of Si particle during electrochemical reaction

4.1 Introduction

4.1.1 Introduction of Si/C composite

Recently studies show that Si/C nano-composites is most promising anode materials for Li ion battery. Because consist materials of Si/C composite are inexpensive, non-toxic, stable and have high capacity. Si/C composites are typically prepared by carbonizing precursors [1-3] or by mechanically mixing Si with carbon. [4-5] Si particles embedded in carbon matrix structure is typically used Si/C composites for Si anode. Li battery.

Carbon matrix prevent forming SEI layer on surface of Si particle because Si particles not directly contact with liquid electrolyte. It prevent depletion of liquid electrolyte. Carbon matrix is the buffer for mechanical strains induced by volume expansion of Si [6-7] and enhanced electrical/ionic conductivity. [8-10] In this study, nano Si/C complex composite composed nano Si and amorphous carbon (AC). Amorphous carbon source is pitch hydro carbon which cost is very cheap and easy to recycle. Cycled performance of Si anode influenced by binder types, compared with typical binders (PVDF, PAA, CMC) pitch hydro carbon have reaction at carbon and silicon surfaces interlayer which improves properties of the electrode [11]. We will present fabrication method of Si/AD composite using liquid state pitch carbon. This method is appropriated for carbon coating regardless shape and size of particles.

4.1.2 Forming 3D Si network

Microstructure change of Si/AC composite is observed using electron microscopy with cycle progress. With cycle progress Si diffused in the AC, and forming nano size 3D Si network, the 3D Si network added structural stability and electrical / ionic conductivity of Si / AC composite. [12]

4.2 Experiment procedure

4.2.1 Preperation of Si/C composite

The Si/C nano composite is consisted with silicon nano particles (~200nm), Pitch carbon, KB. The ratio of the silicon nano particles and pitch carbon is 50:50 by wt%. Pitch carbon is dissolved in N-methyl-2-pyrrolidone (NMP) (Sigma–Aldrich) under stirring for 1h, and the Si nanoparticles were dispersed in NMP by ultrasonication for 0.5hr. Dissolved pitch carbon and dispersed Si particles are fully mixed by stirring for 5hrs and the mixture is fully dried at 150°C during 12hrs in order to evaporate solvent(NMP). The prepared mixture is carbonized in sintered tube furnace at 850°C for 5 h under flowing N₂ atmosphere and naturally cooling to room temperature under N₂ atmosphere.

4.2.2 Electrochemical test & Analysis of Microstructure

The electrodes were cycled vs a lithium anode in 2032 coin cell with 1 M LiPF₆ in EC : DEC : FEC 5:70:25 by wt% . Cycle test is performed between 0.01 and 3.0V. Cells were cycled at a rate of 0.1C for 1st cycle, 0.2C for 2nd cycle, and 1C for after 2 cycle.

A FIB (FEI, NOVA200 dual beam system) equipped with an air-lock chamber is used for TEM sample preparation. The air-lock system enables to analyze lithiated electrode without oxidation. The microstructure of Si-Fe structure was investigated by analytical HR-TEM (TECNAI F20 equipped with EELS) operating at 200 keV.

4.3 Results and discussion

4.3.1 Microstructure of Si/C composite with cycle progress

Figure 4.1 is a schematic illustrate of forming mechanism of 3D Si network is in the Si /AC composite. Figure 4.1 (a) is a Si / AC composite of the 1st lithiation state. All nano Si particles react with inserted Li ions which transmitted through AC by electric field. When delithiation state if Si particle is exist near composite surface, transport path of Li ions is short. In this case Li ions can transport easily to surface of composite particle through thin AC layer. However Si particle is exist deeply inside of composite, Li ions hard to transport to surface of composite through thick AC layer. Li ions require faster path to transport for balancing with electric field. For faster transport of Li ions, Si diffuse in AC matrix by ionic migration. Diffused Si forms 3D network structure inside Si/AC composite. Figure 4.1 (b~c). The Si network structure is the fastest Li transport path in Si/AC composite system. After long cycle

Si network is formed whole AC matrix area.

Figure 4.2 is SEM/TEM images of Si/AC composite in order to observation of micro structural change with cycle progress. Si nano particle are embedded AC matrix. Figure 4.2 (a). 1st lithiation state Si particles are expanded but Si network is nor formed yet. This result shows that Li ion transport to Si particle through AC matrix Figure 4.2 (b). Figure 4.2 (c), after few cycles, initial round shape Si particles cannot be observed, and Si whiskers are formed around Si nano particles by diffusion (ionic migration). And Si network is formed between adjacent Si atoms.

Figure 4.2 (d) shows Si network is formed whole Si/AC composite as role of fast Li transport path.

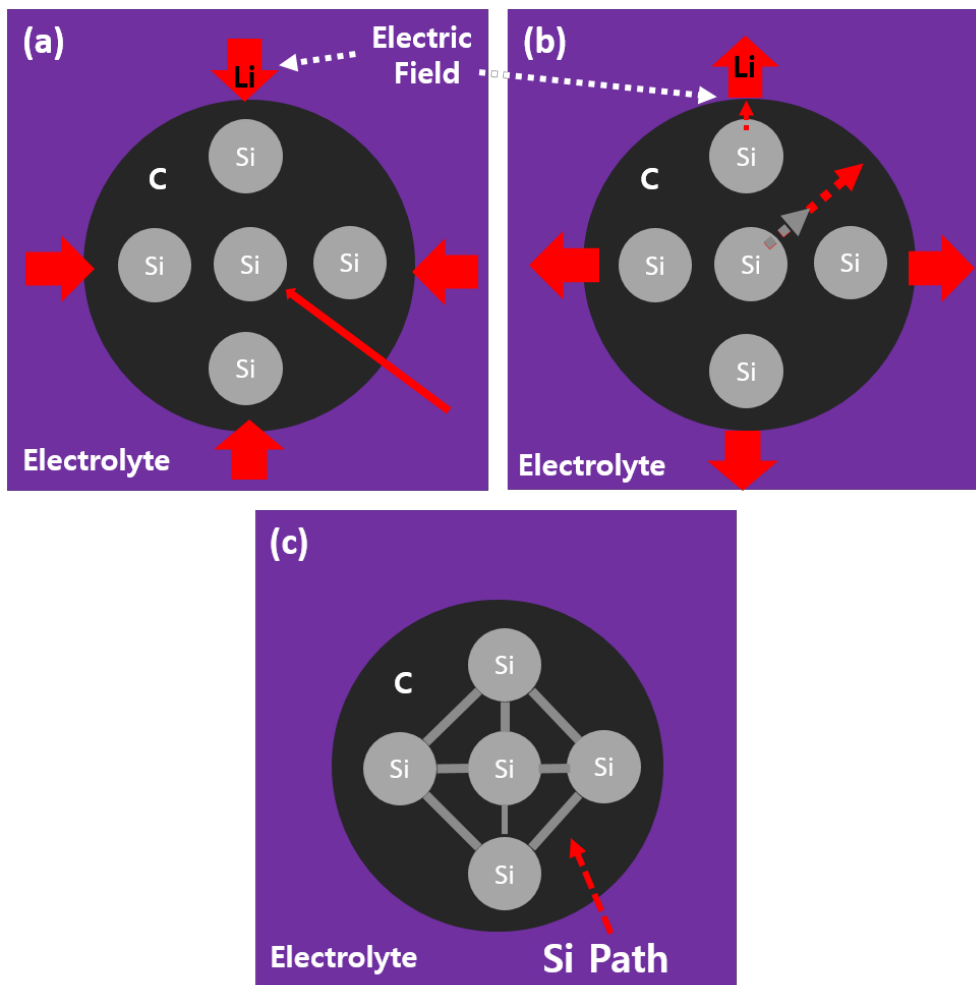


Figure 4.1 Schematics of forming Si 3D network during lithiation and delithiation in Si/AC composite (a) Initial state of Si/AC composite particle. (b) Si diffuse (migration) in C matrix during delithiation. (c) Si nanoparticles tend to fuse to form a network structure to fastest Li ion transfer path. The physical connections between the Si nano particles and the conductive network are preserved during the discharge process

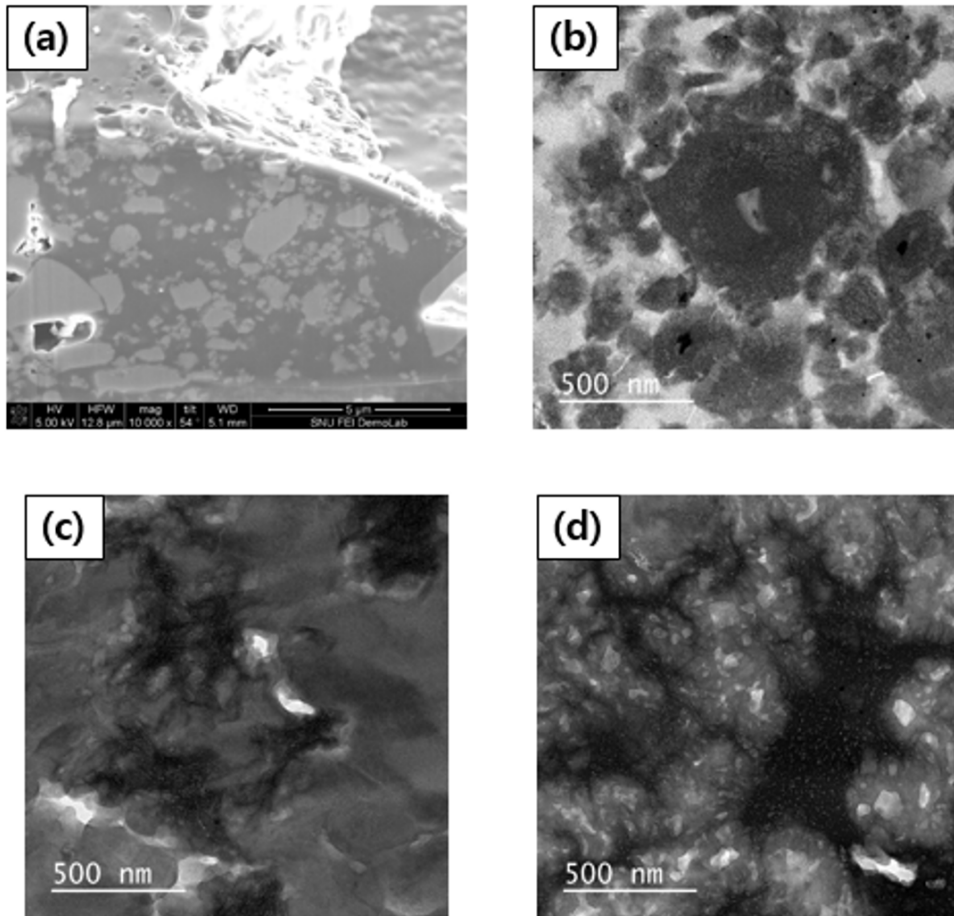


Figure 4.2 Micro-structural change observation of Si nano particle in Si/AC composite during cycle (a) Initial shape of Si/AC composite, (b) 1st lithiated state, (c) after 5 cycles, (d) after 100 cycles

4.3.2 Forming 3D Si network

Figure 4.3 (a) is surface of adjacent Si particles in AC matrix after 100 cycles. Si particles are connected with adjacent another particles. In case of isolated Si particle, Si network cannot be observed. However Si whiskers are formed around Si particles both case of adjacent and isolated Si particle. Figure 4.3 (b). This result prove that Si diffused in AC matrix during cycle. And nano size pores are observed in both Si and AC matrix area. Pores in Si particle area is formed by volume expansion and Si diffusion into AC matrix. However pores in AC matrix area are formed by only Si particle volume expansion. But this pores are closed, liquid electrolyte penetration is not occurred. This result shows Si embedded AC matrix structure is appropriate for enhancing life cycle performance. AC matrix prevents losing conductivity by mechanical fracture and forming SEI layer. Figure 4.3 (c) is high resolution STEM image of 100 cycled Si/AC nano composite. White contrast is primary Si particle, black contrast is AC matrix and gray contrast is Si diffused AC area. After long cycle enough, whole Si/AC composite become gray contrast area that Si and AC are also exist. 3D network structure enhancing life cycle performance because network structure is stable for mechanical and chemical and added ionic conductivity

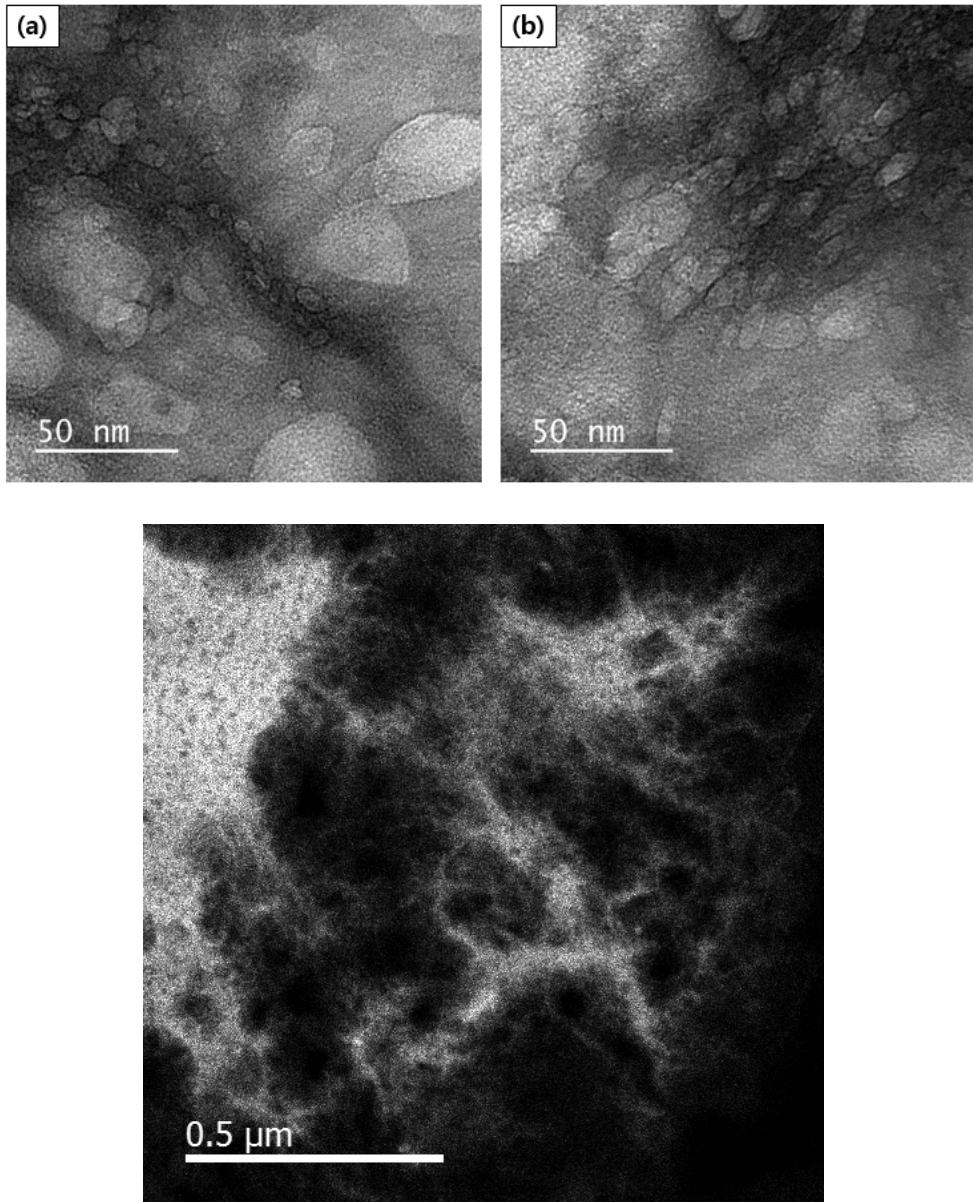


Figure 4.3. (a) After 100 cycle Si particle surface that distance between another particles are close, (b) After 100 cycle surface of isolated Si particles, (c) High-resolution STEM images of 100 cycled Si/AC composite.

4.4 Conclusion

In this study we present Si/AC fabrication using liquid state pitch carbon. This method is appropriated for carbon coating regardless shape and size of particles. In case of Si particle is exist deeply inside of Si/AC composite, Li ions hard to transport to surface through thick AC layer. For faster transport of Li ions, Si diffuse in AC matrix by ionic migration. Diffused Si forms 3D network structure inside Si/AC composite. After long cycle enough, whole particle area will become Si- C mixed area that is stable for mechanical and chemical. We expected that Si-C mixed area has good ionic conductivity for using new solid state electrolyte.

4.5 Reference

- [1] D. Larcher , C. Mudalige , A. E. George , V. Porter , M. Gharghour , J. R. Dahn , Solid State Ionics 1999 , 122 , 71 – 83 .
- [2] W. Xing , A. M. Wilson , K. Eguchi , G. Zank , J. R. Dahn , J. Electrochem. Soc. 1997, 144 , 2410 – 2416 .
- [3] T. Zhang , L. Fu , J. Gao , L. Yang , Y. Wu , H. Wu , Pure Appl. Chem. 2006 , 78 , 1889 – 1896 .
- [4] N. Dimov , S. Kugino , M. Yoshio , J. Power Sources 2004 , 136 , 108 – 114 .
- [5] C. S. Wang , G. T. Wu , X. B. Zhang , Z. F. Qi , W. Z. Li , J. Electrochem. Soc. 1998 , 145 , 2751 – 2758 .
- [6] Y.-S. Hu, R. Demir-Cakan, M.-M. Titirici, J.-O. Muller, R. Schlogl, M. Antonietti, J. Maier, Superior storage performance of a Si@SiO_x/C nanocomposite as anode material for lithium-ion batteries, *Angewandte Chemie International Edition* 47 (2008) 1645.
- [7] Yun-Xiao Wang, Shu-Lei Chou*, Jung Ho Kim, Hua-Kun Liu, Shi-Xue Dou, *Electrochimica Acta* 93 (2013) 213– 221
- [8] J.R. Szczech, S. Jin, Nanostructured silicon for high capacity lithium battery anodes, *Energy & environmental Science* 4 (2011) 56.
- [9] S.H. Ng, J. Wang, D. Wexler, K. Konstantinov, Z.P. Guo, H.K. Liu, Highly reversible lithium storage in spheroidal carbon-coated silicon nanocomposites as anodes for lithium-ion batteries, *Angewandte Chemie International Edition* 45 (2006) 6896.
- [10] W. Wang, P.N. Kumta, Nanostructured hybrid silicon/carbon nanotube

heterostructures: reversible high-capacity lithium-ion anodes, ACS Nano 4 (2010) 2233.

[11] S. Komaba, K. Shimomura, N. Yabuuchi, T. Ozeki, H. Yui, K. Konno, Study on polymer binders for high-capacity SiO negative electrode of Li-ion batteries, Journal of Physical Chemistry C 115 (27) (2011) 13487.

[22] Mingyan Wu, Julian E. C. Sabisch, Xiangyun Song, Andrew M. Minor, Vincent S. Battaglia, Gao Liu Nano Lett. 2013, 13, 5397–5402

(Part 2) Micro-structural change observation of variety

types of cathode materials during cycle

Chapter 5. Structural change observation of reversible FeS₂

cathode in solid state electrolyte system

5.1 Introduction

5.1.1 Pyrite for cathode material

The FeS₂ four electron conversion reaction exhibits a theoretical capacity of 894 mAh/g with two discharge plateaus at roughly 2.1 and 1.5 V versus Li⁺/Li. Research continued to examine the utilization of FeS₂ as an active material at ambient to moderate temperatures. FeS₂ has been successfully commercialized in high energy density only primary cells. [2] Unfortunately, the FeS₂ conversion chemistry is irreversible in cells with a variety of polymer or liquid electrolytes at temperatures <135°C. [3–7]

5.1.2 Solid state electrolyte battery

Solid state electrolyte, it is best to improve the ionic and electronic conductivity of the active material and prevent separation of Sulfur. Solid state electrolyte battery is a safe alternative to conventional Li-ion batteries because sulfide based glass-ceramic electrolytes are pure ionic conductors, non-volatile, non-flammable, and stable versus liquid electrolyte battery. In this study, we take advantage of a sulfide based glass electrolyte to address the problems commonly associated with FeS₂'s

rapid capacity fade at lower temperatures. Along the way, we identify orthorhombic-FeS₂ (marcasite) as a charge product and use this discovery to come to a better understanding of the FeS₂ conversion chemistry.[1]

5.2 Experiment Procedure

5.2.1 Synthesis of Pyrite

FeS₂ was synthesized solvothermally utilizing a reaction scheme adapted from Wang et al. [8] Synthetic FeS₂ was characterized by Cu-K α x-ray diffraction (XRD) measurement, field emission scanning electron microscopy (FESEM, JEOL JSM-7401F), and Raman spectroscopy (Jasco NRS-3100). Cell fabrication and cell testing for this study was carried out under an inert Argon gas environment. Solid electrolytes were prepared by planetary ball milling (Across International).

5.2.2 Solid state electrolyte battery

The solid electrolyte is an amorphous 77.5Li₂S:22.5P₂S₅ binary glass. [9] The glass electrolyte is prepared by milling an appropriate ratio of Li₂S (Aldrich, 99.999%, reagent grade) and P₂S₅ (Aldrich, 99%) with a planetary ball mill (Across International PQ-N2). 2g net weight of material is milled in a 500mL stainless steel vial (Across International) with \times 2 16mm diameter and \times 20 10 mm diameter stainless steel balls at 500 rpm for 20 hours. The composite positive electrode is a 10:20:2 weight ratio mixture of synthetic FeS₂, 77.5Li₂S:22.5P₂S₅, and carbon black (Timcal Super C65) respectively. The composite positive electrode is mixed using an agate mortar and pestle. Stabilized lithium metal powder (SLMP) is used as the

negative electrode (FMC Lithium Corp.). The construction and testing of solid state batteries utilizes a titanium-polyaryletheretherketone (PEEK) test cell die. [10] 200 mg of solid electrolyte powder is pressed at 1 metric ton in the PEEK cell die. 5 mg of composite positive electrode and the stabilized lithium metal powder are then attached to opposite sides of the solid electrolyte pellet by pressing at 5 metric tons. The solid state sulfur cell used in dQ/dV analysis was fabricated using a process adapted from Nagao et al. [11] Liquid cells were fabricated by spreading an electrode slurry with a 6:2:2 weight ratio of synthetic FeS_2 , polyvinylfluorine (PVDF) binder (Alfa Aesar) and acetylene black (Alfa-Aesar, 50% compressed) respectively. FeS_2 electrodes were then assembled into coin cells with a lithium foil negative electrode (Alfa-Aesar, 0.25 mm thick) and 1MLiPF₄ electrolyte.

5.2.3 Electrochemical test & Analysis of Microstructure

Cells were cycled galvanostatically using an Arbin BT2000 battery tester at room temperature (30°C) and elevated temperature (60°C). Stated C-rates are based upon FeS_2 's theoretical capacity of 894 mAh/g. For the detailed observation of lithiated FeS_2 composite electrodes, high resolution transmission electron microscopy (TEM, JEOL 3000F) samples are prepared using our focused ion beam (FIB, FEI NOVA200 dual beam system) machine equipped with air-lock system. The air-lock system enables our composite electrode to remain in a vacuum state while samples are loaded from the glove box to the FIB chamber. The Gatan Digital Micrograph fast Fourier transform (FFT) software was used in the analysis to determine the crystalline phases present in the fully charged FeS_2 electrode.

5.3 Results and discussion

5.3.1 Electrochemical properties of Pyrite

The morphology of synthetically prepared FeS₂ was characterized with field emission scanning electron microscopy (FESEM) and the crystalline configuration by x-ray diffraction (XRD). Cu-K α x-ray diffraction analysis of synthetically prepared FeS₂ exhibits diffraction peaks that match well with the cubic-FeS₂ phase (Figure 5.1 (a)). FESEM images reveal cubic FeS₂ particles with $\sim 2.5\mu\text{m}$ wide faces (Figure 5.1 (b)). Synthetic FeS₂ was tested in both a solid-state and liquid cell configuration. To achieve full utilization of FeS₂, the cells are cycled between 1.0V and 3.0V vs. Li+/Li. The results of cycling at ambient temperature (30°C) and moderate temperature (60°C) are presented in **Figure 5.2** Both solid-state cells are observed to have a stable capacity and a high degree of FeS₂ utilization. The gradual increase in capacity with cycling is observed and attributed to better FeS₂ utilization and not utilization of the Li₂S solid electrolyte component. By the 20th cycle, the cell tested at 30°C exhibits a discharge capacity of nearly 750 mAh/g while the cell tested at 60°C exhibits a theoretical discharge capacity of 894 mAh/g. It is likely that the temperature dependence of the solid electrolyte's ionic conductivity contributes to the full FeS₂ utilization at 60°C. Improved reaction kinetics of the Fe⁰ + Li₂S/FeS₂ conversion reaction may contribute to better FeS₂ utilization as well. The liquid cells' discharge capacities rapidly fade upon cycling. By the 20th cycle, the liquid cell tested at 30°C exhibits a discharge capacity of only 190mAh/g while the cell tested at 60°C exhibits no discharge capacity.

Decomposition processes are accelerated at 60°C leading to such a fast rate of capacity fade that negligible capacity is observed after the second cycle. On the other hand, we have just shown that cycling a solid state FeS₂ cell at 60°C improves its performance. This result is important when it is considered that most traction battery packs are designed to operate at temperatures near 60°C. The superior performance of solid-state batteries at higher temperatures may reduce the need for extensive thermal management systems.

In agreement with the literature, we observe that a cell's initial discharge profile has one plateau when the cell is cycled at 30°C (Figure 5.2 (a,c)) and two plateaus when the cell is cycled at 60 ° C (Figure 5.2 (b,d)). The shoulder at 1.3 V in the ambient temperature liquid cell's initial discharge profile (Figure 5.2 (c)) is attributed to a new phase related to the reaction of Fe⁰ with organic liquid electrolyte. [11]

The initial discharge profile for each FeS₂ cell is different from subsequent discharge profiles. We will propose that the change in discharge profiles is due to the formation of nano-crystalline orthorhombic-FeS₂ particles at full charge.

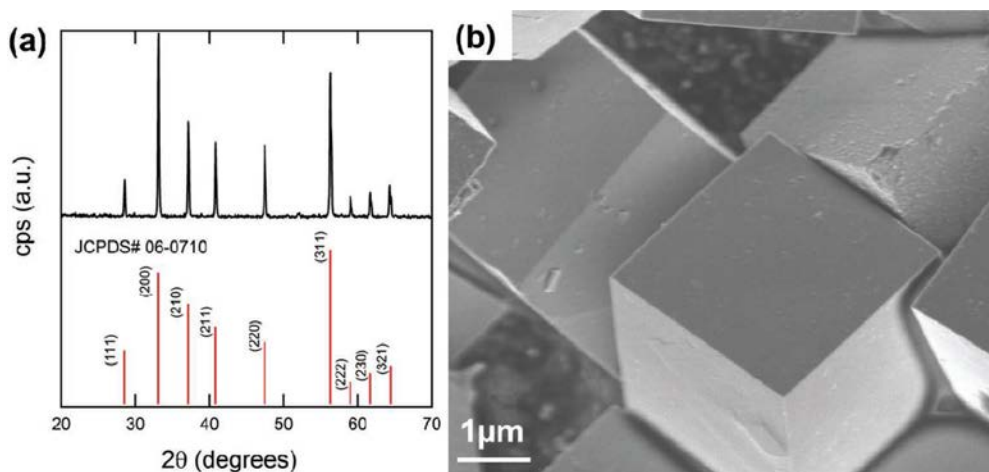


Figure 5.1 (a) Indexed x-ray diffraction of synthetic cubic-FeS₂. (b) FESEM image of synthetic cubic-FeS₂ that confirms cubic structure with 2–3 μm cubes.

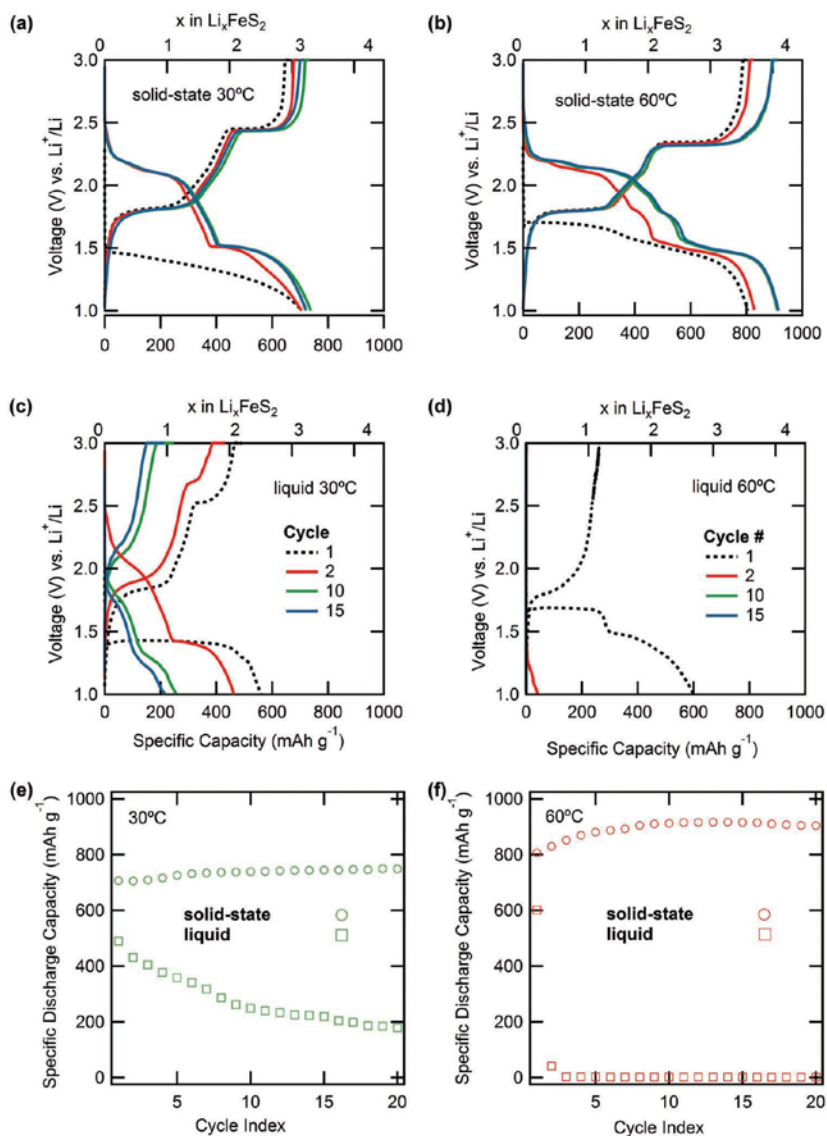


Figure 5.2 Comparison of synthetic cubic-FeS₂ cycled at 30 °C and 60 °C in conventional liquid coin cells and in solid-state cells: a) solid-state cell at 30 °C, b) solid-state cell at 60 °C, c) liquid coin cell at 30 °C, d) liquid coin cell at 60 °C, e) capacity retention comparison of cells cycled at 30 °C, and f) capacity retention comparison of cells cycled at 60 °C. All cells except for the 30 °C solid-state cell were cycled at a current of 144 μA which corresponds to a rate

5.3.2 Microstructural change of Pyrite

We have found that orthorhombic-FeS₂ is produced electrochemically from discharge products along with elemental sulfur at 30–60 ° C. This conclusion is based upon the results TEM observation (Figure 5.4). Literature generally agrees that the formation of FeS_y and S instead of cubic-FeS₂ upon full charge explains why subsequent discharge profiles differ from the initial discharge profile.

When a cubic-FeS₂ solid-state cell is allowed up to 144hours to establish equilibrium during its initial discharge at 60°C, the open circuit voltage (OCV) of the cell approaches the voltage of a subsequent discharge at the appropriate reaction coordinate, x . The results of coulometric titration are compared to 1st, 2nd , and 10th discharges of the solid-state cell cycled at 60°C (Figure 5.3 (a)). This result indicates that the difference between the initial discharge profile and subsequent discharge profiles can be explained by kinetics and not by an entirely different reaction pathway. Particle morphology and a more open regenerated crystal structure would result in faster reaction kinetics. As Fong et al. have already indicated, the initial reduction of pyrite is limited both by the rate and the temperature of the reaction. [4]

The slow diffusion of Li + into 3 μ m pyrite cubes severely limits the reduction reaction kinetics. If electrochemically produced FeS₂ particles are nano-crystalline, the greatly increased interfacial surface area will facilitate a fast reaction rate despite poor Li + diffusivity. The diffusivity of Li + may also be improved by regenerating a phase other than cubic-FeS₂. For example, orthorhombic-FeS₂ has a more open structure than cubic-FeS₂. The formation of orthorhombic-FeS₂ instead of cubic-FeS₂ may result in faster Li + diffusion, thus further increasing the reduction reaction

kinetics. High resolution transmission electron microscopy (HRTEM) supports these claims with direct observation of orthorhombic-FeS₂ nanoparticles upon charge. We recovered electrode material from the solid-state cell cycled at 60°C upon completion of its 20th charge (Figure 5.2 (b)). This cell exhibits full utilization of FeS₂ so it is unlikely that a significant mass of electrochemically inactive synthetic cubic-FeS₂ remains in the cell by the 20th charge.

Figure 5.4 (a) shows a bright field (BF) TEM image of the 20th cycled charged FeS₂ solid-state electrode. This image depicts nano-crystalline domains (darker) of 100–200 nm in diameter encased by an amorphous material (lighter). Fast Fourier transform (FFT) analyses of HR-TEM images matches well with orthorhombic-FeS₂ along the $[-110]$ zone axis (Figure 5.4(b)). The average Fe-Fe interatomic distance ($d_{\text{Fe-Fe}}$) increases for decreasing x over the range $4 \leq x < 2$. Delithiation of the first two lithium ions corresponds to the oxidation of Fe⁰ to Fe²⁺. It is possible that the observed FeS₂ nanoclusters could crystallize into orthorhombic-FeS₂ rather than cubic-FeS₂ because of the former's lower density.

To gain a better understanding of the amorphous regions that we observed with HR-TEM, we examined the differential capacity of the solid-state cell cycled at 30°C (Figure 5.3(b)). The green peaks in Figure 5.3 (b) correspond to the oxidation of Li₂S and the reduction of S in a solid-state S/Li cell. [11] The purple peaks correspond to reaction plateaus observed during the 1st, 2nd and 9th discharges of our solid-state FeS₂ cell cycled at 30°C. When the solid-state FeS₂ cell is charged we observe no peaks corresponding to the oxidation of Li₂S. An absent Li₂S oxidation peak indicates that the Li₂S component in the solid electrolyte is not electrochemically utilized in

the cell. Instead, elemental sulfur is produced only by the disproportionation of $\text{Li}_{2-x}\text{FeS}_2$ at approximately 2.4 V. However, upon discharge we observe a peak at 2.2 V which corresponds to the direct reduction of sulfur to Li_2S . The same is true for the solid-state cell cycled at 60°C. The solid-state cell cycled at 30°C exhibited a discharge capacity of 737 mAh/g upon its 9th discharge. If the peaks at 2.1 and 2.2 V correspond to the reaction of charge products with the equivalent of 2 electrons, then it is expected that integrating the dQ/dV curve between 1.6 and 2.5 V will yield a capacity of 368 mAh/g. When these two peaks are deconvoluted by fitting each with a Voigt profile, then the calculated total area gives a capacity of 342.2 mAh/g (Figure 3.1.3 (c)). This value matches well with the expected capacity of 368 mAh/g. The peak at 2.2 V has an area of 57.14 mAh/g while the peak at 2.1 V has an area of 285.79 mAh/g.

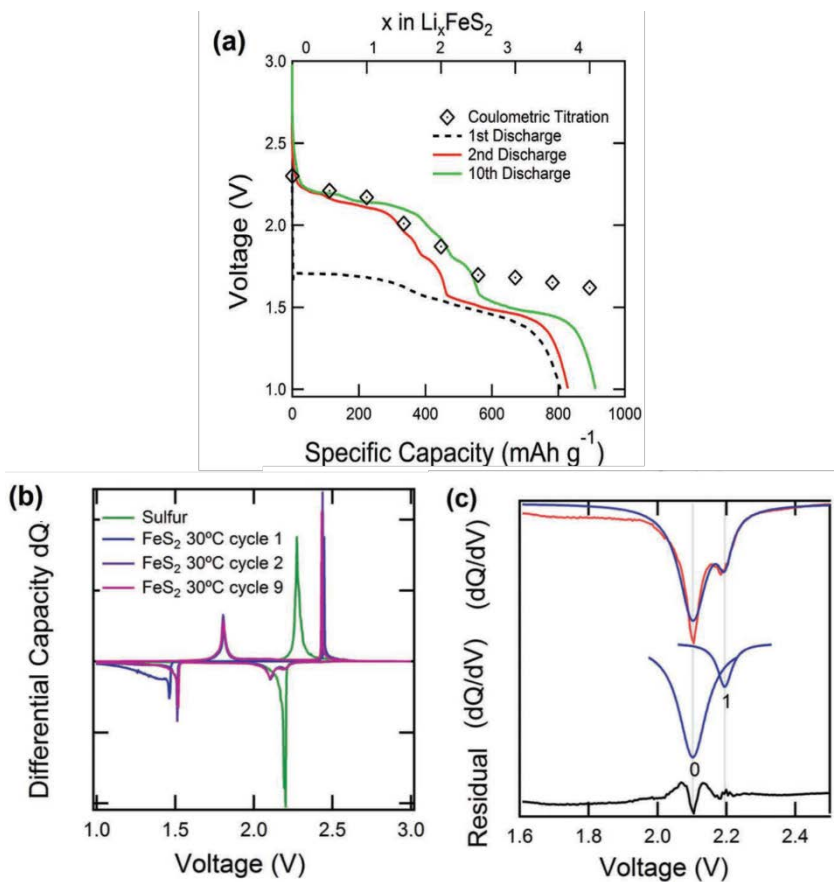


Figure 5.3 (a) Coulometric titration results for the solid-state cell titrated at 60 ° C compared with the 1 st , 2 nd , and 10 th discharge profiles for the solid-state cell cycled at 60 ° C (Figure 2 b). (b) dQ/dV of solid-state cell cycled at 30 ° C. (c) Deconvolution of the dQ/dV peaks at 2.1 and 2.2V with fitted peaks and residual.

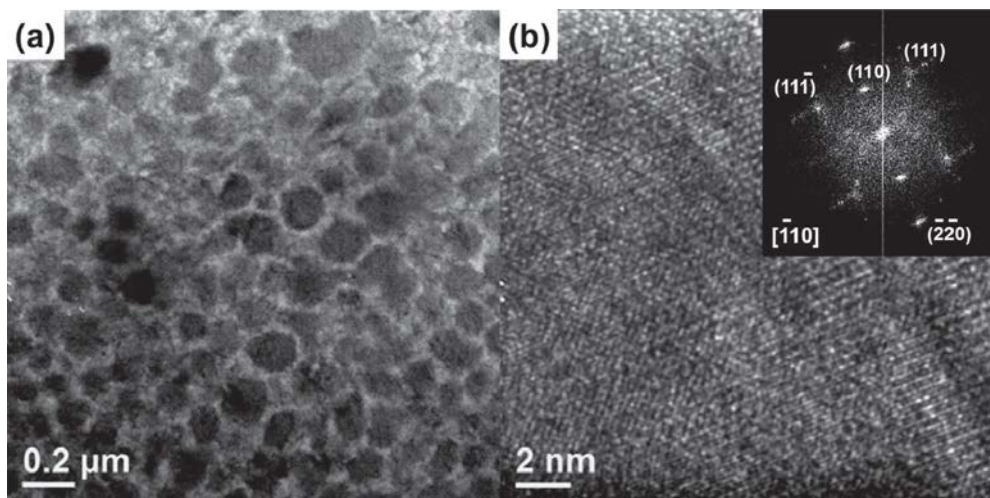


Figure 5.4 Electrode material from the solid-state cell cycled at 60 ° C (Figure 2 b) was recovered after the 20th charge for TEM analysis. a) Bright field TEM image of the 20th cycle sample. Darker areas correspond to nano-crystalline orthorhombic-FeS₂ while the lighter areas correspond to a amorphous region composed of FeS_y and elemental sulfur. b) HR-TEM of the 20th cycle sample. FFT analysis matches with orthorhombic-FeS₂ along the [- 110] zone axis.

5.4 Conclusion

Our assertion that charge products are nano-crystalline orthorhombic-FeS₂ particles encased in non-stoichiometric FeS_y and sulfur is consistent with prior research and our observations. Coulometric titration indicates that the initial discharge is kinetically limited and that subsequent discharges largely follow the same reaction path. Nano-crystalline orthorhombic-FeS₂ particles enable faster reduction kinetics such that subsequent discharges are not kinetically limited and can occur at a higher potential. From dQ/dV analysis, we observe evidence of sulfur reduction at 2.2 V but not Li₂S oxidation. Evidence of direct sulfur reduction supports our conclusion that the observed amorphous region contains elemental sulfur. The amorphous region also contains FeS_y because the absence of the Li₂S oxidation peak indicates that elemental sulfur is produced by the disproportionation of Li_{2-x}FeS₂ during charging. [4] And finally, orthorhombic-FeS₂ exhibits very weak temperature independent paramagnetism. [12] For this reason, it is likely that ⁵⁷Fe Mössbauer spectroscopy used in previous studies was not capable of distinguishing orthorhombic-FeS₂ from other magnetic phases like FeS_{8/7} and unreacted cubic-FeS₂. To this end, we have demonstrated the reversible, ambient to moderate temperature cycling of FeS₂ and proposed a new charge product for a better understanding of the FeS₂ discharge process.

5.5 Reference

- [1] Thomas A. Yersak, H. Alex Macpherson, Seul Cham Kim, Viet-Duc Le, Chan Soon Kang, Seoung-Bum Son , Yong-Hyun Kim , James E. Trevey , Kyu Hwan Oh , Conrad Stoldt , and Se-Hee Lee, *Adv. Energy Mater.* 2013, 3, 120–127
- [2] Y. Shao-Horn , S. Osmialowski , Q. C. Horn , *J. Electrochem. Soc.* **2002** , 149 , A1499 .
- [3] J. Cabana , L. Monconduit , D. Larcher , M. R. Palacín , *Adv. Mater.* **2010** , 22 , E170; L. A. Montoro , J. M. Rosolen , *Solid State Ionics* **2003** , 159 , 233 ; J. W. Choi , G. Cheruvally , H. J. Ahn , K. W. Kim , J. H. Ahn , *J. Power Sources* **2006** , 163 , 158 .
- [4] R. Fong , J. R. Dahn , C. H. W. Jones , *J. Electrochem. Soc.* **1989** , 136 , 3206 .
- [5] E. Strauss , D. Golodnitsky , K. Freedman , A. Milner , E. Peled , *J. Power Sources* **2003** , 115 , 323 ; E. Peled , D. Golodnitsky , E. Strauss , J. Lang , Y. Lavi , *Electrochim. Acta* **1998** , 43 , 1593 ; G. Ardel , D. Golodnitsky , K. Freedman , E. Peled , G. B. Appetecchi , P. Romagnoli , B. Scrosati , *J. Power Sources* **2002** , 110 , 152 .
- [6] J. Barker , E. Kendrick , *J. Power Sources* **2011** , 196 , 6960 .
- [7] D. Golodnitsky , E. Peled , *Electrochim. Acta* **1999** , 45 , 335 .
- [8] D.-W. Wang , Q.-H. Wang , T.-M. Wang , *Cryst. Eng. Comm.* 2010 , 12 , 755 .
- [9] J. Trevey , J. S. Jang , Y. S. Jung , C. R. Stoldt , S.-H. Lee , *Electrochem. Commun.* 2009 , 11 , 1830 .
- [10] T. A. Yersak , J. Trevey , E. S.-H. Lee , *J. Power Sources* 2011 , 196 , 9830 .

[11] M. Nagao , A. Hayashi , M. Tatsumisago , *Electrochim. Acta* **2011** , 56 ,6055 .

[12] R. Garg, V. K. Garg , Y. Nakamura , *Hyperfi ne Interact.* 1991 , 67 , 447 .

Chapter 6. Improvement life performance of Ni-Mn-Co intercalation cathode materials by Al₂O₃ ALD coating for preventing micro structural change

6.1 Introduction

6.1.1 LiNi_{1/3}Mn_{1/3}Co_{1/3}O₂ (NMC) cathodes

LiNi_{1/3}Mn_{1/3}Co_{1/3}O₂ (NMC) cathodes have been the subject of extensive studies as high-energy cathode materials for rechargeable Li-ion batteries because of their high specific capacity and relatively low cost [1-6]. However, practical use of NMC cathodes particularly in plug-in hybrid electric vehicles (PHEVs) and electric vehicles (EVs), have been delayed because of their limited power performance (rate capability) and drastic degradation in their capacity and cycle-life at high operation temperatures (45°C~60°C) and voltages (>4.3 V) [7-9]. One possible way to endow NMC based cathodes with quality power performance is to blend them with a compensating cathode material, such as LiMn₂O₄ spinel (LMO), which has better high rate performance. This blending method enables use of NMC:LMO hybrid cathodes for less expensive commercialized electric vehicles (e.g. GM-Volt) [10] with improved power density and safety. However, emerging concerns about LMO's lower energy density compared to NMC and capacity fade due to metallic dissolution at elevated temperatures [11-12] has led to a need for researchers to develop new materials technology.

6.1.2 Atomic Layer Deposition

Recently, we demonstrated atomic layer deposition (ALD) as an advanced coating method for a variety of Li-ion battery electrodes. [13-16] ALD utilizes sequential and self-limiting surface reactions that enable tailored conformal coatings with Å-level thickness control [17]. An additional advantage of ALD is that it may be employed for both powders and also directly on fully fabricated electrodes. Unfortunately fundamental mechanism for the performance improvement of Li-ion battery via ALD surface modification has not been elucidated yet. We present, for the first time, true fundamental mechanistic understanding of atomic-scale surface modification based on significant characterization including electrochemical impedance spectroscopy (EIS), transmission electron microscopy (TEM), and Synchrotron x-ray diffraction (SR-XRD).

6.2 Experiment procedure

6.2.1 Al₂O₃ ALD on NMC particle

Al₂O₃ ALD films were grown directly on NMC powders (Johnson Controls Inc.) using a rotary reactor. For the Al₂O₃ ALD, trimethylaluminum (TMA 97%) and HPLC (high performance liquid chromatography) grade H₂O was purchased from Sigma Aldrich. The typical growth rate for the chemistry is 0.11 nm/cycle. Due to a small amount of H₂O residue in the reactor after each cycle a slightly increased growth rate of 0.13 nm/cycle. was achieved. The Al₂O₃ ALD reaction sequence was: i) TMA dose to 1.0 Torr; ii) hold pressure static for 60 s; iii) evacuation of reaction

products and excess TMA; iv) 5N₂ purges; v) H₂O dose to 1.0 Torr; vi) hold pressure static for 60 s; vii) evacuation of reaction products and excess H₂O; viii) and 5N₂ purges. Each N₂ purge consisted of dosing N₂ to 20Torr, holding pressure static for 60 s, and then pumping the reaction chamber down for 60 s. This sequence constitutes one cycle of Al₂O₃ ALD. All ALD cycles were conducted at 180°C. The Al₂O₃-coated NMC powders with 4 cycles of ALD (NMC/4ALD) were followed by heat treatment at 300°C in Air for 12h.

6.2.2 Electrochemical test & Analysis of Microstructure

Composite electrodes were comprised of the prepared powders (NMC Bare, NMC/4ALD and NMC:LMO = 1:1), carbon black and polyvinylidene fluoride (90:5:5) in N-methylpyrrolidinon. The composite was coated onto high grade Al foil current collector and roll-pressed after dried in air at 80°C for 1 h. The electrodes were dried in a vacuum oven at 120°C for 12 h before use. The separators were thick porous silica and the electrolyte was 1M LiPF₆ in EC:DEC (1:1 volume ratio). Cell tests were done with a 2032 coin-type cell using Li metal as the anode. All assembled cells were allowed to rest for at least 10h at room temperature prior to electrochemical tests. For cycle-life tests, the cells were cycled between 3.0 and 4.5 V at low rate of C/4 (40mA/g) during the initial two cycles. The cells were charged and discharged between 3.0 and 4.5 V by applying a constant 1 C current (160 mA/g) and 30 min voltage hold at 4.5 V. The cycle-life tests at 55°C were performed at both 3.0~4.3 V and 3.0~4.5V with the same constant current (1 C-rate, 160 mA/g).

Microstructure characterizations Cross-sectional samples were prepared from the 100cycled (1 C-rate, 3.0~4.5 V) fully charged NMC Bare and NMC/4ALD electrodes using a dual-beam focused ion beam (FEI,Nova Nanolab 200). In order to analyze crystal structure of the both electrodes, TEM samples were prepared from the crossectioned electrode particles using a focused ion beam lift-out technique with a manipulating probe (Omniprobe 100.7). Crystal structure information from the inner area and outer area of each electrode TEM sample was determined by selected area electron diffraction (SAED) patterns using a high-resolution TEM (JEOL, JEM 3000F).

XRD data was collected at beamline X14A ($\lambda = 0.07788\text{nm}$) at the National Synchrotron Light Source at Brookhaven National Laboratory (NSLS-BNL). The data were collected with glass capillaries (0.5 mm diameter) in transmission mode using a silicon strip detector scanning from 6 to 60° two-theta. To prepare ex-situ samples, cells are disassembled in Argon-filled glove box and electrodes are washed and cratched off the current collector. They are sealed in glass capillaries in the glove box to avoid air exposure. For easy comparison with other researchers' results, all two theta values in the XRD data are converted to the two-theta value of Cu Ka wavelength ($\lambda = 0.015418\text{nm}$). Rietveld refinements were performed on the collected data using GSAS-EXPGUI software.

6.3 Results and discussion

6.3.1 Electrochemical properties of ALD coated NMC

Uncoated NMC (NMC Bare), 1:1 mixture of NMC:LMO (NMC:LMO), and NMC/4ALD electrodes were tested in CR2032 coin cells with Li-metal foil anode. Figure 6.1 shows a cycling performance of the three battery cells at room temperature (25°C) between 3.0 and 4.5 V at 1 C-rate after the two formation cycles at C/4-rate. When charged/discharged at 1 C-rate (160 mA/g) at the initial stage, the NMC Bare cell delivers a discharge capacity of approximately 171 mAh/g while the NMC/4ALD cell shows a slightly lower capacity of 166 mAh/g. The initial lower capacity of the NMC/4ALD was expected due to the additional Al₂O₃ coating layer on the surface of the cathode particles. The Al₂O₃ layer may affect ionic mobility through the coating layer although the thickness of the layer is ultra-thin (<1 nm). During the 1 C-rate cycling from 3rd to 100th cycle, the NMC/4ALD cell exhibits cycling performance with the highest capacity retention, 96% of the initial capacity, which surpasses the NMC Bare (91%) and the NMC:LMO (95%) cells. It is notable that the discharge capacity of the NMC/4ALD starts to overtake the NMC Bare at around the 50th cycle. The NMC:LMO electrode cell, which is currently being used for Li-ion batteries in commercial PHEVs, exhibits a moderate initial capacity (127 mAh/g) and cyclability (95%) as expected. The NMC/4ALD, however, still appears to be more attractive in terms of the Li-ion batteries' specific energy density. The charge/discharge voltage profiles of the NMC Bare, NMC:LMO and NMC/4ALD cells at 3rd and 100th cycle with 1 C-rate are shown in Figure 3.2.2 (a~c) displaying stable voltage potentials and capacities corresponding to the passable capacity retentions after the continuous 1 C-rate cycling.

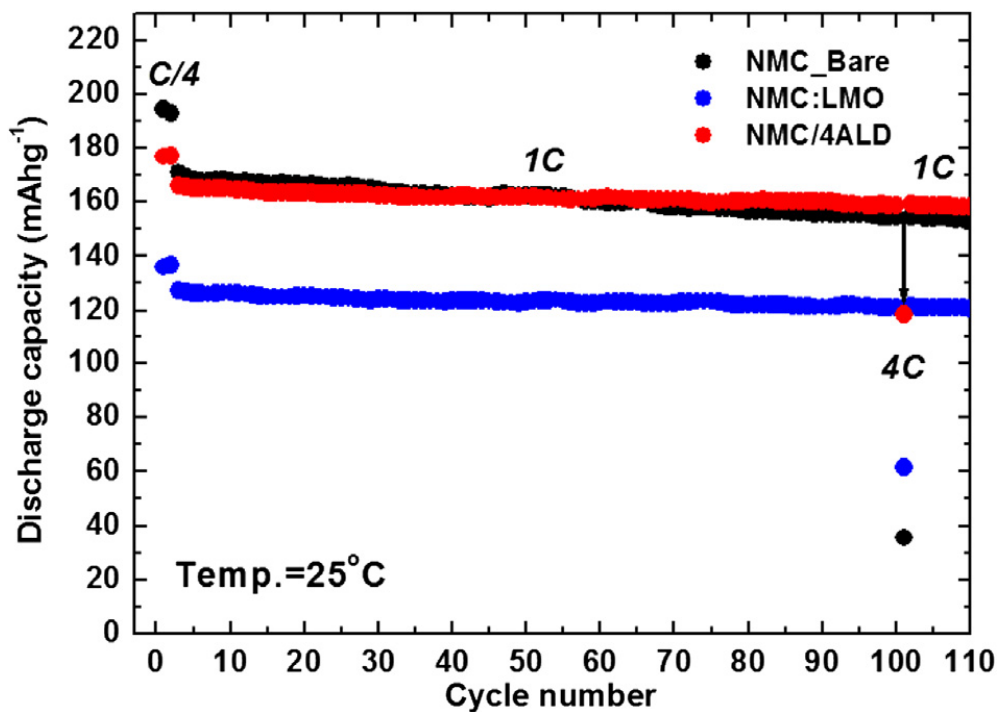


Figure 6.1. Cycling performance of half cells using uncoated-NMC (NMC Bare), uncoated-NMC:LMO (NMC:LMO, 1:1 mixture) and Al₂O₃ 4ALD coated-NMC (NMC/4ALD) cathodes cycled between 3.0 and 4.5 V versus Li⁺/Li at 25 °C at 1 C-rate (160 mA g⁻¹ for NMC Bare and NMC/ALD and 130 mA g⁻¹ for NMC:LMO) following after the first two formation cycles at C/4-rate (40 mA g⁻¹ for NMC Bare and NMC/ALD and 32.5 mA g⁻¹ for NMC:LMO). Discharge capacities at 4C-rate (640 mA g⁻¹ for NMC Bare and NMC/ALD and 520 mA g⁻¹ for NMC:LMO) after 100 cycles are shown at the 101st cycle

Surprisingly, the most striking result is observed at 4 C-rate cycling at the 101st cycle right after the consecutive 100 cycles with 1 C-rate as seen in Figure 6.1. Although the pristine NMC Bare and the NMC/4ALD cells have shown a similar discharge capacity (~ 160 mAh/g) at 1 C-rate cycling, there is a huge difference in the specific capacity ($d_{\text{cap}} = 83$ mAh/g) between the two cells recorded at four times higher current density (4 C-rate, 640 mA/g). In Figure 6.2 (d-f), the voltage profiles of NMC/4ALD show a significantly reduced overpotential compared to the NMC Bare between the 1 C-rate and the 4 C-rate cycling. This leads to a higher capacity of 118 mAh/g for NMC/4ALD in contrast to a diminished capacity of 35 mAh/g for NMC Bare. The NMC/4ALD cell exhibits an excellent high-rate capability despite its high active material content (90% of the composite electrode). The NMC:LMO cell (Figure 6.2(e)) also shows a reasonable rate capability with a discharge capacity of mAh/g, mainly due to the superior rate capability of the LMO, but this is still much less than that of the NMC/4ALD. The outstanding cycle-life and high-rate performance of the NMC/4ALD implies that the ALD Al_2O_3 coating enhances the electrochemical properties of the pristine NMC through nano-scale surface modification, the positive effects of which are maintained over the longterm cycling even at high current rate.

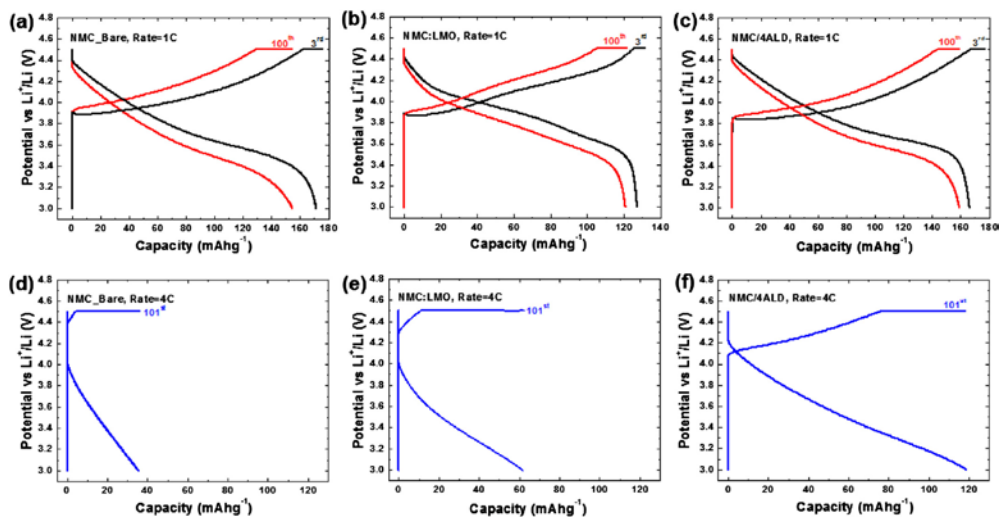


Figure 6.2 (a~c) Comparison of 3rd and 100th charge-discharge voltage profiles (3.0e4.5 V) at 1 C-rate, (d~f) charge-discharge voltage profiles at 4 C-rate after continuous 100 cycles at 1 C-rate of NMC Bare, NMC:LMO and NMC/4ALD half cells. Voltage hold is applied at 4.5 V for 0.5 h after each charge step.

6.3.2 ALD coating effect on microstructure of NMC during cycle

To check the effects of Al_2O_3 ALD coating on preservation of crystal structure of the NMC, a NMC Bare and NMC/4ALD particle was carefully selected from the 100 cycled (after delithiated to 4.5V) electrode and analyzed by focused ion beam (FIB) and TEM. Fig. 5a and b shows FIB ion beam images of the cross-sectioned NMC Bare and NMC/4ALD particle. Average particle size of both the NMC Bare and NMC/4ALD is about 12 nm and each primary particle is composed of multiple grains with the size range of 1~5 nm. In Figure 3.2.3 (c~d), TEM selected area electron diffraction (SAED) patterns show that NMC Bare electrode undergoes phase transition during 100 cycles from layered structure mother phase (space group: R-3m) to spinel cubic structure (space group: Fd3m). In contrast, the Al_2O_3 -ALD coating layer preserves the original layered structure of NMC/4ALD electrode for the same cycling period as seen in Figure 3.2.3 (e~f)

In Figure 3.2.4, SR-XRD and Reitveld refinement on the NMC/4ALD sample also confirm that there is no structural change in the NMC/4ALD electrode materials after 100 charge/discharge cycles at 1-C rate. In contrast, the diffraction peaks of NMC Bare electrode after 100 cycles feature great asymmetry. This result suggests that there could be composition inhomogeneity in the NMC bare sample after 100 cycles, leading to the formation of multiple phases. These phases could be developed at the surface of the particle during the cycling, accompanied by the breaking down of particles, yielding nano-sized particles that produce the ring pattern as seen in TEM analyses. Therefore we conclude that the excellent rate capability of the NMC/4ALD

cell is mainly attributed to both preserved surface characteristics and crystal structures which are favorable to electrons and Li-ions transport during charge/discharge processes.

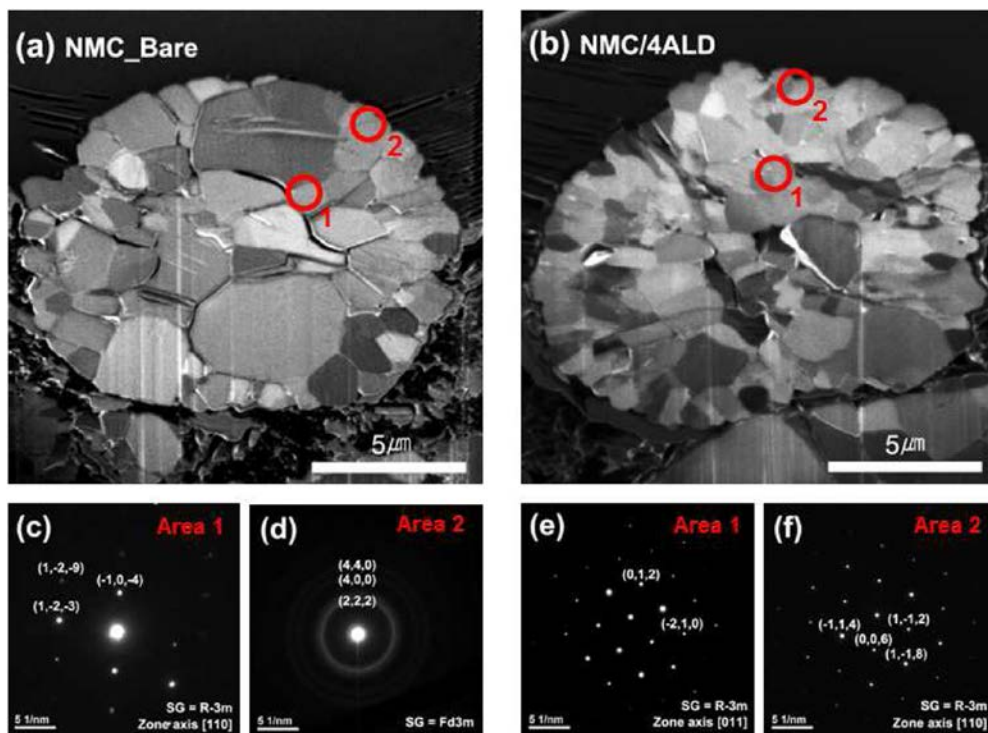


Figure 6.3 FIB cross-section images of fully charged (delithiated) (a) NMC Bare and (b) NMC/4ALD after 100 cycles at 1 C-rate between 3.0 and 4.5 V. TEM selected area electron diffraction (SAED) patterns from inner area (1) and outer area (2) of each particle show phase transition in NMC Bare electrode (c,d) whereas NMC/4ALD presents same crystal structure from inner and outer area (e,f).

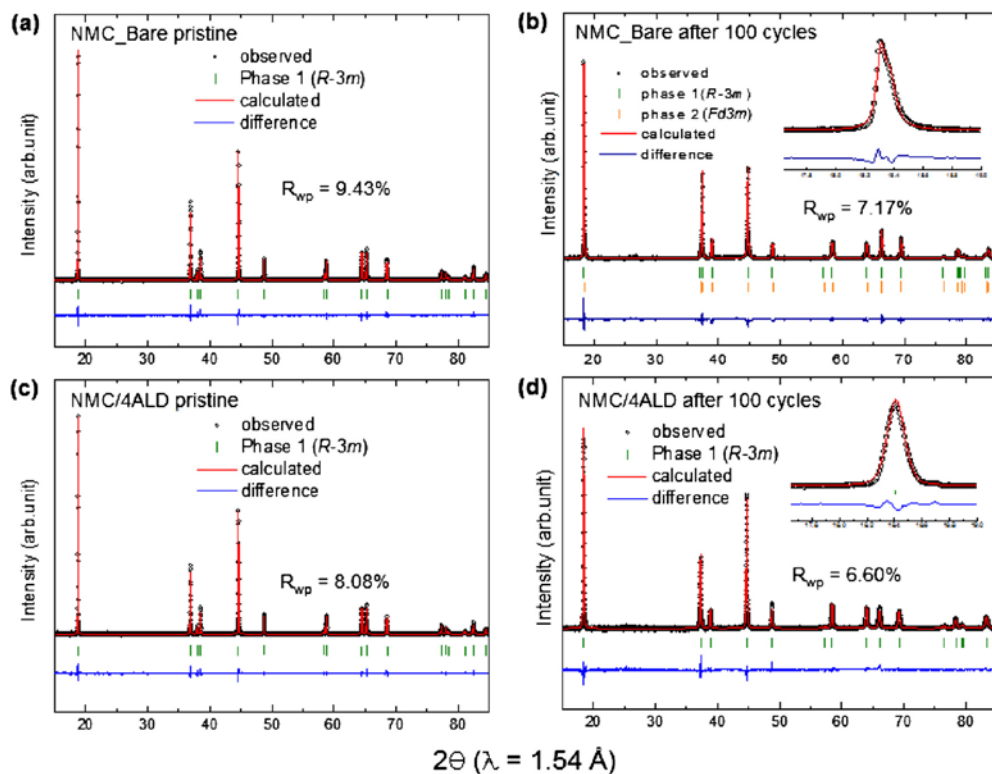


Figure 6.4 Synchrotron X-ray diffraction patterns of fully charged (a,b) NMC Bare and (c,d) NMC/4ALD at 3rd cycle and 100th cycle respectively during 1 C-rate cycling test between 3.0 and 4.5 V.

6.3.3 Life cycle performance comparison between w/ &w/o ALD

For a cathode material to meet the safety and energy requirements for Li-ion batteries in electric vehicles, the high temperature cycling performance of the cathode material must be ensured. To investigate high temperature performances of the three cells, NMC Bare, NMC:LMO and NMC/4ALD half cells are cycled at 55°C with 1 C-rate between 3.0 and 4.5 V as seen in Figure 3.2.5. The uncoated NMC (NMC Bare) exhibits a significant decline in the discharge capacity after a couple of initial cycles. The capacity retention from 3rd to 70th cycle is only 14% at 1 C-rate cycling (169 mAh/g → 24mAh/g), whereas the NMC/4ALD cell shows the best result with the highest retained capacity (92% of retention; 170 mAh/g /156 mAh/g) during the same cycling period. At lower voltage cut-off (3.0~4.3 V, 55°C C and 1 C-rate), the NMC/4ALD cell shows again an excellent cycling performance with 96% of capacity retention (148 mAhg₁ /142 mAhg₁ in contrast to each MC:LMO and NMC Bare cell only delivers 88% (119 mAhg₁/105 mAhg₁) and 36% (149 mAhg₁/54 mAhg₁) of its initial capacity as seen in Figure 3.2.6.

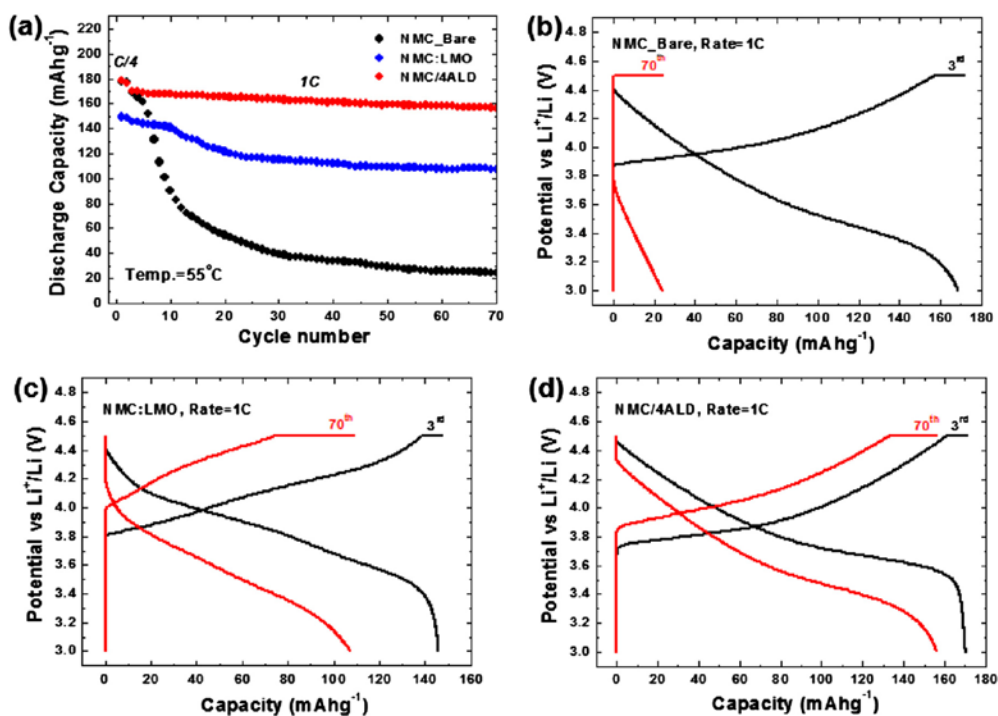


Figure 6.5 (a) Cycling performance of half cells using uncoated-NMC (NMC Bare), uncoated-MC:LMO (NMC:LMO, 1:1 mixture) and Al₂O₃ 4ALD coated-NMC (NMC/4ALD) cathodes cycled between 3.0 and 4.5 V versus Lip/Li at 55 °C by applying a constant rate of 1 C-rate (160 mA_g⁻¹ for NMC Bare and NMC/ALD and 130 mA_g⁻¹ for NMC:LMO) following after the first two formation cycles at C/4-rate (40 mA_g⁻¹ for NMC Bare and NMC/ALD and 32.5 mA_g⁻¹ for NMC:LMO). Comparison of 3rd and 70th charge/discharge voltage profiles (3.0~4.5 V) at 1 C-rate of (b) NMC Bare, (c) NMC:LMO and (d) NMC/4ALD half cells. Voltage hold was applied at 4.5 V for 0.5 h after each charge step.

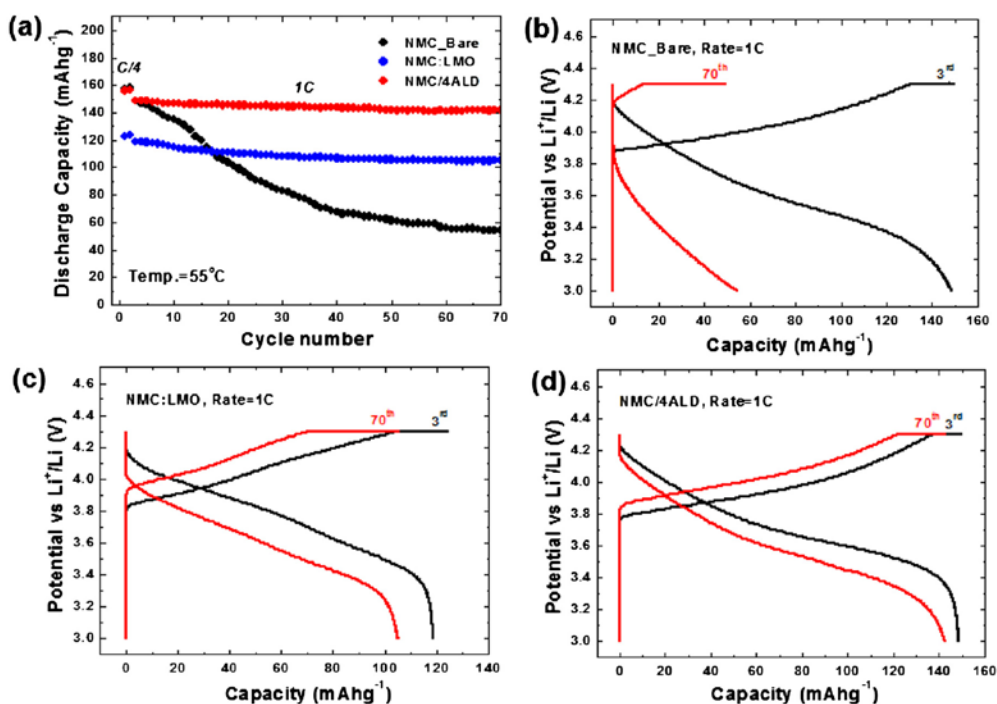


Figure 6.6 (a) Cycling performance of half cells using uncoated-NMC (NMC Bare), uncoated-MC:LMO (NMC:LMO, 1:1 mixture) and Al₂O₃ 4ALD coated-NMC (NMC/4ALD) cathodes cycled between 3.0 and 4.3 V versus Li⁺/Li at 55 °C by applying a constant rate of 1 C-rate (160 mA_g⁻¹ for NMC Bare and NMC/ALD and 130 mA_g⁻¹ for NMC:LMO) following after the first two formation cycles at C/4-rate (40 mA_g⁻¹ for NMC Bare and NMC/ALD and 32.5 mA_g⁻¹ for NMC:LMO). Comparison of 3rd and 70th chargedischarge voltage profiles (3.0e 4.3 V) at 1 C-rate of (b) NMC Bare, (c) NMC:LMO and (d) NMC/4ALD half cells. Voltage hold was applied at 4.3 V for 0.5 h after each charge step.

6.4 Conclusion

We applied Al_2O_3 -ALD coating to a spotlighted cathode material (NMC), which traditionally suffers from unacceptable rate capability and high temperature cycling performance thus necessitating the battery manufactures to blend NMC with other compensating materials, despite its high capacity. With our coating method, the coated NMC cell delivered a high capacity (166 mAh/g, 3.0~4.5V, 1 C-rate) and maintained excellent capacity retention over 96% during long-term cycling. At the same time, a demand for high power density was also satisfied by our ALD coating process with the improved rate capability of the coated NMC. This outstanding rate capability of the NMC/4ALD cell (~137 mAh/g at 4 C-rate), which is four times faster than the NMC:LMO cell (~125 mAh/g at 1 C-rate), demonstrates that the Al_2O_3 -ALD coating layer dramatically prevents an increase in cell resistances and a slowdown in Li ion kinetics by preserving the crystal structure of the NMC. This durable ultra-thin Al_2O_3 -ALD coating layer also worked to improve stability for the NMC at an elevated temperature (55°C). Thus we successfully obtained a remarkable capacity (170 mAh/g, 3.0~4.5 V, 1 C-rate) together with a high retention (92%) which is stable at high temperatures. We believe our work offers significant advantages to most of the layered lithium transition-metal oxide cathodes by addressing the raised issues; poor cycle-life, slow rate capability, and safety concerns at high temperature, without severe loss in their original energy density. Therefore, we anticipate that our work will spark much interest in Li-ion battery and electric vehicle manufacturers who are actively seeking high energy, power and safe cathode materials for Li-ion

batteries.

6.5 Reference

- [1] Ji Woo Kim, Jonathan J. Travis Enyuan Hu, Kyung-Wan Namc, Seul Cham Kim, Chan Soon Kang, Jae-Ha Woo a, Xiao-Qing Yang, Steven M. George, Kyu Hwan Oh, Sung-Jin Cho, Se-Hee Lee, *Journal of Power Sources* 254 (2014) 190e197
- [2] N. Yabuuchi, T. Ohzuku, *J. Power Sources* 119e121 (2003) 171.
- [3] I. Belharouak, Y.-K. Sun, J. Liu, K. Amine, *J. Power Sources* 123 (2003) 247.
- [4] S. Jouanneau, K.W. Eberman, L.J. Krause, J.R. Dahn, *J. Electrochem. Soc.* 150 (2003) A1637.
- [5] K.M. Shaju, P.G. Bruce, *Adv. Mater.* 18 (2006) 2330.
- [6] I. Belharouak, W. Lu, D. Vissers, K. Amine, *Electrochem. Commun.* 8 (2006) 329.
- [7] N. Yabuuchi, T. Ohzuku, *J. Power Sources* 146 (2005) 636.
- [8] Z.H. Chen, Y.-K. Sun, K. Amine, *J. Electrochem. Soc.* 153 (2006) A1818.
- [9] K. Amine, Z. Chen, Z. Zhang, J. Liu, W. Lu, Y. Qin, J. Lu, L. Curtis, Y.-K. Sun, *J. Mater. Chem.* 21 (2011) 17754.
- [10] M. Alamgir, K. Yoo, B. Koetting, M. Klein, in: Presented at 2011 DOE Hydrogen Program and Vehicle Technologies Office Annual Merit Review and Peer Evaluation Meeting, Arlington, VA, 10 May 2011.
- [11] M.M. Thackeray, *Prog. Solids Chem.* 25 (1997) 1.
- [12] A. Blyr, C. Sigala, G. Amatucci, D. Guyonard, Y. Chabre, J.-M. Tarascon, *J. Electrochem. Soc.* 145 (1998) 194.

- [13] Y.S. Jung, A.S. Cavanagh, A.C. Dillon, M.D. Groner, S.M. George, S.H. Lee, J. Electrochem. Soc. 157 (2010) A75.
- [14] Y.S. Jung, A.S. Cavanagh, A.C. Dillon, M.D. Groner, S.M. George, S.H. Lee, Adv. Mater. 22 (2010) 2172.
- [15] I.D. Scott, Y.S. Jung, A.S. Cavanagh, Y. Yan, A.C. Dillon, S.M. George, S.H. Lee, Nano Lett. 11 (2011) 414.
- [16] L.A. Riley, S.V. Atta, A.S. Cavanagh, Y. Yan, S.M. George, P. Liu, A.C. Dillon, S.H. Lee, J. Power Sources 196 (2011) 3317.
- [17] S.M. George, Chem. Rev. 110 (2010) 111.

Chapter 7. Conclusion

In this thesis, I studied the microstructure to achieve the good life properties of the Li-ion batteries. Part 1, it was proposed microstructure for good life properties implementations of the silicon anode materials. (1) In order to enhancing life cycle performance, grain size refinement, well mixed uniform structure and strong bonding force between primary particles are required. MA Si alloys are composed ultrafine amorphous free Si and Fe-Silicide. Continuous amorphous Si phase is role as a path of Li transparent and Fe-silicide is as a role of stress relaxation induced by Si volume expansion. Uniform microstructure can prevent occurring imbalance stress. Carbon coating process increase bonding force between primary particles. Since dense particles are less exposed to electrolyte, it prevent forming SEI layer inside of secondary particle. In this study stable Si alloy microstructure for enhanced life cycle performance derived. And In this study, I measured volume expansion behavior of the electrode materials using discharge voltage difference. Expansion of the electrode is not only Si alloy, the expansion of the graphite also have a significant impact. In Si alloy system, Si included matrix became solid electrolyte to transfer Li ion to inside free Si particles during Lithiation.

(2) In order to prevent mechanical fracture of Si particles and formation SEI layer, C coating process on surface is must needed. Good ionic conductivity of cyclized-PAN coatings is assumed based upon good electrochemical performance at fast cycling rates. In this study, our method has economic advantages, this method is based on low-cost polymer precursor and adaptable to other anode or cathode

materials. And it can form a stable SEI layer on changing the composition of the electrolytic solution. I provided in-depth characterization of the Si-PYR13FSI system and proposed a mechanism for the system's stability through a remarkably robust SEI.

(3) In this study, I present Si/AC fabrication using liquid state pitch carbon. This method is appropriated for carbon coating regardless shape and size of particles. For faster transport of Li ions, Si diffuse in AC matrix by ionic migration. Diffused Si forms 3D network structure inside Si/AC composite. After long cycle enough, whole particle area will become Si- C mixed area that is stable for mechanical and chemical. We expected that Si-C mixed area has good ionic conductivity for using new solid state electrolyte.

Part 2 is observation of micro structure change of cathode materials solid and liquid electrolyte during cycle progress. Comparison advantages and disadvantages of solid and liquid electrolyte batteries. (1) In solid state electrolyte pyrite cathode battery, that charge products are nano-crystalline orthorhombic-FeS₂ particles encased in non-stoichiometric FeS_y and sulfur is consistent with prior research and our observations. Nano-crystalline orthorhombic-FeS₂ particles enable faster reduction kinetics such that subsequent discharges are not kinetically limited and can occur at a higher potential. (2) In liquid electrolyte pyrite cathode battery, Al₂O₃-ALD coating layer dramatically prevents an increase in cell resistances and a slowdown in Li ion kinetics by preserving the crystal structure of the NMC. This study offers significant advantages to most of the layered lithium transition-metal oxide cathodes by addressing the raised issues; poor cycle-life, slow rate capability, and safety concerns

at high temperature, without severe loss in their original energy density.

Appendix 1. Thermal stability of ZnS nanowires studied by using in-situ heating X-ray diffraction

8.1 Introduction

8.1.1 1D semi-conductor nano materials.

Recently, the research for a down-scalable nanoelectronics device that combines rapid operation, cheaper cost, and minimization has been focused on the exploration of novel nano-structured systems [1]. From this perspective, one-dimensional (1-D) semiconductor nanomaterials have been extensively researched due to their unique geometry, properties and potential applications, such as electrical, optical, magnetic, and thermoelectric devices [2–6]. If a nano-electronic device based on a nano-structure building block is to be realized, 1-D nano-material properties with mechanical, structural, and thermal stability in a vigorous environment are required [7–9]. Especially, the thermal stability of the 1-D nano-materials building block is one of the most important keys, which allow a nano-electronic device to operate well even in critical surroundings.

8.1.2 ZnS nanowire

Among various methods to characterize the thermal stability of 1-D nano-materials, X-ray diffraction (XRD) with in-situ heating is used because it allows the detection of structural changes even in organic and inorganic nano-scale material systems [10,11]. We adopted an in-situ heating XRD system to investigate the thermal

stability of 1-D nano-materials. Among several semiconductor 1-D nano-materials, we use ZnS nanowires as a model system to characterize the thermal stability by using an in-situ heating XRD system. ZnS is an important II-VI group semiconductor with good optical properties (direct bandgap energy = 3.68 eV at 300 K) and has recently been considered as the most promising material for optical and electrical device applications, such as displays, electroluminescence devices, infrared windows, ultraviolet (UV) lasers, sensors, etc [12–16]. In addition, we employed scanning electron microscopy (SEM) and transmission electron microscopy (TEM) for morphological and structural analysis of the in-situ heating XRD measurement.

8.2 Experiment procedure

8.2.1 Synthesis of ZnS nanowire

The synthesis of ZnS nanowires was achieved by using a metal-organic chemical vapor deposition (MOCVD) process with a $\text{Zn}(\text{S}2\text{CNEt}_2)_2$ single molecular precursor [17]. A Au/Pd (molar ratio 4 : 6) thin film was plasma-sputtered on a clean oxide-covered Si substrate (SiO_2 thickness ~400 nm) for 1 minute, which subsequently served as the catalytic site for ZnS nanowire nucleation and growth. The Au/Pd-film-deposited substrate was then placed downstream in a horizontal tube furnace, and $\text{Zn}(\text{S}2\text{CNEt}_2)_2$ single molecular precursors were positioned upstream. The furnace temperature was slowly raised to 890°C (substrate temperature: ~770°C), and the quartz tube was pumped down to a base pressure of 10^{-2} Torr with pure Ar (99.99%

purity) introduced into the tube at a flow rate of 50 sccm (sccm denotes cubic centimeter per minute at STP). After the furnace had been stabilized at the process pressure of 100 Torr, the precursor was slowly pushed into the hightemperature zone of the furnace, and ZnS nanowires growth was performed for 10 minutes. Figure 8.1(a) displays a simple diagram of as-synthesized ZnS nanowires via Au/Pd-mediated vapor-liquid-solid reaction, which is described elsewhere [18,19].

8.2.2 Characterize the thermal stability of ZnS nanowire

To characterize the thermal stability of the assynthesized ZnS nanowires, we transferred the products into an in-situ heating XRD system (Philips X'pert Pro) equipped with a high-temperature oven chamber (Anton Paar HTK 1200N). After the as-synthesized ZnS nanowires had been loaded at in-situ heating stage, the XRD system was pumped down to a base pressure of 10 mTorr and then kept there for 5 minutes to stabilize the system. The procedure for the XRD analysis at the temperatures ranging from 25°C to 900 °C was depicted

in Figure 8.1(b). As for the in-situ heating process, the heating stage in the XRD system was ramped, with the temperature increasing at a rate of 5 °C/min. On Fig. 2. X-ray diffraction pattern by in-situ heating at (a) 25°C, (b) 500°C, (c) 600°C, (d) 700°C, (e) 800°C, and (f) 900°C. (g) Low-magnification 70° tilted SEM image of assynthesized

ZnS nanowires. (h) High-magnification 70° tilted SEM image of as-synthesized ZnS nanowires. the other hand, the phase composition change of the assynthesized ZnS

nanowires was measured in intervals of 100°C, and was recorded using Cu K radiation ($\lambda=0.154\text{nm}$) and a 2 theta scan from 20° to 60°. The red circles in Figure 8.1(b) represented data obtained for a 10 minute recording time at each measurement. In addition, SEM (FEI NOVA NANO200) and TEM (JEOL 3000F) were utilized to characterize the microstructure of ZnS nanowires corresponding to in-situ heating experiment in the XRD system.

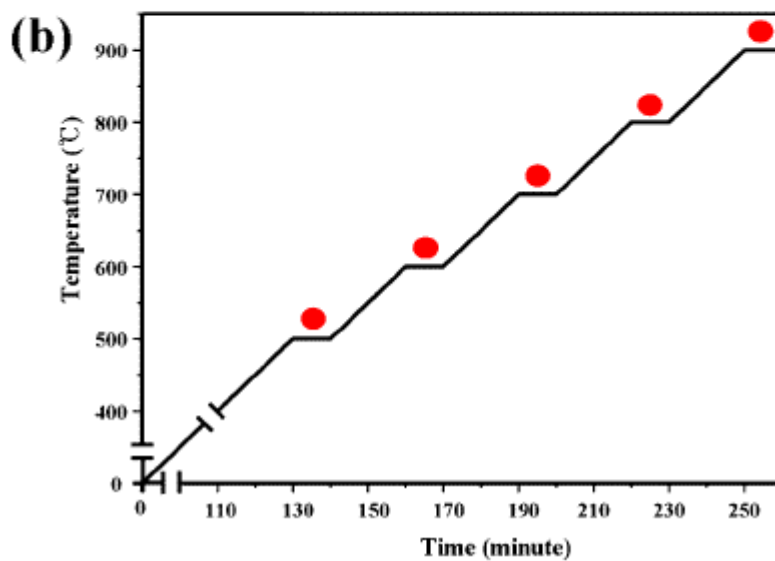
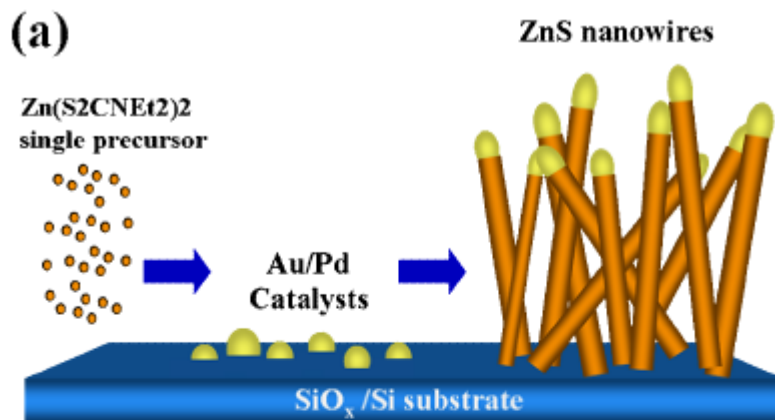


Figure 8. 1 (a) Schematic representation of ZnS nanowires showing the Au/Pd-catalyzed VLS reaction. (b) In-situ heating XRD measurement diagram (Red circle: XRD data acquisition time for 10 min)

8.3 Results and discussion

Figure 8.2 shows the XRD patterns corresponding to structures in the ZnS nanowires at 25°C, 500°C, 600°C, 700°C, 800°C, and 900°C. The XRD patterns of as-synthesized ZnS nanowires are shown in Figure 8.2(a) with a series of ZnS peak, (111) = 28.557°, (200) = 32.979°, (220) = 47.566 °C , (311) = 56.376° (JCPDS card No.05-0566) and a Au/Pd texture peaks (111) = 39.018° [20]. As the temperature was increased to 400 °C no significant changes, compared to the as-synthesized ZnS nanowires, were observed; thus, the nanowires maintained their sphalerite structure till 400°C. Interestingly, when the temperature reached 500°C, the XRD peaks were reduced over all the scanned area, and the (200) peak decrease is seen clearly in Figure 8.2 (b). As the temperature was increased to 600°C, a decrease in the peak intensities over all the scanned range was observed continuously, as in Figure 8.2 (c). XRD patterns obtained by using extended heating from 700°C to 900°C are shown in Figure 8.2 (d~f). As shown in Figure 8.2(d), a pure Zn (200) peak was observed in the data recorded 700°C, which is thought to be from partial decomposition of ZnS nanowire. Hence, a decrease in the ZnS (111) peak is also clearly seen in Figure 8.2(d). From these results, we can infer that the ZnS sphalerite structure is degraded abruptly at 700°C because we found a partial decomposition of ZnS and a decreased in the peak associated with the ZnS (111) closed packing plane with surface energy minimization. From Figure 8. 2(e) and (f), we find that this tendency, which started from 700°C, was sustained until the temperature reached 900°C. Figure 8.2 (g~h) show 70°tilted SEM images of as-synthesized ZnS nanowires. Figure 8.2 (g) shows

that the ZnS nanowires grew over almost all the area of the Si substrate. There are no clusters around the root of the ZnS nanowire in Figure 4.2 (h). This confirmed that the XRD peaks came from the nanowire. To explore morphological changes in the ZnS nanowires due to the in-situ heating process, we conducted an SEM analysis on as-synthesized and final (heat-treated at 900) ZnS nanowires. Figure 8.3 (a) shows a low-magnification SEM image of as-synthesized ZnS nanowires with lengths up to tens of micrometers.

Figure 8.4 (a) Low-magnification TEM image of as-synthesized ZnS nanowire. (b) HRTEM image at upper part of as-synthesized ZnS nanowire (inset: FFT pattern showing [111] growth direction). (c) TEM image of ZnS nanowires obtained by 900°C heat-treatment. (d) HRTEM image of degraded ZnS nanostructure (inset: FFT pattern corresponding to HRTEM image). Representative high-magnification SEM image in Figure 8.3(b) shows that the as-synthesized ZnS nanowires possessed diameters of ~80 nm and a Au/Pd catalyst on top of the nanowire, which means Au/Pd-catalyzed VLS growth method. Figs. 3(c) and (d) show SEM images corresponding to final ZnS nanowires after in-situ heating at 900°C. As shown in Figure 3(c), ZnS nanowires were observed with less density, smaller diameter and shorter length compared to Figure 3(a). These differences can be explained as being due to a partial decomposition and a structural degradation of the ZnS nanowires, as depicted in Figure 8.2 (d-f). Figure 8.3(d) displays a high magnification SEM image of Figure 8.3 (c). Tangled and shrunken ZnS nanowires are found in Figure 8.(d). Through the Au/Pd catalyst can be observed on top of the ZnS nanowire, the degradation of the

ZnS nanowire can be clearly seen. To make a quantitative morphology comparison between the initial and final products, we measured the diameters of the initial and the final products by using SEM images showing hundreds of ZnS nanowires (data not shown). Through the quantitative comparison, we found that the diameter of final product was decreased by ~40% compared to that of the as-synthesized product.

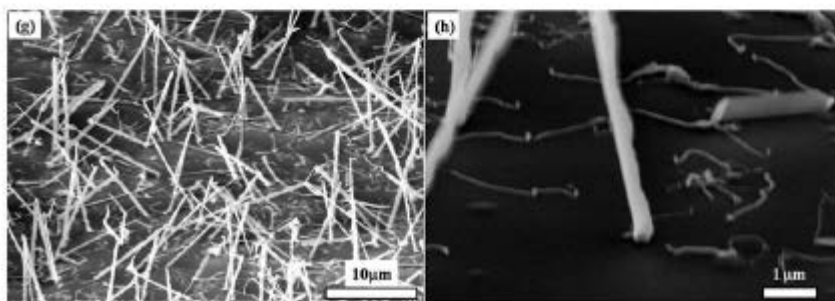
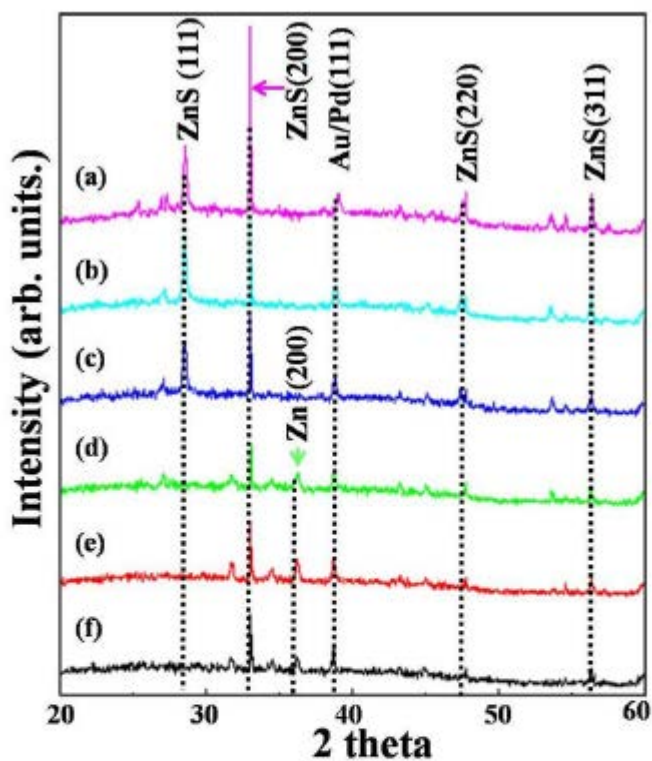


Figure 8.2 X-ray diffraction pattern by in-situ heating at (a) 25°C, (b) 500°C, (c) 600°C, (d) 700°C, (e) 800°C, and (f) 900°C. (g) Low-magnification 70°tilted SEM image of as-synthesized ZnS nanowires. (h) High-magnification 70 tilted SEM image of as-synthesized ZnS nanowires.

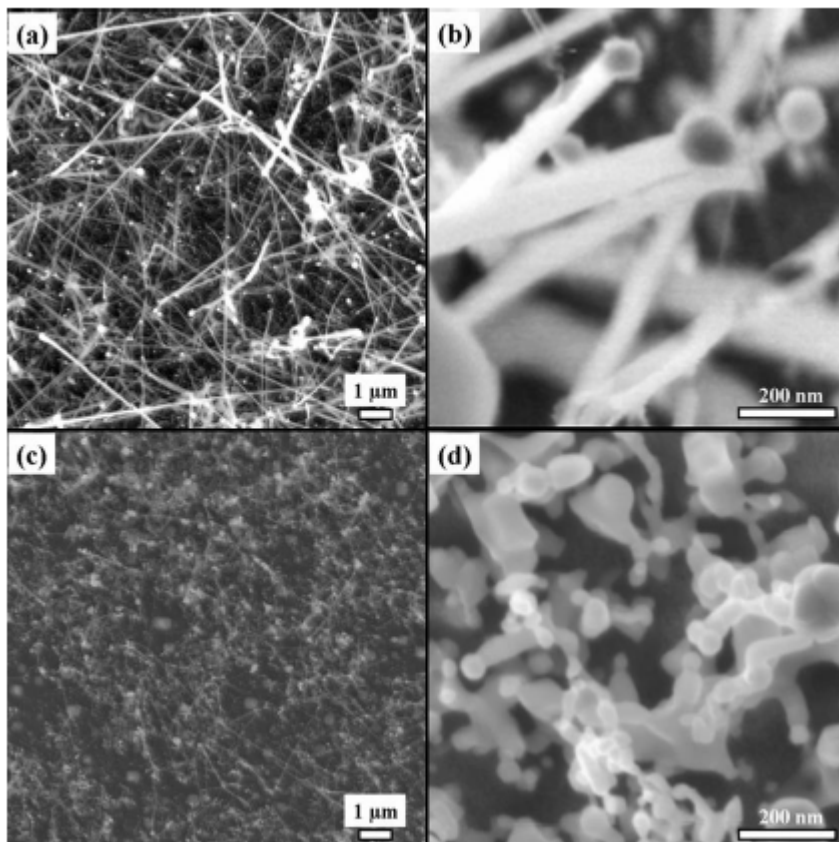


Figure 8.3 (a) Low-magnification SEM image of as-synthesized ZnS nanowires. (b) Enlarged SEM image of as-synthesized ZnS nanowires. (c) SEM image of ZnS nanowires obtained by 900°C heat-treatment. (d) High-magnification SEM image of (c).

To gain better structural information with respect to the initial and the final ZnS products, we employed high-resolution (HR) TEM and conducted a structural analysis via fast Fourier transformation (FFT). Figure 8.4 (a) presents a representative TEM image of ZnS nanowire recorded at a low magnification to illustrate a diameter of ~70nm and a Au/Pd-mediated VLS reaction. As shown in Figure 8.4 (b), a HRTEM investigation was conducted for the upper part of the as-synthesized ZnS nanowire. HRTEM and FFT pattern studies reveal that the ZnS nanowire possesses a sphalerite single-crystalline structure in the [111] growth orientation. Figure 8.4(c) and (d) show TEM images corresponding to the final ZnS nanowires products heat-treated at 900°C. In Figure 8.1 (c), we find a tangled and degraded ZnS nanostructure, compared to the as-synthesized product, which is co-related with partial ZnS nanowire decomposition and crystalline degradation at 900°C. Figure (d) displays a HRTEM image of a degraded ZnS nanostructure. Though we investigated the crystallinity over the entire degraded ZnS nanostructures by using HRTEM, we acquired no distinct information because crystallinity disappeared abruptly, from the XRD peaks obtained at 700°C.

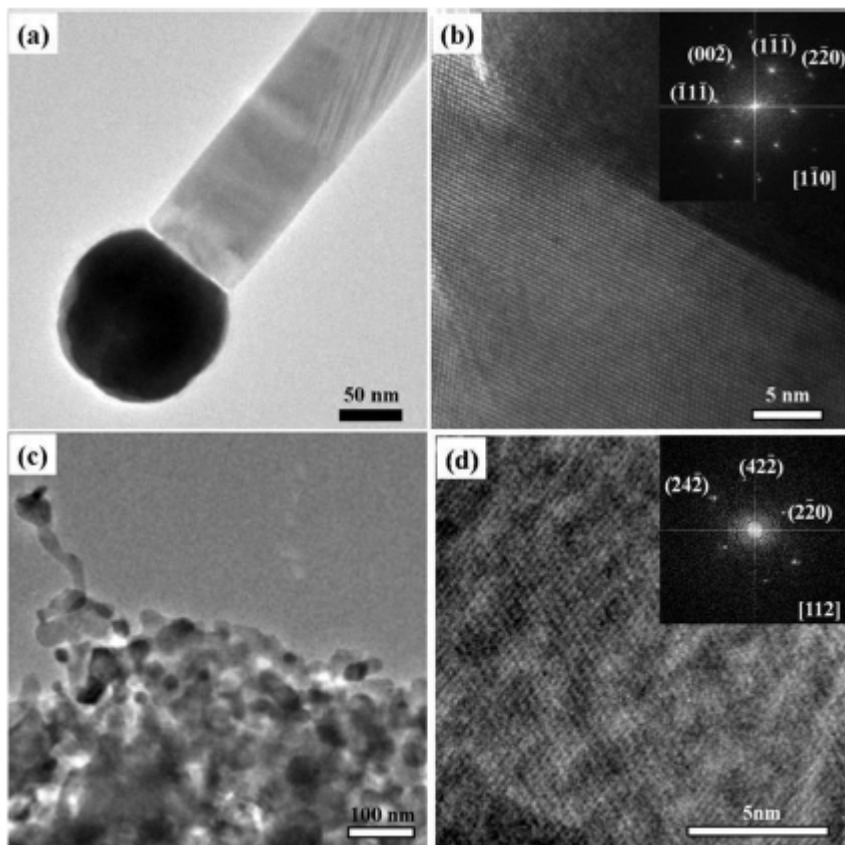


Figure 8.4 (a) Low-magnification TEM image of as-synthesized ZnS nanowire. (b) HRTEM image at upper part of as-synthesized ZnS nanowire (inset: FFT pattern showing $[111]$ growth direction). (c) TEM image of ZnS nanowires obtained by 900 heat-treatment. (d) HRTEM image of degraded ZnS nanostructure (inset: FFT pattern corresponding to HRTEM image).

8.4 Conclusion

In this work, we characterized the thermal stability of ZnS nanowires by using in-situ heating X-ray diffraction. As-synthesized ZnS nanowires had a sphalerite structure that was maintained to 400°C, as evidenced by the little change in the XRD patterns obtained at temperatures up to 400°C. In the temperature range of 500°C ~900°C, the crystallinity of the as-synthesized ZnS nanowires appeared to decrease. Especially, a pure Zn (200) was observed in the XRD pattern obtained at 700°C, which is associated with a partial ZnS nanowire decomposition. Further, the (111) and the (200) peaks of ZnS nanowires decreased abruptly in the XRD data obtained at 700°C. To investigate morphological and structural difference between the initial and the final ZnS products, we employed electron microscopes. From SEM and TEM analyses, we confirmed that as-synthesized ZnS nanowires were structurally degraded, with tangled features and a size reduction after the in-situ heating XRD process at 900°C. This method of in-situ heating XRD system is expected to have more applications in nano-scale systems.

8.5 Reference

- [1] P. S. Peercy, *Nature* 406, 1023 (2000).
- [2] Y. Cui and C. M. Lieber, *Science* 291, 851 (2001).
- [3] T. Wang, F. Ranalli, P. J. Parbrook, R. Airey, J. Bai, R. Rattlidge and G. Hill, *Appl. Phys. Lett.* 86, 103103 (2005).
- [4] J. I. Martina, J. Nogues, K. Liuc, J. L. Vicente and I. K. Schuller, *J. Magn. Magn. Mater.* 256, 449 (2003).
- [5] M. Fardy, A. I. Hochbaum, J. Goldberger, M. M. Zhang and P. Yang, *Adv. Mater.* 19, 3047 (2007).
- [6] J. Schrier, D. O. Demchenko and L. W. Wang, *Nano Lett.* 7, 2377 (2007).
- [7] D. Moore and Z. L. Wang, *J. Mater. Chem.* 16, 3898 (2006).
- [8] X. Li, X. Wang, Q. Xiong and P. C. Eklund, *Nano Lett.* 5, 1982 (2005).
- [9] Y. Liu, G. Xi, S. Chen, X. Zhang, Y. Zhu and Y. Qian, *Nanotechnology* 18, 285605 (2007).
- [10] S. Y. Wu, J. Y. Ji, M. H. Chou, W. H. Li and G. C. Chi, *Appl. Phys. Lett.* 92, 161901 (2008).
- [11] L. Vieille, I. Rousselot, F. Leroux, J. P. Besse and C. T. Gue'ho, *Chem. Mater.* 15, 4361 (2003).
- [12] T.V. Prevenslik, *J. Lumin.* 87, 1210 (2000).
- [13] J. S. Sebastian, H. C. Swart, T. A. Trottier and S. L. Jo, *J. Vac. Sci. Technol. A* 15, 2349 (1997).
- [14] H. Yang P. H. Holloway and B. B. Ratna, *J. Appl. Phys.* 93, 586 (2003).

- [15] J. T. Vallin, G. A. Slack, S. Roberts and A. E. Hughes, *Phys Rev. B* 2, 4313 (1970).
- [16] P. Calandra, M. Goffredi and V. T. Liveri, *Physicochem. Eng. Aspects* 160, 9 (1999).
- [17] C. J. Barrelet, Y. Wu, D. C. Bell and C. M. Lieber, *J. Am. Chem. Soc.* 125, 11498 (2003).
- [18] H. S. Chung, Y. Jung, T. J. Zimmerman, S. H. Lee, J. W. Kim, S. H. Lee, S. C. Kim, K. H. Oh and R. Agarwal, *Nano Lett.* 8, 1328 (2008)
- [19] R. S. Wagner, W. C Ellis and M. Hill, *Appl. Phys. Lett.* 4, 89 (1964).
- [20] Z. Zhao and M. A. Carpenter, *J. Appl. Phys.* 97, 124301 (2005).

Appendix 2. Martensite in interstitial-free steel obtained by ultra-high pressure

9.1 Introduction

9.1.1 Interstitial Free steel

Interstitial-free (IF) steel is a steel product in which the interstitial elements C and N are scavenged by the controlled addition of Ti or Nb. The formation of Ti- or Nb-carbonitride precipitates makes the steel matrix almost free of solute interstitials. Besides the scavenging of solute C and N, IF steels inherently contain a very small amount of the interstitial elements in their nominal composition [1]. In general, the content of other substitutional elements is also relatively very low. Although their strength is generally low because of the very lean alloying, cold-rolled and annealed IF steel sheets have excellent formability and especially superior drawability by virtue of their optimal recrystallization textures. Therefore, they have been widely used in the outer shells of cars, household appliances and beverage cans [1–3].

Because of the lean alloying, the hardenability of IF steels should be extremely shallow. By conventional water quenching, therefore, it is generally impossible to observe martensitic transformation in IF steels. Indeed, a martensitic structure in IF steel has very rarely been reported or documented. In a limited number of studies [4,5], martensitic structures in IF steels of rather high alloying were observed after rapid quenching with iced brine or water. Martensitic IF steels show greater microstructural refinement [4,5], and this could compensate for their deficit in

strength. In this study, an attempt was made to obtain a martensitic structure in IF steels at a rather slow rate of cooling with the aid of ultra-high pressure.

9.1.2 High pressure high temperature

The chemical composition of the IF steel used in this study is presented in Table 1. This steel was designed to have more strength than a typical grade of IF steels. The C and Mn contents are relatively high compared to those of typical ultra-low-carbon (ULC) products, while the C content is still low enough to be fully stabilized by the amount of Ti and Nb added. A relatively large amount of Mn and a small addition of B enhance hardenability. However, the amounts of the two elements are considerably less than those used in Refs. [4] and [5], and therefore the hardenability is also considerably less.

9.2 Experiment procedure

9.2.1 High pressure high temperature

Specimens from a hot-rolled sheet were austenitized at high temperatures and cooled. To perform heat treatment under ultra-high pressure, we used the high-pressure high-temperature (HPHT) technology developed for diamond synthesis [6–8]. In this study, a cube-type anvil press [9] installed in the pilot plant of ILJIN Diamond Co. Ltd. was used to generate the HPHT condition. A coin-shaped specimen with a diameter of 30 mm and a thickness of 4 mm was inserted into a reaction cell designed for sintering of polycrystalline diamond composite. The structure of the reaction cell is illustrated in Figure 1. It was pressed on all six surfaces with 85 MPa of pressure by the anvils

while it was heated to 1200°C at 10°C/sec, held for 10 min, then cooled to roomtemperature at 8°C/sec. As the NaCl in the cell melted, the reaction cell experienced an internal hydrostatic pressure of approximately 5 GPa due to the volume expansion of NaCl in melting. After cooling was complete, the external force was removed, the cell was disassembled and the coin-shaped specimen of IF steel was finally retrieved. During the process, the specimen was encapsulated in Ta foil, which prevented any contamination from contact with other materials during the process. However, because Ta is a strong carbide former, it could also scavenge the solute C from the specimen to form a Ta-carbide film on the surface, resulting in a reduction in hardenability.

9.2.2 Microstructure analysis

The microstructure at the mid-thickness region of the specimen core was examined using electron backscattering diffraction (EBSD) and a transmission electron microscopy (TEM). It was also compared with microstructures produced under atmospheric pressure.

C	Mn	Ti	Nb	Al	B
0.0042	0.909	0.013	0.031	0.005	0.0005

Table 9.1 Chemical composition of IF steel used in the study (wt.%).

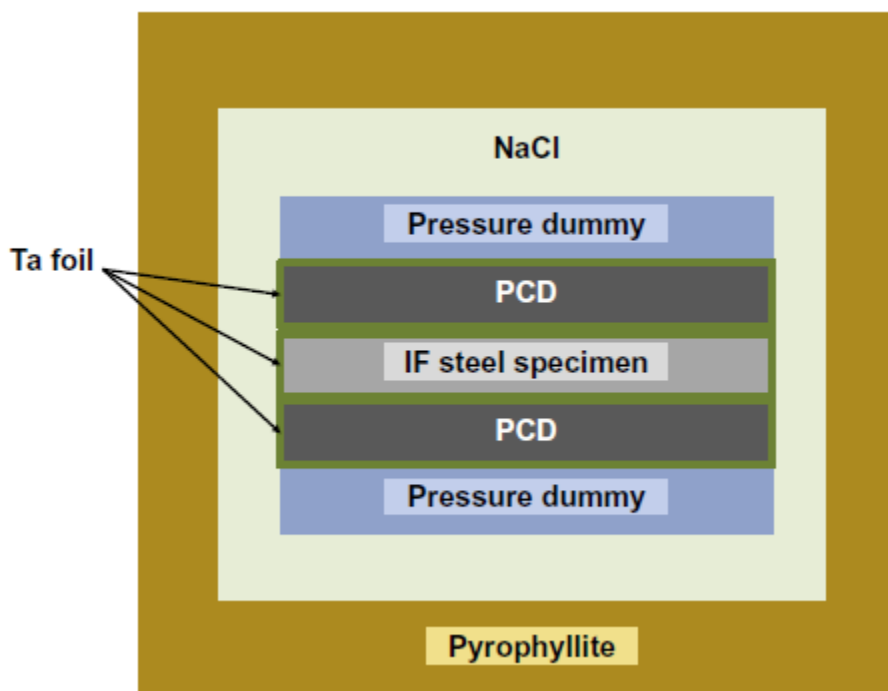


Figure 9.1. The structure of the reaction cell for the HPHT process. The pressure dummy is a plain carbon steel and the dimension is optimized for the preset conditions of pressure and temperature (5 GPa, 1200°C).

9.3 Results and discussion

Figure 2 shows the microstructure of the specimen after the HPHT process. In Figure 2(a), the prior austenite boundary and the subdivision of the prior austenite grains by blocks and packets of laths can be recognized. The average diameter of prior austenite grains was estimated to be 186 nm. In Figure 2(b), a more detailed morphology of individual laths with dislocation tangles can be also observed. These correspond well to the typical characteristics of lath martensite [10]. From Figure 2(c), it is clear that a large proportion of the packet boundaries shows a twin relationship, which has also been reported as a characteristic of low-carbon martensite [11,12]. From these features, it can be concluded that full-lath martensite has been obtained in an IF steel with extremely shallow hardenability, even without quenching, by the use of ultra-high pressure. Figure 3 shows typical microstructures of the same steel after austenitization under atmospheric pressure.

Figure 3(a) and (b), which resulted from different cooling rates (8 and 50°C/sec respectively), show essentially the same character. They do, however, show a large variation in grain size and highly irregular grain shapes with ragged boundaries. Moreover, many grains contain sub-boundaries and consequently exhibit internal orientation gradients due to the dislocations introduced during transformation. This type of microstructure can be regarded as a massive or quasi-polygonal ferrite, which is a higher-temperature product of austenite decomposition than martensite and is frequently encountered in ULC steels [12–15]. It can also be observed that further subgranular structures evolve as the cooling rate is increased. However, at least up to

50°C/sec , a clearly aligned subdivision like that in lath martensite cannot be observed. It is generally considered that a martensitic structure in IF steels would be difficult to obtain under atmospheric pressure, even with more rapid cooling [14,15]. Although martensite can be found in high-purity iron with a comparable carbon content, the required cooling rate is several thousand (5000–35,000) °C/sec [16].

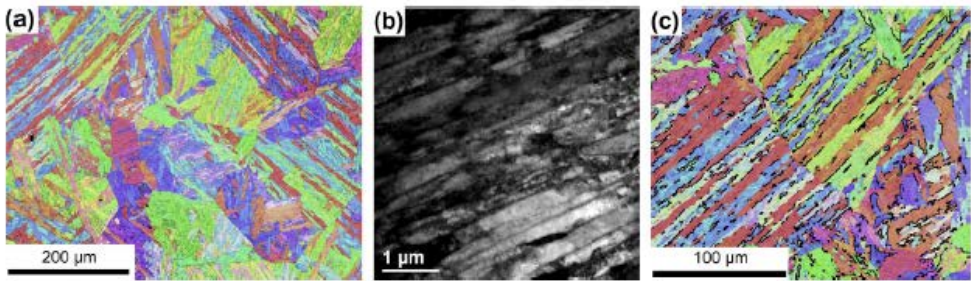


Figure 9.2. Microstructure after HPHT process: (a) EBSD orientation map overlaid on band contrast map, (b) TEM micrograph and (c) distribution of twin boundaries (thick black lines) in the upper-left part of (a).

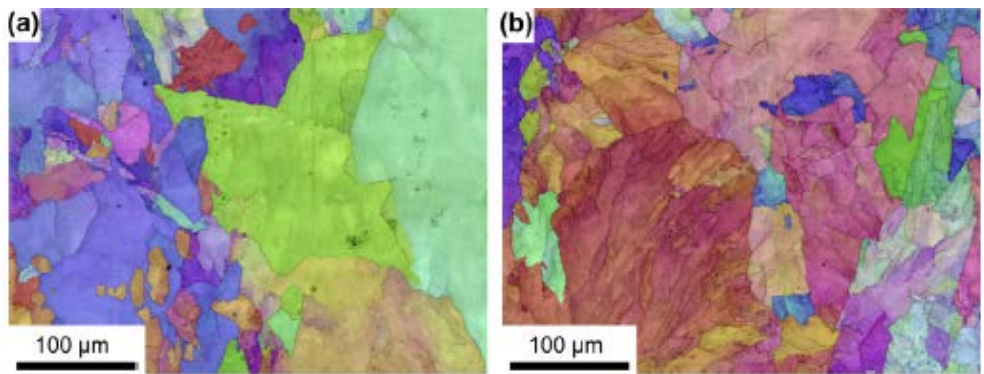


Figure 9.3. Microstructures produced under atmospheric pressure, heated to 1150°C at 10°C/sec, held for 10 min and cooled at (a) 8 and (b) 50°C/sec

The hardness of the HPHT specimen was 236 HV, while that of the microstructures shown in Figure 3(a) and (b) was only 81 and 118 HV, respectively. This hardness comparison reflects dramatic strengthening through martensitic transformation based on transformation strain and microstructure refinement. In this case, however, the supersaturation effect of C or N would be diminished.

The criticism might be made that the two specimens treated under atmospheric pressure were austenitized at a lower temperature (1150°C) than the HPHT specimen (1200°C/sec), resulting in decreased hardenability. Strictly speaking, a direct comparison between the two types of microstructures shown in Figures 2 and 3 cannot be justified. However, the cooling rate under atmospheric pressure (50°C/sec) was considerably faster than that under high pressure (8°C/sec), which might counterbalance the effect of the lower austenitization temperature. In Ref. [16], little effect of austenitization temperature was reported. Meanwhile, the HPHT specimen should experience a reduction in hardenability due to the additional scavenging of C by the Ta foil. In spite of these factors, the HPHT process resulted in a martensitic structure which was clearly distinct from the massive ferrite, which provided confirmation that great retardation of ferrite transformation can be achieved using high pressure. It must be emphasized that the cooling rate in the HPHT process was far lower than in a typical quenching situation (greater than approximately 50°C/sec). Generally, as pressure increases, denser phases are favored in the transformation. From this point, it can be easily inferred that the close-packed face-centered cubic

austenite is more stable than the body-centered cubic ferrite under pressure. Moreover, it can be confirmed from phase diagrams that hydrostatic pressure stabilizes austenite [17–20]. Therefore, the retardation of ferrite transformation under pressure is considered to originate from the thermodynamic stabilization of austenite, which has been intensively discussed in a number of studies [19–22]. For example, the equilibrium transformation temperatures (A_3) of high-purity irons decrease from about 910°C to 600–730°C when pressure increases from atmospheric level (about 105Pa) to 5 GPa [17–20]. It is interesting that the latter temperature range falls well within the reported temperature range (540–750°C) of martensitic transformation in high-purity iron at atmospheric pressure [16]. Nevertheless, this cannot support the martensitic transformation in that temperature range under a high pressure of about 5 GPa because pressure also lowers the martensitic transformation temperature as well as the equilibrium one [20–22]. However, it is evident that the reduced driving force for the transformation greatly suppresses the ferrite formation in both aspects of transformation temperature and kinetics, by which martensitic transformation at a low temperature is preferred [20–22].

The great retardation of transformation under pressure has been shown as displacement of the transformation–time–temperature curve [20,21]. Under a very high pressure, an extremely slow cooling rate would be required to obtain a product of diffusional transformation such as polygonal ferrite, even though the cooling actually passes through the temperature regime in which the diffusional transformation can take place.

9.4 Conclusion

In summary, a rare, fully martensitic structure of IF steel has been achieved without quenching by use of ultra-high hydrostatic pressure. The thermodynamic stability of austenite increases under high pressure, which greatly retards the ferrite transformation in an IF steel with negligible intrinsic hardenability, resulting in the martensitic structure. Currently, the industrial significance of this may be questioned. However, it is worth knowing that the effectiveness of pressure can be considered as a new parameter for microstructure control, in addition to conventional ones such as temperature and plastic strain. The feasibility of a high-pressure metallurgy based upon these observations needs to be investigated.

9.5 Reference

- [1] R.K. Ray, J.J. Jonas, R.E. Hook, *Int. Mater. Rev.* 39, (1994) 129.
- [2] T. Obara, S. Satoh, M. Nishida, T. Irie, *Scand. J. Metall.* 13 (1984) 201.
- [3] T. Obara, K. Sakata, in: *Proceedings of the 39th Mechanical Working and Steel Processing Conference*, Indianapolis, IN, 1997, pp. 307–314.
- [4] S. Morito, X. Huang, T. Furuhashi, T. Maki, N. Hansen, in: *Proceedings of the 25th Risø International Symposium on Materials Science*, Roskilde, Denmark, 2004, pp. 453–458.
- [5] N. Hansen, X. Huang, *Mater. Sci. Forum* 475–479 (2005), 37.
- [6] F.P. Bundy, H.T. Hall, H.M. Strong, R.H. Wentorf, *Nature* 176 (1955) 51.
- [7] H.P. Bovenkerk, F.P. Bundy, H.T. Hall, H.M. Strong, R.H. Wentorf, *Nature* 184 (1959) 1094.
- [8] H.T. Hall, *Rev. Sci. Instrum.* 31 (1960) 125.
- [9] E. Ito, in: G. Schubert (Ed.), *Treatise of Geophysics*, Elsevier, Amsterdam, 2007, pp. 197–230.
- [10] W.C. Leslie, *The Physical Metallurgy of Steels*, McGraw-Hill, New York, 1981.
- [11] P.M. Kelly, J. Nutting, *JISI* 197 (1961) 199.
- [12] G.R. Speich, P.R. Swann, *JISI* 203 (1965) 480.
- [13] E.A. Wilson, *ISIJ Int.* 34 (1994) 615.
- [14] J.-M. Lee, K. Shibata, K. Asakura, Y. Masumoto, *ISIJ, Int.* 42 (2002) 1135.
- [15] I.A. Rauf, J.D. Boyd, *Metall. Mater. Trans.* 28A (1997), 1437.
- [16] M.J. Bibby, J.G. Parr, *JISI* 202 (1964) 100.

- [17] F.P. Bundy, *J. Appl. Phys.* 36 (1965) 616.
- [18] H. Hasegawa, *Phys. Rev. Lett.* 50 (1983) 130.
- [19] J.E. Hilliard, *Trans. AIME* 227 (1963) 429.
- [20] T.G. Nilan, in: *Proceedings of the Symposium on Transformation and Hardenability in Steels*, Climax Molybdenum Company of Michigan and the University of Michigan, 1967, pp. 57–66.
- [21] T.G. Nilan, *Trans. Metall. Soc. AIME* 239 (1967) 898.
- [22] T. Kakeshita, T. Saburi, K. Shimizu, *Mater. Sci. Eng., A*, 273–275 (1999) 21.
- [23] Jun-Yun Kang, Seul Cham Kim, Jeang-Ook Oh, Heung Nam Han, Kyu Hwan Oh and Hu-Chul Lee, *Volume 66, Issue 1, January 2012, Pages 45–48*

국문 초록

본 논문에서는 리튬 이온 배터리 활물질의 사이클 진행에 따른 미세구조를 공기 노출을 배제한 상태로 집속이온빔과 투과전자현미경을 이용한 분석을 통하여 활물질의 충방전 거동에 의해 발생하는 미세조직 변화를 이해하였으며 미세조직과 전기화학적 특성의 상관 관계를 규명함으로써 장수명 특성 구현을 위한 안정적인 미세구조를 도출하였다.

본 논문은 2 개의 파트로 구성되어있다. 첫번째 파트에서는 실리콘 음극 재료의 미세 조직 변화관찰을 통해 수명 열화 원인을 분석하였으며 장수명 구현을 위한 실리콘 합금의 미세조직과 카본 코팅과 같은 추가공정의 효과를 확인하였다.

실리콘은 3600mAh/g 라는 graphite 의 10 배에 해당하는 큰 용량을 가지고 있으나 Lithiation 시 수반되는 부피 팽창(300%)에 의해 입자의 전기적 단락과 액체 셀의 경우 사용시 전해액과 맞닿은 영역에서 부반응 층이 형성되어 전해액의 고갈이 발생하여 수명 특성이 급감하는 단점을 가지고 있어 이를 보완하기 위한 연구가 활발히 진행되고 있다.

본 논문의 2 장에서는 응력 관점에서 실리콘 부피 팽창시 발생하는 응력의 최소화와 수명 열화 원인을 분석하였다. 장수명 구현을 위해서는 다음의 미세구조에 다음의 조건이 필요하다. 첫째 실리콘 입자의 미세화를 통하여 팽창시 발생하는 응력을 최소화 하여야 하며 둘째 입자 전체에 균일한 미세조직을 형성하여 응력 불균형을 방지 해야 한다. 세번째로는 압점을 통해 치밀한 입자를 구현하여 입자 내 전해액의 침투를 통한 급격한 부반응 영역의

형성을 억제하는 것이 필요하다. 본 연구에서는 안정적인 미세 구조 형성을 위해 Mechanical Alloying process 을 이용하였다. Si-Fe 합금을 High energy ball milling 을 통하여 분쇄하여 입자의 미세화와 균일한 조직을 형성하였으며 Graphite 카본을 bonding phase 로 적용하여 압점을 개선하여 수명 특성을 개선하였다.

3 장에서는 효과적인 부반응층 형식 억제를 위하여 실리콘 표면 특성 개선을 위한 관점에서의 연구를 진행하였다. 첫째로 실리콘 나노 입자 표면에 5~10nm 의 카본층을 형성하여 기계적인 파단의 방지와 부반응층 형성을 억제하였다. 사이클 진행 후에도 코팅층이 원상태를 유지하고 있는 것을 확인하였다. 둘째로 ionic liquid 를 전해액으로 사용하여 수명특성이 개선되는 것을 확인하였다. Ionic liquid 에 포함되어있는 유기물이 실리콘 입자 표면에 카본 층을 형성하여 안정적인 부반응 층으로서 역할을 하여 수명특성이 개선되는 것을 확인하였다.

4 장에서는 카본 매트릭스에 실리콘 입자가 박혀있는 구조가 사이클 진행 시 실리콘이 카본 매트릭스로 확산되어 3 차원 실리콘 네트워크를 형성하는 것을 확인하였다. 실리콘 네트워크는 스프링과 같은 형태로 응력에 대한 구조적 안정성과 이온전도도를 증가시켜 주는 역할을 할 것으로 기대된다.

두 번째 파트에서는 양극 물질에 대한 미세 구조 연구를 진행하였다. 특히 고체전해질과 액체 전해질 모두를 분석하여 각각의 특징을 확인하였다.

5 장에서는 FeS₂ 가 고체전해질에서 안정적으로 작동하는 원인을 규명하였다. 액체셀의 경우 FeS₂ 는 중간상인 Fe, S 가 분리되어 FeS₂ 로 돌아가지 못 하여

수명 특성이 저하되나 고체 셀의 경우 중간상의 분리가 억제되어 사이클 진행이 가능함을 확인하였다. 또한 사이클 진행 중 cubic structure 가 더 큰 unitcell 을 가지는 orthorhombic 으로 변하여 리튬의 이동이 더 쉬워지는 것을 확인하였다.

6 장에서는 표면 코팅을 통해 Ni-Mn-Co 양극 재료의 특성 개선에 대한 연구를 진행하였다. NMC 는 충방전에 의해 결정성이 떨어져 intercalation 이 방해받게 되어 수명 특성이 저하된다. 입자 표면에 Atomic Layer Deposition 을 이용한 Al₂O₃ 층을 형성하여 입자의 결정성을 유지함으로써 수명특성 뿐만 아니라 율특성이 개선 되는 것을 확인하였다.

본 연구는 리튬이온전지 다양한 재료의 미세구조 분석을 통해 전지 재료의 특성과 미세조직의 상관관계를 도출하였다.

표제어 : 리튬이온 배터리, 실리콘 음극, 카본 코팅, 극판 부피 팽창, 3D Si network, 활물질 미세구조, 고체 전해질, 투과전자현미경, 집속이온 빔